Optimization of ^{83m}Kr tracer diagnostics and design of the slow control for the purification system for XENON1T

Sergej Schneider

Master thesis

Institut für Kernphysik
Mathematisch-Naturwissenschaftliche Fakultät
Westfälische Wilhelms-Universität Münster

17. August 2015

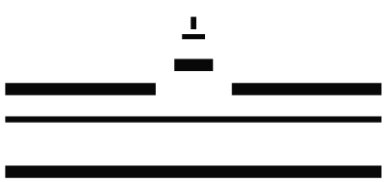

Westfälische
Wilhelms-Universität
Münster

Referent: Prof. Dr. C. Weinheimer

Korreferent: Prof. Dr. A. Khoukaz

Eigenständigkeitserklärung

Hiermit versichere ich, dass ich diese Arbeit selbstständig und nur unter Verwendung der angegebenen Quellen und Hilfsmittel verfasst habe. Alle Textstellen, die wortwörtlich oder sinngemäß anderen Werken entnommen sind, wurden unter genauer Angabe der jeweiligen Quelle als Entlehnung gekennzeichnet.

_____

Münster, 17. August 2015

Contents

Chapter 1

Introduction

For decades the question of the composition of the universe has been one of the most fascinating in cosmology. Although the first evidence for a so called "dark matter", a non-baryonic and extremely weakly interacting form of matter, has been found not less than 82 years ago by Fritz Zwicky, up to this day it has eluded itself from any direct experimental detection. Various theoretically well motivated candidates have been introduced which could potentially explain the vast amount of mass, that is missing in order to explain our universe as we observe it. One very promising candidate that could make up for this absence of mass is the so called WIMP (weakly interacting massive particle).

The WIMP is hence the object of a world wide scientific search of which one of the leading experiments is the XENON Dark Matter Project. It tries to detect the nuclear recoil of a WIMP in a dual-phase xenon time projection chamber. The international collaboration has set itself the goal to increase the sensitivity for a WIMP search by two orders of magnitude with the new XENON1T detector in relation to its results in 2012 with the XENON100 detector. While the latter could at that time set the most stringent upper limit for a possible spin-independant cross section but not find any direct evidence, the expectations for this finding are high with the upcoming XENON1T. For this two crucial subsystems have been developed by the XENON group from the University of Münster. When entering a sensitivity regime as high as aimed with XENON1T, background in the detector cannot be sufficiently reduced solely by shielding because internal radioactivity becomes a significant problem. Therefore a cryogenic distillation column has been developed in order to reduce the long living ^{85}Kr ($t_{1/2} = 10.74\,\mathrm{a}$[Sin14]) level beforehand. Furthermore, electronegative impurities have to be continuously removed from the detector material in order to allow electron drift times long enough for the electrons to penetrate the whole detector. In order to address this a gas system was constructed that includes a purification unit and acts as a central distributing system for the experiment.

For the characterization of the distillation column a scintillation detector has been developed using a $^{83\mathrm{m}}$Kr tracer method. The optimization of this detector will be presented in this thesis. Futhermore the development of a slow control system for the purification system which is going to be implemented in the slow control environment of XENON1T will be described.

Chapter 2

Dark Matter

Huge scientific effort was made within the last decades to perform significant experiments that would create a full and consistent picture of the universe. The outcome of this is the clarity that an overwhelming majority of the energy density of the universe is yet completely unknown to modern science. According to the recent Planck results[Pla13] merely 4.9% can be explained with baryonic matter whereas 26.8% are supposed to result from the so called dark matter and 68.3% from dark energy, which is responsible for the acceleration of the expansion of our universe. While dark energy is a concept hard to grasp, especially regarding a direct experimental detection, the existence and the possibility of experimentally detecting dark matter is well motivated by various physical theories.
In this chapter the search for dark matter will be motivated through the presentation of some of the most compelling evidence. Furthermore, some of the more favoured candidates for dark matter will be introduced as well as their potential methods of discovery.

2.1 Evidence

2.1.1 The galaxy rotation problem

The effects of dark matter were first experimentally observed in the 1930s when Fritz Zwicky analysed the kinematic properties of the Coma cluster and concluded that in order to fulfil the virial theorem, the cluster has to contain 400 times more mass than observed by optic spectroscopy[Zwi33]. The following decades the significance of this observation was overlooked by the scientific community until Vera Rubin and Kent Ford presented an extensive survey about the dynamics of spiral galaxies in the 1970s. By analysing the Doppler shift of the 21cm hydrogen line they could conclude the rotational velocity of stars in spiral galaxies with different distances to the galactic center[Rub70].
With a given mass distribution $M(r)$ one would expect a velocity $v(r)$ given by Newtonian mechanics as

$$v(r) = \sqrt{GM(r)/r}. \tag{2.1.1}$$

Since the majority of the luminous mass is accumulated in the central bulge of a galaxy and

decreases for large distances, a decreasing velocity is expected. Contrary to the expectation, measurements showed a flat behaviour of the rotation curves for large radii. By adding a halo of non visible matter, the measured velocity distribution could be accurately modelled (see figure 2.1).

Regarding the possibility of direct experimental detection, the galaxy rotation problem is especially significant since it implies the presence of dark matter on Earth due to its position in our galaxy.

While at that time the scientific discussion was rather focussing on missing mass, i.e. the question of what undetected objects made out of ordinary baryonic matter could make up for this discrepency, where particularly MACHOs (massive compact halo objects) were thought could solve the galaxy rotation problem, more and more scientific evidence was found pointing towards the necessitiy of non-baryonic matter.

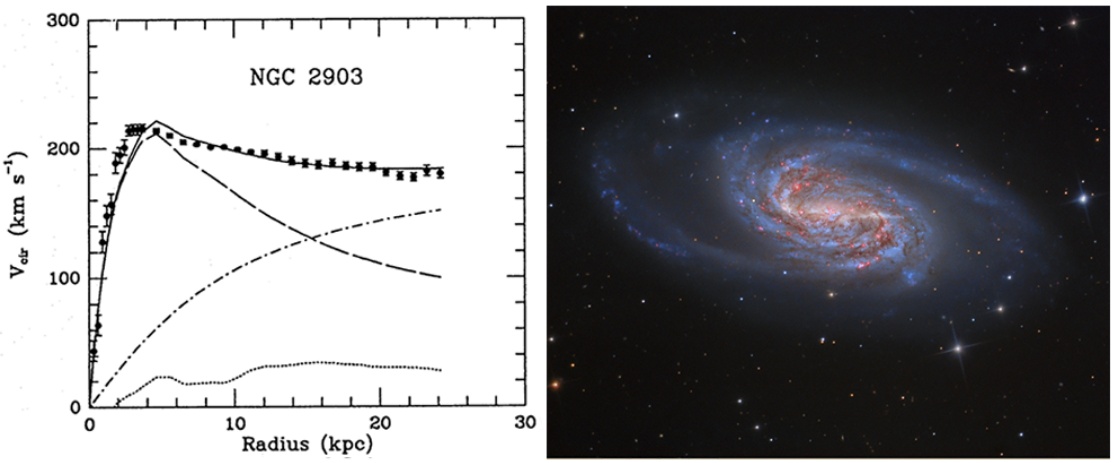

Figure 2.1: *Left:* Rotational velocity in dependance of the radius of the spiral galaxy NGC2903 fitted with a three parameter dark-halo fit (solid line). The single components of the fit are shown: luminous matter (dashed line), interstellar gas (dotted line) and dark halo (dash-dotted).[Beg91]; *Right:* Colored image of the galaxy NGC2903[NASA10].

2.1.2 Colliding galaxy clusters

The event of colliding galaxy clusters provides maybe one of the most impressive proof for dark matter and a particular strong one against the modified Newtonian dynamics (MOND)[Clo06], a theory hypothesizing changes to the force law at very low accelerations[Mil87]. In case of such a collision galaxies in most cases pass each other unaffected due to the great distances by which they are seperated. However, the dominant component of luminous mass, namely the intergalactic plasma which is detectable by X-ray spectroscopy, interacts with each other and decelerates, leading to an accumulation of mass in the center of collision.

Large collection of matter leads to the effect of gravitational lensing, as predicted by the theory of general relativity, where the light between a source and the observer is bent in a characteristic way. In the case of high local mass density, e.g. black holes, light is bent in characteristic rings

or is seen multiple times around the distorting object. Contrary to this so called strong lensing effect, the weak lensing effect observed in the more complex mass distributions of galaxy clusters leads to only a small distortion, perceivable as stretching of background sources of only a few percent. In order to reconstruct the mass distribution in such a system, a large number of sources has to be analysed for their preferred stretching, taking systematic sources of error into account. This allows to map the actual mass distribution of such colliding systems. The most prominent cluster system is the Bullet cluster seen in figure 2.2. In the X-ray image where the gravitational potential is overlayed, derived from weak gravitational lensing, one can clearly see that the plasma and the actual center of mass decoupled. This also reveals that dark matter has to be weakly interactive to both baryonic matter as well as to itself.

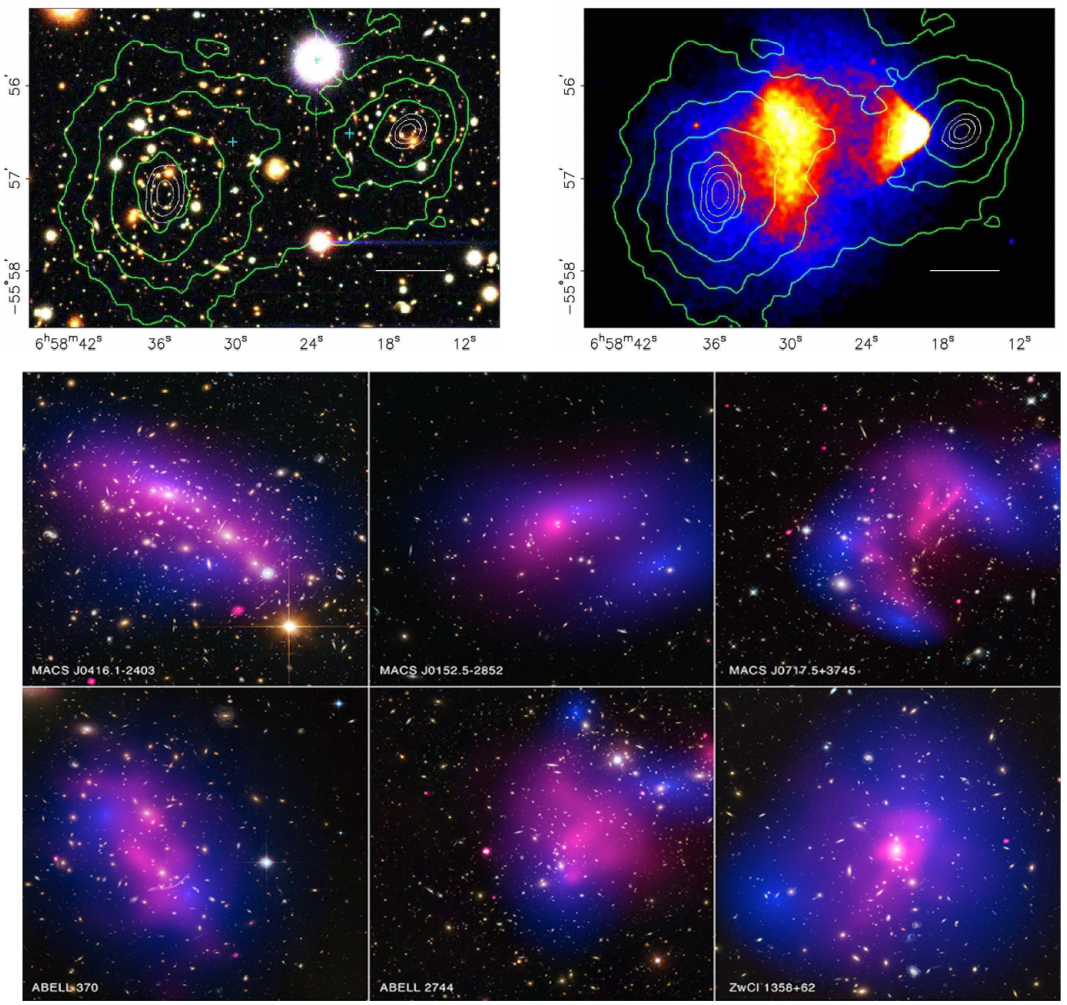

Figure 2.2: *Top:* Colored optical image (*left*) and X-ray image (*right*) of the "Bullet Cluster" 1E0657-558. The green contours show the weak lensing reconstruction. The center of mass is surrounded by the white contours, indicating the peak of the weak lensing effect. The biggest density of X-ray emitting gas is represented by the yellow/white area.[Clo06]; *Mid/Bottom:* Exemplary selection of colliding galaxy clusters with overlayed dark matter map through gravitational lensing analysis (blue) and luminous mass distribution through X-ray analysis (pink) [Har15].

A recent study analysing the dynamics of colliding galaxy clusters in detail (images taken with ESA/NASA's Hubble space telescope and NASA's Chandra X-ray observatory) showed that in all 72 observed systems the three major components, namely baryonic matter in stars, plasma and dark matter could be separated by means of their gravitational effects showing an offset in their mass distribution and hence setting a highest limit on the self-interaction cross section of dark matter to $\sigma_{\mathrm{DM}/m} < 0.47\,\mathrm{cm}^2/\mathrm{g}$ (at 95% CL). With this the existence of dark matter could be stated with a confidence of $7.6\,\sigma$[Har15].

2.1.3 The Cosmic Microwave Background

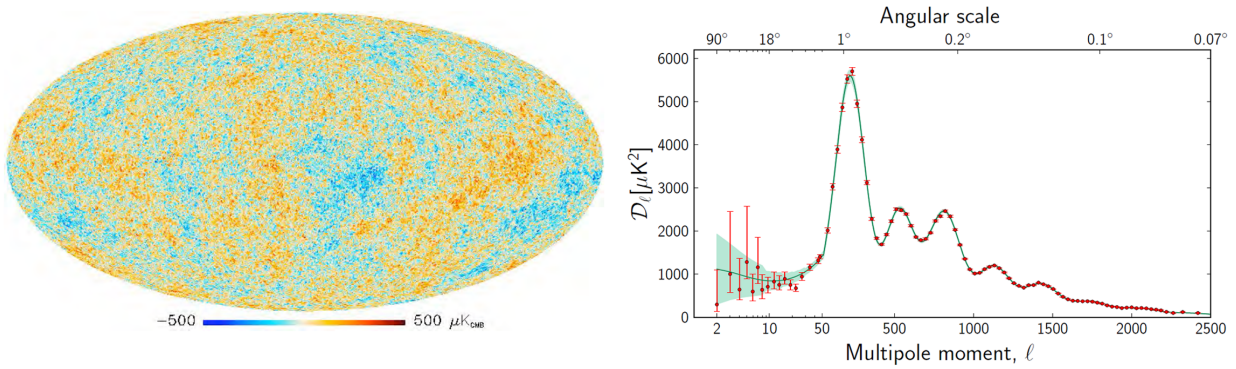

Figure 2.3: *Left:* Plancks map of the Cosmic Microwave Background. The fluctuations in temperature lie in between $\pm 500\,\mu\mathrm{K}$; *Right:* The 7-year angular power spectrum from Planck. The solid red line is the best fit given by the 6-paramter ΛCDM model [Pla13].

A quantitative statement about the amount of dark matter on an even larger scale gives the cosmic microwave background (CMB). The CMB is a radiation background originating from the recombination phase of the early universe approximately 380000 years after the big bang, where matter was nearly isotropically distributed as plasma. At this point the universe cooled down just to the temperature of about 3000 K where the plasma recombined to atoms and hence became transparent to photons. The radiation thereby released can be measured today as a uniform background at a low temperature of 2.725 K (see figure 2.3 left) due to the redshift of the photons caused by the expansion of the universe. Although the CMB, which is the best black body radiation ever measured, shows only faint anisotropies of about 10^{-5}, their physical implication are all the greater.

When analysing the angular momentum of the power spectrum, the CMB reveals important information about the composition of the universe. Due to the interplay of gravitationally induced mass accumulation and the radiation pressure of photons in plasma, baryonic matter is expected to have been oscillating in the primordial universe. Photons decoupling from a bigger gravitational potential will have less energy than those from a small potential due to the Sachs-Wolfe effect[Toj06]. Considering further effects like the Silk damping which describes the outwashing of small scale anisotropies due to dissipation of overdensed regions through diffusion,

a structure formation leading to the galaxies we see today would not be possible without a non-baryonic form of matter. Therefore one can actually deduce the amount of dark matter that has to exist in our universe by detailed analyses of the angular power spectrum (as seen in figure 2.3 right). The fit that matches the measured data extremely well is a six-parameter Lambda cold dark matter (ΛCDM) modell. It shows that in our apparently very flat universe 31.7 % is made out of matter, of which only 4.9 % is baryonic. The remaining 68.3 % is explained by the mysterious dark energy[Pla13].
Based on the Big Bang theory, physicists predicted a microwave background in the area of only a few Kelvin before its detection and could perfectly explain the observed fluctuations, making the measurement of the CMB one of the landmark tests supporting the model of an expanding universe.

2.2 Candidates for Dark Matter

Combining all found evidence we are faced with an overwhelming amount of reason to believe that dark matter exists with a particle like nature. This evidence also necessitate certain properties for a potential dark matter candidate that would all lead to the effects explained in chapter 2.1. First of all it has to be long living on the scale of the age of the universe, since we observe its effects to this day. Furthermore it has to be electrically neutral since no electromagnetic interaction is observed. It has to be non-baryonic as the results from the CMB reveal and interact only on a weak scale. Finally, due to its gravitational effects it has to be massive. While at first glance standard model neutrinos do fulfil all these requirements, due to the smallness of their mass and their highly relativistic velocity in the early universe they cannot explain the effects associated with dark matter.
Theory naturally provides several potential candidates from physics beyond the standard model that could make up for this matter dominating component. In the following chapter some of the most promising candidates will be introduced.

2.2.1 Weakly Interacting Massive Particles (WIMPs)

One of the candidates studied intensely is the WIMP[Ber10]. WIMPs are a class of particles which were not specifically thought up to solve the dark matter problem but arise naturally from extensions of the standard model (SM) of particle physics, e.g. the theory of Supersymmetry (SUSY). Although the SM is one of the most successful theories in physics which predicted the existence of numerous particles that could be later discovered and describes many aspects of nature very accurately, undeniably strong evidence was found that imply physics beyond the standard model (e.g. ν-oscillation, ΛCDM, matter-antimatter asymmetry etc...). SUSY is a theory developed in the 1970s that associates every known fermion/boson from the SM with a supersymmetric bosonic/fermionic partner which differs in spin by 1/2 (see table 2.1).
It is one of the most popular theories for physics beyond the standard model due to the elegance with which it can solve several major problems in physics which are incomprehensible in the

Table 2.1: Standard Model particles and their superpartners in the MSSM.[Eds97]

Standard Model particles and fields		Supersymmetric partners			
		Interaction eigenstates		Mass eigenstates	
Symbol	Name	Symbol	Name	Symbol	Name
$q = d, c, b, u, s, t$	quark	$\tilde{q}_L$, $\tilde{q}_R$	squark	$\tilde{q}_1$, $\tilde{q}_2$	squark
$l = e$, μ, τ	lepton	$\tilde{l}_L$, $\tilde{l}_R$	slepton	$\tilde{l}_1$, $\tilde{l}_2$	slepton
$\nu = \nu_e$, ν_μ, ν_τ	neutrino	$\tilde{\nu}$	sneutrinno	$\tilde{\nu}$	sneutrino
g	gluon	$\tilde{g}$	gluino	$\tilde{g}$	gluino
$W^\pm$	W-boson	$\tilde{W}^\pm$	wino	$\tilde{\chi}^\pm_{1,2}$	chargino
H^-	Higgs boson	$\tilde{H}_1^-$	higgsino		
H^+	Higgs boson	$\tilde{H}_2^+$	higgsino		
B	B-field	$\tilde{B}$	bino	$\tilde{\chi}^0_{1,2,3,4}$	neutralino
W^3	W^3-field	$\tilde{W}^3$	wino		
H_1^0	Higgs boson	$\tilde{H}_1^0$	higgsino		
W_2^0	Higgs boson	$\tilde{H}_2^0$	higgsino		
W_3^0	Higgs boson				

SM. Particularly the hierarchy problem motivated the development of SUSY. Similarly to the fine-tuning in the strong CP problem, the large discrepancy between weak force and gravitational force of 10^{32} towards weak interaction seems unnatural since it requires major quantum corrections of the Higgs mass. In SUSY these corrections are not necessary and the divergence is naturally explained due to a spontaneously breaking symmetry in the TeV scale. Moreover it provides a framework for the unification of particle physics and gravity at the Planck energy scale ($\approx 10^{19}$GeV). The first conclusive and experimentally most investigated theory of supersymmetry in particle physics is the Minimal Supersymmetric Standard Model (MSSM). It considers only the minimal number of supersymmetric particles. The model naturally provides suitable dark matter candidates since under assumption of R-parity conservation all SUSY particles would eventually decay into the stable Lightest Supersymmetric Particle (LSP)[Ber05]. R-parity is a multiplicative quantum number consisting of baryon number B, lepton number L and spin s

$$R = (-1)^{3B+L+2s}. \tag{2.2.1}$$

While for SM particles R-parity is $R = 1$, supersymmetric particles have $R = -1$. Hence SUSY particles can only decay into an odd number of further SUSY particles. In the MSSM the LSP is the lightest neutralino $\tilde{\chi}^0_1$, which is in fact a linear combination $\tilde{\chi}^0_{1,2,3,4}$ of the bino $\tilde{B}$ and the neutral wino $\tilde{W}^3$, two superpartners of gauge bosons, as well as two higgsinos $\tilde{H}^0_1/\tilde{H}^0_2$. The neutralino is a neutral Majorana particle and only interacts on the weak scale with SM particles. Due to the brokenness of SUSY these particles are believed to be heavy around $\mathcal{O}(100\,\text{GeV})$ which is why they are classified as weakly interacting massive particles.
These WIMPs would have been in a thermal equilibrium in the early universe, i.e. an equal rate

of annihilation to and creation out of SM particles

$$\chi + \chi \leftrightarrow \mathrm{SM} + \mathrm{SM}. \tag{2.2.2}$$

When the universe cooled down to a temperature lower than the WIMP mass $T < m_\chi$ the rate of SM particles annihilating to WIMPs decreased, thereby disturbing the thermal equilibrium. Since it is Boltzmann suppressed, the WIMP abundance n_χ dropped exponentially until it fell below the Hubble expansion rate $H = \dot{R}/R$, describing the expansion rate of the universe. At this "freeze-out" point the WIMP abundance stayed constant and can be calculated based on the Boltzmann determining abundance

$$\frac{dn_\chi}{dt} + 3Hn_\chi = -\langle\sigma_A v\rangle\,(n_\chi^2 - n_{\chi,eq}^2) \tag{2.2.3}$$

to be

$$\Omega_\chi h^2 \approx \frac{3 \cdot 10^{-27}\mathrm{cm}^3\mathrm{s}^{-1}}{\langle\sigma_A v\rangle}, \tag{2.2.4}$$

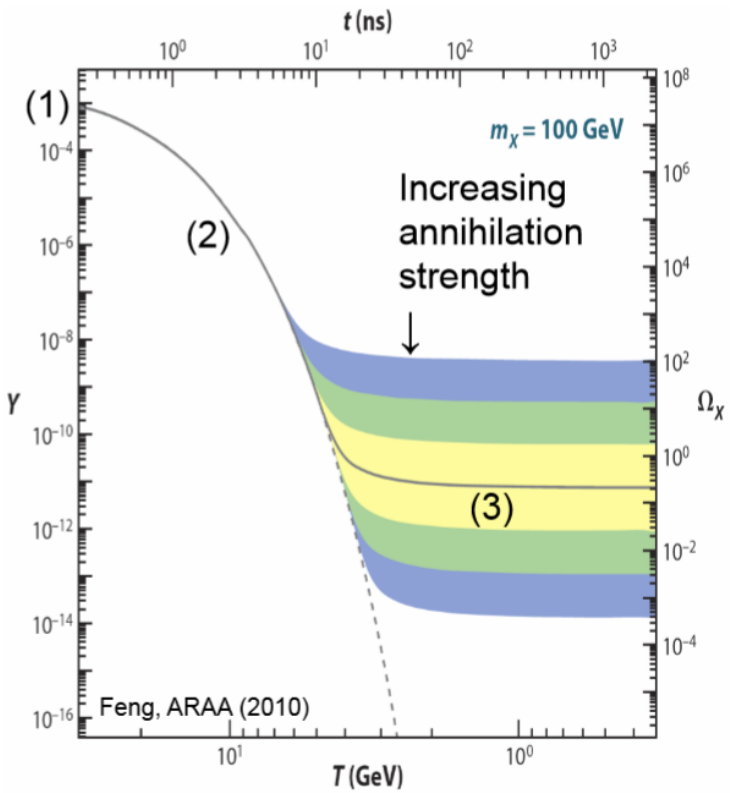

Figure 2.4: Evolution of number density of WIMP during "freeze-out" for a 100 GeV WIMP in the early universe. The solid curve shows the abundance starting from a thermal equilibrium (1) while the universe is cooling (2). When the expansion rate of the universe exceeds the annihilation rate of χ the relic abundance stays constant (3). The solid grey line shows the expected abundance from CMB multipole analysis[Fen10] and the coloured regions are for cross sections that lead to a difference of 10 (yellow), 10^2 (green) and 10^3 (blue) from this value.

where $\langle \sigma_A v \rangle$ is the velocity averaged WIMP annihilation cross section[Jun96]. Inserting a weak scale cross section of $\langle \sigma_A v \rangle = 10^{-26} \mathrm{cm}^3 \mathrm{s}^{-1}$ leads to the abundance we concluded from the CMB analysis of $\Omega_{\mathrm{DM}} \approx 0.27$ (see figure 2.4). This pleasant coincidence, called the "WIMP miracle", encourages the WIMP hypothesis furtheron.

Despite its great potential to solve several problems of the SM, the MSSM got strongly constraint in recent years. With energies in the TeV scale, high energy particle colliders should potentially be able to detect MSSM particles. Particularly the absence of supersymmetric particles in the 2012 run of LHC has cast doubt on the MSSM and led to a more intense focus on extended models of the MSSM. While in some of these models the LSP differs from the neutralino, in most cases they provide particles that can be categorized as WIMPs and therefore are suitable dark matter candidates.

2.2.2 Sterile Neutrinos

Although neutrinos with their three known flavours (electron-, muon- and tau neutrino) do constitute an amount of dark matter they can only account for a small fraction of it. Due to the fact that neutrinos are governed by oscillation between their flavour states, it is definite that they must have a mass[Oli14a]. However, all measurements so far could only set a highest limit on the neutrino mass, indicating it to be extremely small ($< \mathrm{eV}$). Furthermore, they are catogerized as "hot" dark matter, i.e. particles which were relativistic during structure formation and thereby having a free-streaming length much larger than the average size of a proto-galaxy. Hence they cannot explain the small scale anisotropies observed in the CMB that would leed to formation of galaxies.[Ber05]

The hypothetical sterile neutrino, which comes as an extension of the standard model of particle physics, could however make up for the missing amount of mass. It comes as one of the extensive consequences of massive neutrinos. In the SM, neutrinos only exist with a left-handed chirality, antineutrinos only with a right-handed chirality respectively. In this scenario neutrinos would not aquire mass from their Yukawa coupling to the Higgs field, as it is the case for all other fermions. By introducing a right-handed neutrino, the sterile neutrino, the process of mass aquirement through the Yukawa coupling would naturally apply to neutrinos and thereby explaining their oscillation in the first place. Additionally it would explain why the masses of neutrinos are so vanishingly small through the seesaw-mechanism. As a right handed neutrino, it would not participate in the weak interaction and hence from the four known fundamental forces only interact gravitationally. Sterile neutrinos are catogerized as "warm" dark matter with masses in the keV regime[Kus09], that could explain small scale anisotropies in the size of typical protogalaxies. Since sterile neutrinos would only interact directly by gravitational force a direct experimental detection is extremely challenging.

2.2.3 Axions

Axions were originally proposed as a possible solution to the strong charge parity problem. The CP symmetry is a combination of charge- and parity symmetry. It states that a particle behaves physically identical to its mirror particle with inversed charge. Based on the decay of neutral kaons, the violation of the CP symmetry for the weak interaction was found in 1964. Similarly, a CP violation is expected for the strong interaction because the QCD Lagrangian contains the theta term[Oli14b]

$$L_{CPV} = \bar{\theta}\frac{g^2}{32\pi^2}G^{a\mu\nu}\tilde{G}_{a\mu\nu} \tag{2.2.5}$$

with the gluon field strength $G_{a\mu\nu}$ and $G^{a\mu\nu}$ being its dual and g being the coupling of the strong interaction. This term breaks the CP symmetry for the case of a non-zero $\bar{\theta}$. This is however contradictory to experimental findings. This leads to the two possibilities of either facing a fine-tunig of $\bar{\theta}$ to a tremendously exact level of 10^{-10}[Oli14b] or the effects of new physics. By adding the spontaneously broken Peccei-Quinn symmetry to the SM, the CP violating term cancels out, leading to the non-observation of the CP violation in the strong interaction. Moreover, this would in particularly explain the vanishingly small electric-dipole moment of the neutron. Since in the quantum field theory a field is always associated with a particle, the Peccei-Quinn symmetry would lead to the existence of a new particle, the axion. While the orignially proposed "standard" and "variant" axions, whose interaction scale was believed to be similar to the weak scale, were already excluded by experiment, models describing "invisible" axions like the KSVZ (Kim-Shifman-Vainshtein-Zakharov) or DFSZ (Dine-Fischler-Srednicki-Zhtnisky) model still provide viable scenarios for the existence of axions or axion-like particles (ALPs).
Naturally these particles also fulfil all the necessary properties in order to act as a potential dark matter candidate. Axions are massive, neutral particles which only couple very weakly to the strong and weak interaction. Their mass is predicted to be at $\lesssim 10\,\mathrm{meV}$. Coming in the right abundance, axions could make up for a significant part of the observed dark matter energy density.

2.3 Methods for the detection of Dark Matter

With the number of different theories adressed, which provide numerous potential dark matter candidates, there come also several ways of potentially detecting those particles. The search for WIMPs can be divided into three different strategies.

1. Detection in collider experiments

   If SM particles are provided with high enough energy in particle colliders they should in principle be able to annihilate into WIMPs, like it was the case in the very young universe. In collider experiments neither WIMPs nor their possible decay products are actually observed. Rather their signature could be find in missing energy when the chain of events are reconstructed. The currently highest energy collisions were provided by the

LHC with 8 TeV center of mass energy. In the analysis of its proton-proton collision no signature of dark matter was found[Mar13]. In near future the LHC will be upgraded to achieve its goal of 14 TeV and thereby opening a new energy window for dark matter search in collider experiments. The weak point of collider experiments regarding dark matter search is certainly that they could not provide the evidence needed to state if the found particle has the required stability in cosmological timescales. Since colliders look for traces of energy missing from particles escaping the detector, they could only deduce a stability within this timescale of $\mathcal{O}(\mu s)$.

2. Indirect detection

   Since WIMPs are expected to annihilate with the self-annihilation cross section σ_A or maybe even decay with a half-life at least as long as the age of the universe, regions with a higher density of dark matter should show an excess of their annihilation or decay products like photons, antimatter or neutrinos at energies similar to the WIMP mass of $10^2 - 10^3$GeV[Ber10]. Such regions would be galactic halos, dwarf galaxies or the center of the sun. If WIMPs annihilate directly to photons without a primarily decay into secondary particles, the produced photons will be mono-energetic. In this scenario a clear line in the γ-ray spectrum should be visible at energies equal to the mass of the WIMP, similar to the 511 keV peak from electron-positron-annihilation. The most recent results for an indirect dark matter search were published by the AMS collaboration. With the alpha magnetic spectrometer orbiting the earth, they were able to show a clear increase of positron fraction up to energies of ~ 350 GeV[Agu13] indicating the existence of dark matter particles in this region of energy.

3. Direct detection

   The strongest statement about the existence and the nature of dark matter would be made with a direct detection. In this approach physicists look for the recoil energy E_R deposited by a WIMP χ when scattering off of target nuclei N from the detection material. The differential event rate (in units of counts/kg/day/keV) is generally given by

$$\frac{dR}{dE_R} = \frac{\rho_0}{m_N m_\chi} \int_{v_{min}}^{v_{esc}} v f(v) \frac{d\sigma_{\chi N}}{dE_R}(v, E_R) dv. \tag{2.3.1}$$

   It depends on the local WIMP density which is expected to be $\rho_0 \simeq 0.3\,\mathrm{GeV/cm^3}$[Bov12], its velocity distribution $f(v)$ which is often (not completely accurately[Kuh10]) estimated as Maxwell-Boltzmann distribution with an average velocity of $\bar{v} \approx 270$ km/s and the maximum limit being the local galactic escape velocity v_{esc}[Fox11] and the differential cross section for WIMP-nucleus elastic scattering $\frac{d\sigma_{\chi N}}{dE_R}$. It thereby depends on the input from astrophysics and particle physics and with that is associated with their uncertainties. The local dark matter density, for example, is calculated from analysing the dynamics of the Milky Way and shows significant variations depending on the used model[Rea14].

Moreover the differential cross section can be separated into the spin-independent cross section σ_{SI} and the spin-dependent cross section σ_{SD}. In the case of spin-independent cross section the WIMP couples to the content of the nucleus with the atomic mass number A

$$\left(\frac{d\sigma_{\chi N}}{dE_R}\right)_{SI} = \frac{2m_N A^2}{\pi v^2} F^2(E_R) \tag{2.3.2}$$

where F is the form factor, which is the Fourier transformation of the mass distribution of the nucleus. If the WIMP has a non-zero spin value it can couple by axial vector coupling to the spin content of the detector nuclei with the differential cross section of

$$\left(\frac{d\sigma_{\chi N}}{dE_R}\right)_{SD} = \frac{16m_N}{\pi v^2}\Lambda^2 G_F^2 J(J+1)\frac{S(E_R)}{S(0)} \tag{2.3.3}$$

for a fermionic WIMP (e.g. the neutralino χ_1^0)[Cer10] with the nucleus total angular momentum J, the fermi coupling constant G_F, the spin expectation value S and the constant

$$\Lambda = \frac{1}{J}\left[a_p \langle S_p \rangle + a_n \langle S_n \rangle\right] \tag{2.3.4}$$

including the effective coupling of WIMPs to protons a_p and neutrons a_n. For a bosonic WIMP of spin $s = 1$ (e.g. Kaluza-Klein particle) the interaction term differs slighty from equation 2.3.3. For a zero-value spin the spin-dependent cross section obviously disappears.

A scattering event in xenon causes a signal which can be differentiated into three excitation channels, namely scintillation-, ionization- and heat signal where most experiments make use of two channels to increase their background reduction by a sophisticated signal analysis (see fig. 2.5). In order to be able to directly detect these very rare events that only cause small signals, experiments generally have to be designed as low background experiments.

Two less commonly used signals that can be taken advantage of are tracking signals induced through ionization from WIMP scattering in low pressured gas (e.g. DRIFT) and the creation of bubbles by heat deposition in super heated liquids (e.g. PICASSO).

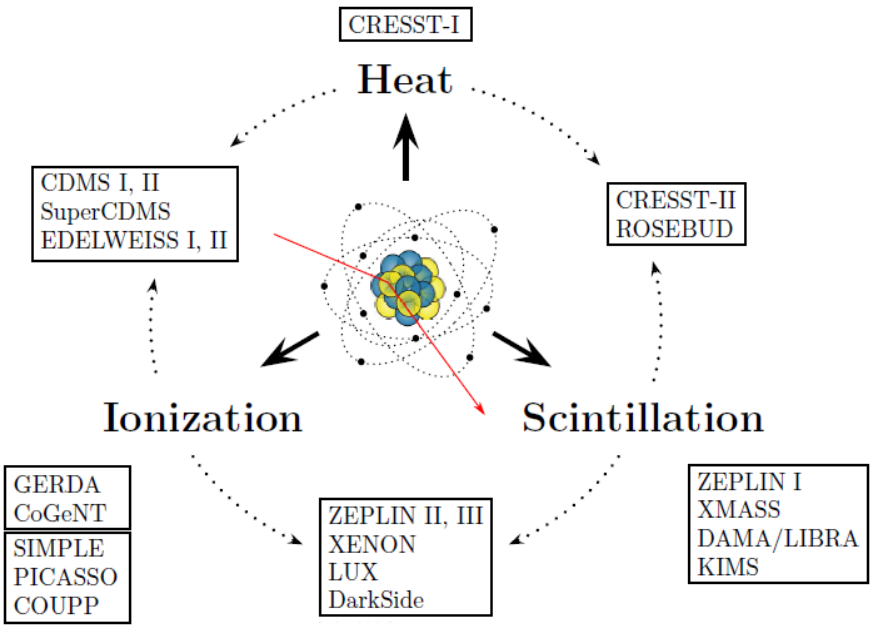

Figure 2.5: Scheme of the three excitation channels used for the detection of WIMP scattering with experiments listed accordingly to their experimental method[Pla12].

Chapter 3

The XENON Dark Matter Project

The XENON Dark Matter Project is a direct detection experiment located at the underground laboratory *Laboratori Nazionali del Gran Sasso* (LNGS) in Italy. Experiments in the underground laboratory are shielded by 1400 m of rock (equivalent to 3800 mwe (meter water equivalent)[Bel12]) from the surrounding mountain Gran Sasso d'Italia. This provides an efficient background reduction from cosmic ray induced muons by six orders of magnitudes[Apr10]. XENON tries to directly detect dark matter in the form of scattering WIMPs by measuring their recoil energy in form of light and charge in a dual phase xenon time projection chamber (TPC). The detector design allows not only to reconstruct a scattering event in three dimensions but also enables a discrimination of electron and nuclear recoil through the analysis of the ratio of light to charge deposited by a scattering event. The project was designed to gradually enlarge the detector in three main steps. With XENON10, which started taking data in 2007, the first phase experiment was working with a relatively small detector utilizing only 15 kg of xenon to mainly prove the suitability of the detector design. Within small amount of time the detector principle was applied to a ton scale experiment at XENON1T, which is currently under commissioning. Meanwhile the project could set at that time unmatched exclusion limits on a possible WIMP-nucleus cross section with both their detectors XENON10 and XENON100. While these could only exclude possible WIMP regions, big hopes lay on XENON1T to actually find direct evidence of a WIMP since due to its high projected sensitivity it will enter a promising parameter space of potential dark matter candidates and it further on allows for an upgrade to the even more sensitive XENONnT.

3.1 Dual Phase Time Projection Chamber

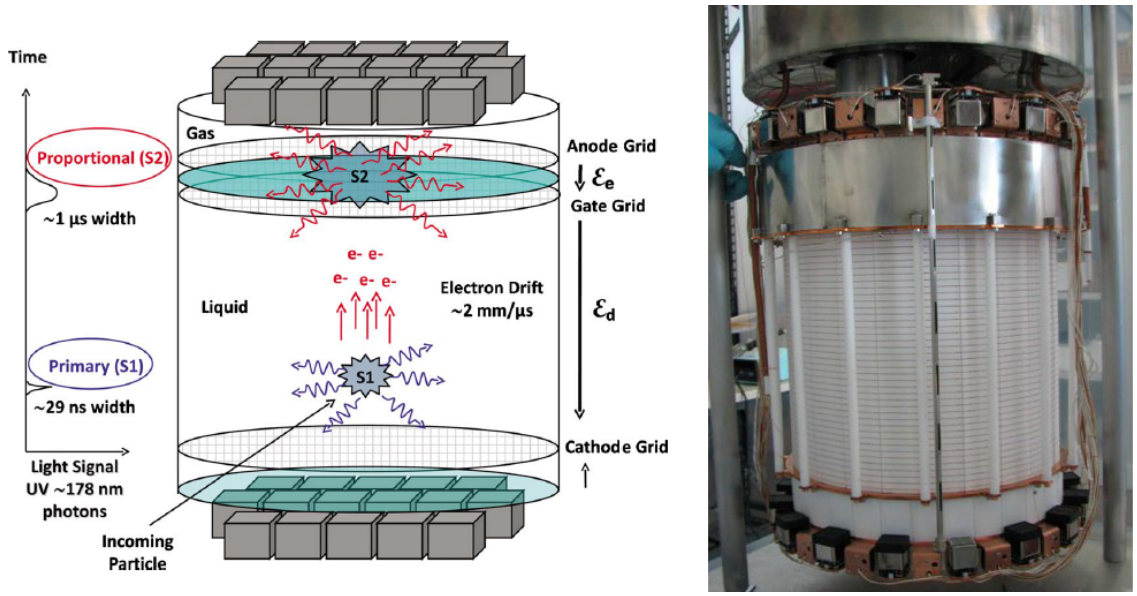

Figure 3.1: *Left:* Measurement principle of a dual phase time projection chamber[Apr10]; *Right:* Photo of the XENON100 inner detector structure [Pla12].

In order to directly detect dark matter, the XENON Dark Matter Project utilizes a dual phase time projection chamber (TPC) filled with liquid and gaseous xenon. The detector volume is monitored by an array of photomultiplier tubes (PMTs) which is placed on top and bottom of the detector and converts the energy of photons to electric charge, which is then digitized and read out by data acquisition system for further analysis. In order to increase the light yield, the inner walls of the TPC are made out of polytetrafluorethylen (PTFE) which shows a high reflectivity for the scintillation light of xenon[Lev14].

The functional principle of the TPC is shown in figure 3.1. A particle scattering in the liquid phase causes both a prompt scintillation signal and free electrons. The scintillation signal (S1) is mainly collected at the bottom array of PMTs since due to the high refractive index of liquid xenon ($n_{Xe} = 1.69$[Sol04]) a large fraction of photons suffer total reflection at the liquid surface. The ionized electrons get accelerated towards the gas phase by a high voltage electric drift field ϵ_d (e.g. 530 V/cm in XENON100[Apr10]) applied between the cathode and gate grid. Since expected WIMP recoils would only transfer energy in the order of ∼10 keV the raw amount of charge is too small to be directly read out. This is why in the gas phase the electric field ϵ_e is further on increased (12 kV/cm in XENON100) to induce the electroluminescence effect where the accelerated electrons extracted from the liquid phase, cause a further scintillation signal (S2). Since the number induced in S2 is directly proportional to the number of ionized electrons, the ratio of S1 to S2 gives information about the interaction process with the target atom and allows to discriminate two fundamentally different processes. While e.g. penetrating β particles or photons interact mainly with the shell of the xenon atoms and therefore cause electronic recoil

with a high ionization fraction, WIMPs are expected to interact with the nucleus. In the latter case the S2/S1 ratio will be much smaller which allows for an increased reduction of background through sophisticated signal analysis.
The time difference between the two signals gives information about the time the electrons drifted from the point of interaction towards the gas phase. With knowledge about the drift speed (1.73 mm/µs for 0.53 V/cm[Apr14a]) the depth coordinate of the point of interaction can be reconstructed. The x and y coordinate can be reconstructed by the signal distribution among the top PMT array. In the case of XENON100 the x-y spacial resolution is ~ 3 mm while the z-resolution is ~ 0.3 mm[Apr12a]. The three dimensional reconstruction furtheron enhances the background reduction because it allows to define an inner fiducial volume.

3.2 Xenon as scintillating detection material

Many of the current direct dark matter detection experiments use xenon as their target material. This is due to the fact that xenon has several properties that make it an excellent detection material. It naturally provides the use of two excitation channels, since it responds to penetrating radiation with both scintillation and ionization. Furthermore among other liquid noble gases it has the highest ionization and scintillation yield for WIMPs with an expected mass of ~ 100 GeV[Apr10]. The scintillation of xenon can be caused by two different processes involving ionized (Xe^+) or excited (Xe^*) xenon that ultimately lead to the formation of an excited molecular state (Xe_2^*), also referred to as excimer[Dok02]. In case of ionization an excimer is created in the absence of an electric field by the following subsequent process:

$$\begin{aligned} Xe^+ + Xe &\rightarrow Xe_2^+ \\ Xe_2^+ + e^- &\rightarrow Xe^{**} + Xe \\ Xe^{**} &\rightarrow Xe^* + \text{heat} \\ Xe^* + 2Xe &\rightarrow Xe_2^* + Xe. \end{aligned} \tag{3.2.1}$$

In case of direct excitation, the excited xenon Xe^* simply forms an excimer with neighbouring xenon atoms in a three body process

$$Xe^* + 2Xe \rightarrow Xe_2^* + Xe. \tag{3.2.2}$$

In gaseous xenon scintillation almost exclusively originates from the latter process because recombination is less likely. In both cases the excimer finally decays by emitting a scintillation photon $h\nu$

$$Xe_2^* \rightarrow 2Xe + h\nu \tag{3.2.3}$$

with a wavelength of $\lambda_{Xe_2^*} = 178$ nm in the case of liquid xenon[Apr10]. Due to the formation of excimers, xenon is transparent to its own scintillation light which allows for a design of detectors with large volumes. Xenon is the heaviest noble gas which has no natural radioactive isotopes

(^{136}Xe with $T_{1/2} = 2.165 \times 10^{21}$ yr[Alb14] being effectively stable on the relevant timescale) which is crucial for a low background experiment. The high mass number $A \sim 131$ is especially useful for the determination of the spin-independent cross section since it scales quadratically $\sigma_{SI} \propto A^2$. Additionally xenon allows to probe the spin-dependent cross section due to its natural isotopic abundance. Two isotopes of xenon occur in the atmosphere, from which xenon is obtained by liquefaction of air, which have a non-zero spin value and make roughly 50% of its isotopic abundance (see table 3.1).
The high atomic number $Z = 54$ and density $\rho \approx 3\,\mathrm{g/cm^3}$ of LXe furthermore lead to an extraordinary good self-shielding from external radiation. Thus upscaling a LXe detector not only means an increase in detection volume but also a decrease in externally induced background.

Table 3.1: Relative isotopic abundance of natural xenon found as trace gas in the atmosphere, normalized to the most abundant ^{132}Xe. Values adapted from [Lae03].

Isotope	Atomic mass [u]	Natural abundance (atom %)	Nuclear Spin (J)
^{124}Xe	123.9058942 (22)	0.09(1)	0
^{126}Xe	125.904281 (8)	0.09(1)	0
^{128}Xe	127.9035312 (17)	1.92(3)	0
^{129}Xe	128.9047801 (21)	26.44(24)	1/2
^{130}Xe	129.9035094 (17)	4.08(2)	0
^{131}Xe	130.905072 (5)	21.18(3)	3/2
^{132}Xe	131.904144 (5)	26.89(6)	0
^{134}Xe	133.905395 (8)	10.44(10)	0
^{136}Xe	135.907214 (8)	8.87(16)	0

3.3 Development of the XENON detectors from XENON10 to XENONnT

The XENON Dark Matter project published its first dark matter results with the relatively small XENON10 detector which had an active mass of about 15 kg in a cylindrical volume of 20 cm diameter and 15 cm height. The active volume was monitored by in total 80 1-inch PMTs (*Hamamatsu*® R8520-AL) which were specially developed for a high quantum efficiency in the relevant wavelength regime (QE $\sim 20\%$ for $\lambda = 178\,\mathrm{nm}$). Additionally to the natural 3800 mwe shielding of the Gran Sasso d'Italia, the XENON10 detector was embedded in a cubic steel-framed shield of 20 cm polyethylene inside a 20 cm Pb shield. As a detector prototype it could demonstrate the efficiency of a liquid xenon dual phase time projection chamber and create a deep understanding of the detector principle to pave the way for further upgrades towards larger detectors. After 58.6 live days of data taken until February 2007 it could not detect any WIMP signals, setting an upper limit on the spin-independent cross section for a $100\,\mathrm{GeV/c^2}$ WIMP to $8.8{\times}10^{-44}\,\mathrm{cm^2}$[Ang08], thereby setting the at that time worlds most stringent limit.
One of the many reasons for the development of a liquid xenon dual phase TPC is its potential

for scalability. Hence after the success of XENON10 the following phase developed quickly, where with the XENON100 detector 63 kg of xenon was utilized in an active cylindrical volume with a diameter of 30 cm and 30 cm in height, monitored by in total 178 PMTs (with a higher quantum efficiency of QE $> 30\%$ for the bottom 80) and additional 64 used for an active veto of 99 kg. Special care was taken for radio-purity of the used materials in order to decrease internal background. In combination with the stronger self-shielding from a larger volume, stronger passive shielding through a 5 cm copper and a 20 cm water shield and active reduction from internal background like ^{85}Kr, the background for XENON100 was reduced by two orders of magnitude in respect to XENON10. This lead after 224.6 live days of measurement until March 2012 to a limit on the spin-independent cross section of $2 \times 10^{-45}\,\mathrm{cm}^2$ for a WIMP mass of $55\,\mathrm{Gev/c}^2$, again setting the at that time worlds most stringent limit, which was since then only surpassed by the LUX collaboration in 2013 with a sensitivity of $7.6 \times 10^{-46}\,\mathrm{cm}^2$ for a WIMP mass of $33\,\mathrm{Gev/c}^2$[Ake14]. Moreover XENON100 could set the most stringent limit on the spin-dependent WIMP-nucleon cross section σ_{SD} of $3.5 \times 10^{-40}\,\mathrm{cm}^2$ for $45\,\mathrm{GeV/c}^2$ WIMPs as well as on the axion electron coupling g_{Ae} of 7.7×10^{-12}[Apr14b].

Building upon the success of its predecessors, with XENON1T an even bigger detector was developed and is currently under commissioning. 3300 kg of liquid xenon are used in an cylindrical detector volume of 1 m diameter and height embedded in an active xenon veto. Furthermore the detector is placed in a water tank of 9.6 m diameter and 10 m height which acts as active Cherenkov muon veto with 4π coverage and reduces the muon induced neutron events. 248 further developed 3-inch Hamamatsu R11410 PMTs monitor the sensitive volume. They were especially designed for high radio-purity and an even higher quantum efficiency for 178 nm photons of QE $> 35\%$. XENON1T aims to reduce the background by another two orders of magnitude in relation to XENON100 and with that will achieve a sensitivity of $2 \times 10^{-47}\,\mathrm{cm}^2$ at 90% confidence level after 2 years of measurement for a spin-independent cross section at a $50\,\mathrm{GeV/c}^2$ WIMP mass, thereby exploring a promising parameter space of potential dark matter candidates.

A special feature of the XENON1T detector is its capability for the final foreseen upgrade to XENONnT. It will be embedded in the same water tank and cryostat as XENON1T, hence allowing a fast and cost efficient upgrade to a 7 T liquid xenon detector. The cryostat was specifically designed for this upgrade, allowing to install a TPC of 1.4 m in diameter and already containing the cables for the additional PMTs. The significantly bigger sensitive volume and xenon veto will allow a sensitivity of $\sim 10^{-48}\mathrm{cm}^2$ for $50\,\mathrm{GeV/c}^2$ WIMPs (see fig. 3.2 for achieved and projected sensitivities of various dark matter experiments).

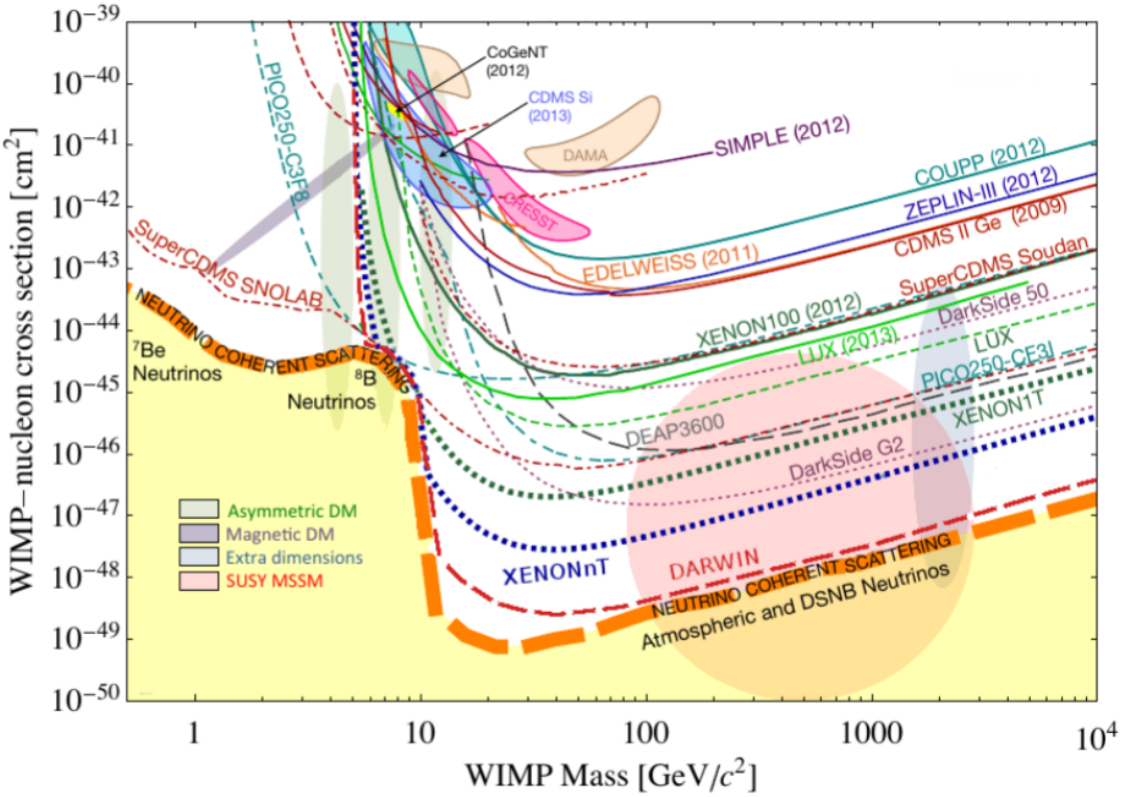

Figure 3.2: Achieved and projected limits on the spin-independent WIMP nucleus cross-section for various direct dark matter experiments along with parameter space as predicted by the Constrained Minimal Supersymmetric Extension of the Standard Model[Apr13b].

3.4 A cryogenic distillation column for the removal of radioactive ^{85}Kr out of xenon

In order to increase its sensitivity to a cross section which is two orders of magnitude smaller than XENON100, the XENON1T detector had not only to provide a bigger sensitive volume but in particular had to deal with its intrinsic background sources. In this regard especially the radioactive krypton isotope ^{85}Kr poses a critical challenge. ^{85}Kr is an atmospherical trace gas in the abundance of $^{85}\mathrm{Kr}/^{\mathrm{nat}}\mathrm{Kr} \sim 10^{-11}$ mol/mol[Che99], mainly produced artificially as a nuclear fission product. Since xenon is obtained by liquefaction of air, commercially available xenon contains a small amount of natural krypton $^{\mathrm{nat}}\mathrm{Kr/Xe} \sim 10^{-6} - 10^{-8}$ mol/mol even after special purification. ^{85}Kr decays by beta-decay into ^{85}Rb with an endpoint energy of 687.4 keV and a half-life of $t_{1/2} = 10.74$ a[Sin14]. Due to the relatively long half-life and its intrinsic occurrence, even with an excellent discrimination rate for electronic and nuclear recoils of 99.5%, ^{85}Kr can mimic a WIMP scattering signal and thus has to be actively removed for low background experiments like XENON100 or XENON1T. In the case of XENON100 the removal of ^{85}Kr out of xenon was performed by a cryogenic distillation column from Taiyo Nippon Sanso® [Abe09]. With this distillation column, xenon could be purified to a level of 10^{-11} with a throughput of

Figure 3.3: Picture of the 5 m distillation column developed for XENON1T in the university of Münster.

0.6 kg/h. However, in order to reach the projected sensitivity of XENON1T, ^{nat}Kr has to be removed down to a level of 10^{-13}. Moreover, to achieve this in a feasible amount of time the throughput has to be much higher. In order to reach this design goal the XENON group in the University of Münster has constructed a 5 m cryogenic distillation column to achieve a xenon purity of $^{nat}\mathrm{Kr/Xe} < 0.2$ ppt (parts per trillion) with a throughput of 3 kg/h and a collection efficiency of 99% (see fig. 3.3). It takes advantage of the different vapour pressure of krypton and xenon, where krypton being the high volatile component can be separated from the liquid phase and accumulated in an off-gas at the top of the column. Performance measurements with a smaller 3 m test facility produced a xenon with a non-measurable level of krypton. Even with extremely sensitive gas-chromatography measurements, performed by the MPIK in Heidelberg, the krypton concentration could only be estimated with an upper limit of < 26 ppq (parts per quadrillion) and with that surpassing the goal for XENON1T by more than one order of magnitude (detailed information can be found in the PhD thesis by Stephan Rosendahl[Ros15]).

3.5 A gas circulation and purification system for XENON1T

As described in section 3.1 the way the XENON detector utilizes charge from scattering events is by drifting ionized electrons towards the gas phase to cause a second ionization signal. The detection ability thereby depends on the ability to drift charge over the total height of the detector, i.e. 1 m for XENON1T. At a given drift speed this only depends on the electron life time τ_e, which describes the characteristic time free electrons can move in a medium before being captured, following an exponential behaviour[Apr06]

$$N(t) = N_0 e^{-t/\tau_e}, \tag{3.5.1}$$

where N_0 is the number of free electrons at t_0. Electronegative impurities (e.g. H_2O, O_2, N_2) in the target material can attenuate electrons and thus reduce τ_e as well as impair the light yield from a direct scintillation signal[Dob10]. The electron life time τ_e is inversely proportional to the concentration of impurities n_I and the attachment rate constant k_s

$$\tau_e = \frac{1}{k_s \cdot n_I}, \tag{3.5.2}$$

which is a constant depending on the type of impurity and the applied electric field. Therefore, in order to achieve an electron lifetime and a scintillation light yield sufficient enough for an experiment in the dimension of XENON1T, where τ_e has to be $\mathcal{O}$(ms), electronegative elements have to be continuously removed from the target material to a sub-ppb level O_2 equivalent.
For this a gas system was developed which both serves as a central gas distributing system for the whole experiment and removes electronegative elements in two parallel purification lines with high temperature zirconium getters (see fig. 3.6). The getter from SAES®, rated for a flow rate of 75 slpm, removes electronegative impurities by chemically binding them to a zirconium alloy at a temperature of 400 °C[Sae01]. This process is irreversible so that no danger of releasing

the collected impurities can occur. The manufacturer states a purity performance of $< 1\,\text{ppb}$ for relevant impurities, which was confirmed by several electron life time measurements within the XENON experiment[Apr12a]. Since zirconium oxide has a higher electrical resistance than pure zirconium, the absorption capacity can be inferred by measuring the cartridges resistance. The getter electronic automatically gives notification before a decrease of absorption efficiency occurs and the getter cartridge has to be replaced for optimal performance.

Since outgassing of H_2O molecules from inner materials is not only inevitable but even increased in LXe, because it acts as an effective solvent due to its strong Van-der-Waals interactions, a continuous recirculation of the whole detection material through the zirconium getters is required. The water concentration is moreover continuously monitored by a lossless in-situ analysis with a moisture analyser from *Tiger Optics*. Its measurement principle can be seen in fig. 3.4. A gas sample in a cavity enclosed by two ultra-high reflective mirrors gets irradiated by a continuous wave diode laser with photons in the IR range at around $\lambda = 1392.5\,\text{nm}$ where H_2O molecules show an absorption peak. A photodiode detector measures the small fraction of light that decouples from the cavity. By measuring the decay time $\tau(\nu)$ of the signal intensity after shuttering the light source, the water concentration N can be determined to a level of $(0.4 \pm 0.2)\,\text{ppb}$. Therefore a reference measurement is performed in order to measure the decay time τ_0 at a different wavelength, which does not excite H_2O molecules. From the difference of the reciprocal of these ringdown times one can deduce the water concentration by

$$N = \frac{1}{c \cdot \sigma(\nu)} \left(\frac{1}{\tau(\nu)} - \frac{1}{\tau_0} \right) \tag{3.5.3}$$

where $\sigma(\nu)$ is the absorption cross section and c is the speed of light.

The system is designed to work at high flow rates up to about 100 slpm in order to meet the requirements of XENON1T. Therefore, two parallel purification lines each including a getter and a circulator pump are provided for the required high flow rate as well as for redundancy,

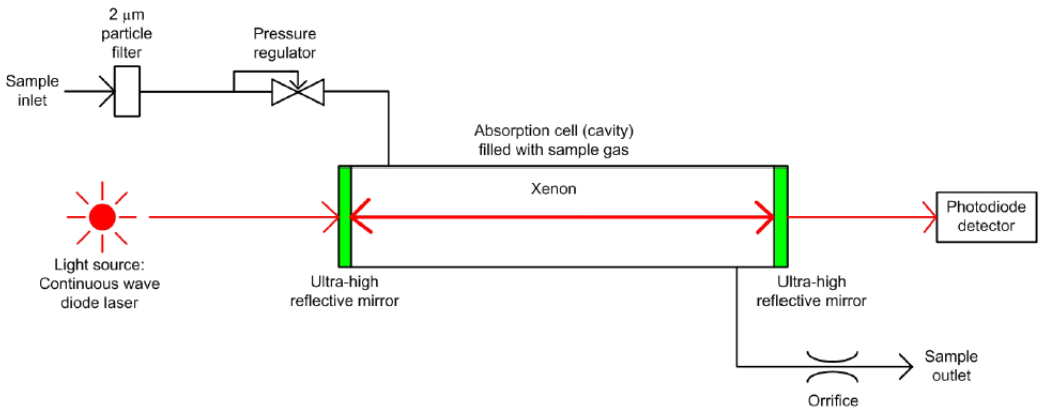

Figure 3.4: Schematic of the principle of a cavity ringdown spectroscopy in the moisture analyser from *Tiger Optics*. Taken from [Ros15], based on the information of the HALO+ instruction manual[Tig06].

ensuring a continuous purification even during a possible failure or maintenance. The circulation pumps from *QDrive*® were chosen due to their characteristic as high flow, oil-free and radon pure pumps. While the pumps have been tested and approved for their stability at relatively high flows ($\gtrsim 50$ slpm) and an oil contamination from a failing pump can be excluded, the radon content is still a topic under investigation.

The gas system is fully remotely controllable by the use of in total 34 bellow-sealed pneumatic valves (*Swagelok*® SS-8BG-VCR-5C/5O). Furthermore, in order to monitor the gas dynamics within the system, five pressure sensors (*Swagelok*® PTU-S-AC9-31AD) and three mass flow controllers (MKS® 1579A) have been installed at crucial positions. The pressure sensors utilize a metal thin-film technology, where a changing system pressure changes the resistance of the strain gauge[Swa07]. The mass flow controller determines the mass flow by utilizing the thermal conductivity of xenon in a laminar bypass element[Hin95]. At the entrance and the exit of this element the gas temperature is measured with a temperature sensitive, resistive element. In between a small amount of heat is induced by a heating element at the wall. Since in a laminar flow the rate of heat transfer Q from the walls is directly proportional to the mass flow rate F_m, it can be precisely determined with knowledge about the specific heat of the used gas c_p and the temperature difference between the gas before and after contact with the heating element $\Delta T = T_2 - T_1$[Lip93]

$$F_m = \frac{Q}{c_p \cdot \Delta T}. \tag{3.5.4}$$

The MKS® 1579A not only allows to monitor but also to control the gas flow up to a flow of 100 slpm through the implementation of a magnetic coil driven control valve. It is internally controlled by a PID algorithm (see chapter 4.2 for a description of a PID algorithm) which compares the current flow to the setpoint and accordingly adjusts the valve until any deviation vanishes[MKS06].

Finally, the gas purification system not only provides connection to other subsystems but also provides two idle ports which can be used to connect additional diagnostics or calibration sources. All the instruments described above have to be included to a slow control system, which will be described in the following.

Figure 3.5: Picture of the purification system of XENON1T as installed at LNGS (courtesy of the XENON collaboration).

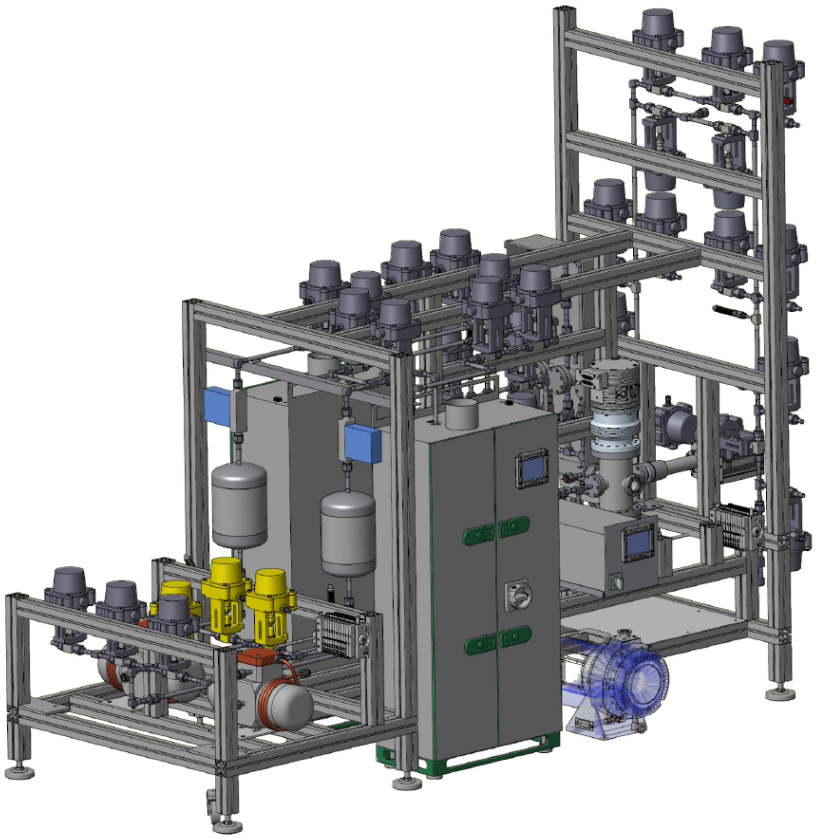

Figure 3.6: Technical drawing of the purification system of XENON1T (provided by Dipl. Ing. Christian Huhmann).

Chapter 4

The slow control environment of XENON1T

The slow control system of XENON1T was designed to provide an independent low level development for each subsystem while ensuring a uniform schematic representation on the supervisory level. This allows shifters from different parts of the experiment to become quickly acquainted with unfamiliar systems without cutting the autonomy of the respective working group. Therefore, each subsystem has a dedicated independent local controller unit, which is implemented in a networked architecture controlled by a central supervisory control and data acquisition (SCADA) system (see fig 4.1). For safety reasons two SCADA servers are simultaneously running at all times, one as an active server, the other as a standby server for redundancy. This standby server is run in a fail-over mode, allowing an automatic switch in case the active server fails.

A commercial slow control system from *General Electric* was chosen as developing framework. This grants both a high level of reliability and the possibility of a professional customer service. The development software package *Proficy Process System* (PPS) is composed of different programs dedicated for their respective area of application. Fundamental programming of the RX3i programmable automatic controller (PAC) is done on the expert level with *Proficy Machine Edition* where control logic can be written with different programming languages. *Machine Edition* supports programming of the RX3i with C coding, as well as coding in ladder diagram (LD), LabView resembling function blocks diagram (FBD) and Pascal resembling structured text (ST), where the combination of C and LD has shown to be very powerful while at the same time convenient. The SCADA system is developed with *Cimplicity* while the historical database is created with *Historian*, allowing storing physical values of any data points. Lastly, local touch screen functionality is provided for each subsystem using operator panels from *Beijer Electronics*, which come with their own developing software *Information Designer*. Although from a different supplier, the used RX3i PAC from GE is implemented in *Information Designer* by default, which allows interfacing the PAC and the operator panel without much effort.

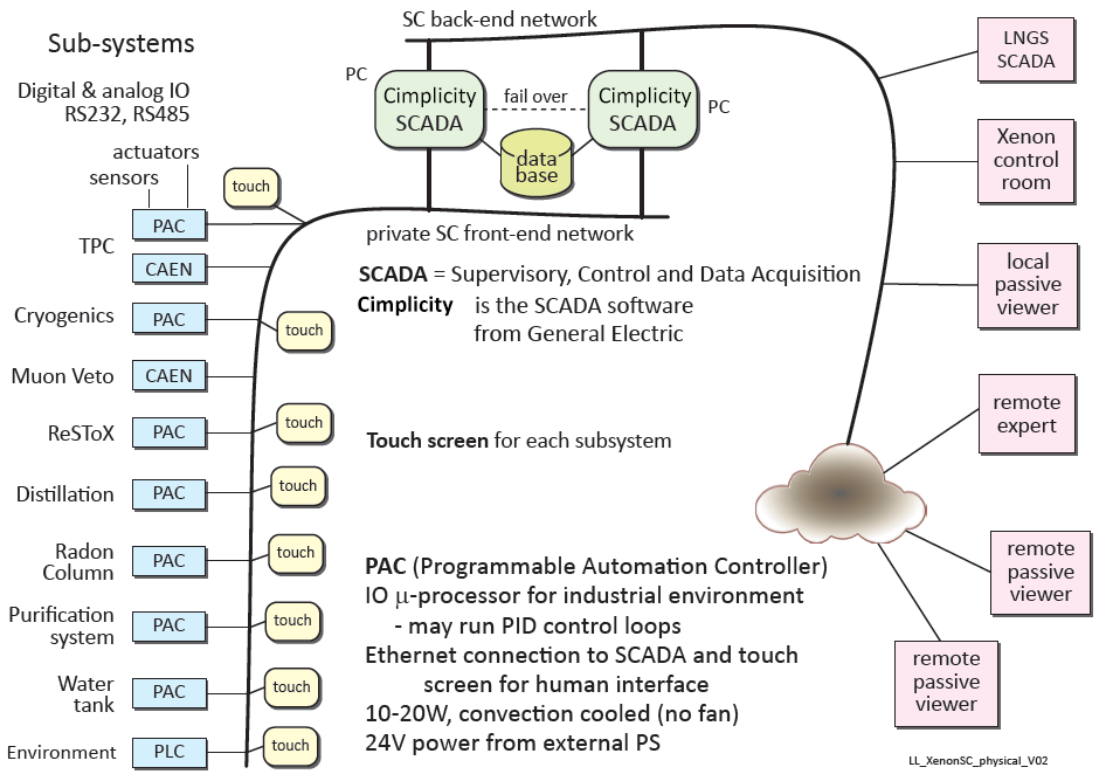

Figure 4.1: Overview of the slow control structure of XENON1T[Car13].

4.1 Design of a slow control system for the purification system of XENON1T

The purification system of XENON1T serves both as gas purification unit as well as central distribution system for the whole experiment (see fig. 4.2). Hence, the gas exchange of every subsystem is dependent on the state of this particular system and the ability for control is especially important. For the commissioning phase of other subsystems like the storage and recovery (ReStox) or cryogenic system, the purification system had to be present. Thus, its delivery to LNGS was asked for at a very early stage of the experiment. At that point the construction and testing of the gas circulator pumps for the purification system have not been finished as well as the infrastructure of XENON1T has not been fully setup yet, i.e. neither the SCADA servers nor the historical database server were installed. Thus the main goal of the design of the slow control system for the purification system for XENON1T within the context of this thesis, was to provide a preliminary system which supports the commissioning phase of the mentioned systems as well as prepare necessary steps for a quick integration to the upcoming network structure as soon as provided. This implies that even without an existing SCADA system users should be able to have full control over the system through the operator panel, preferably without the need of intervening through the expert level. Additionally security automatisms should be included to prevent damage to the system by false usage.

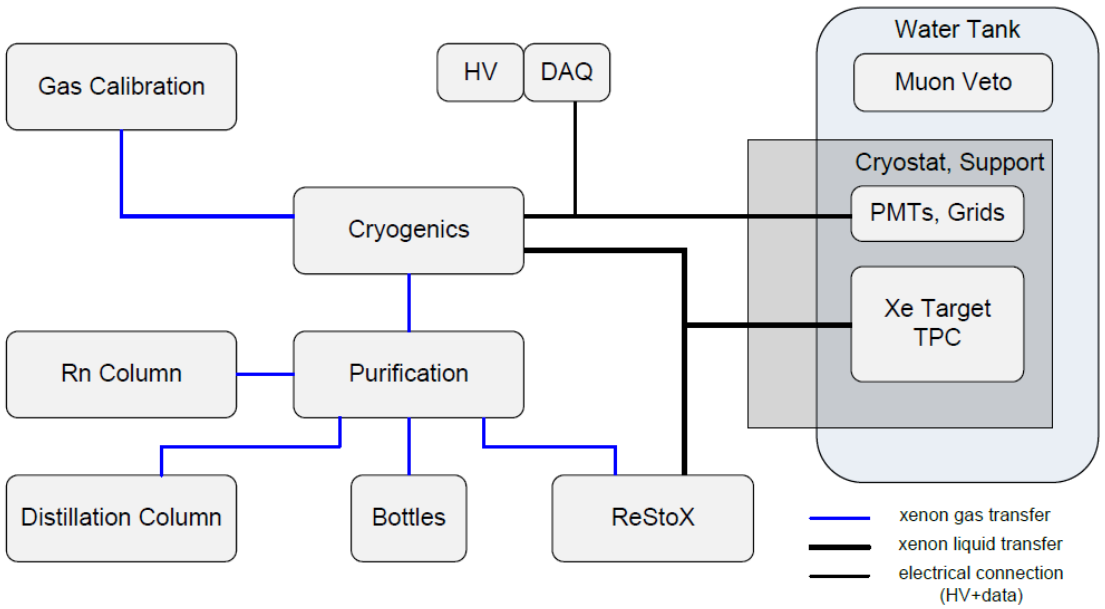

Figure 4.2: Block diagram of the XENON1T subsystems showing their relationship. Taken from[Car13].

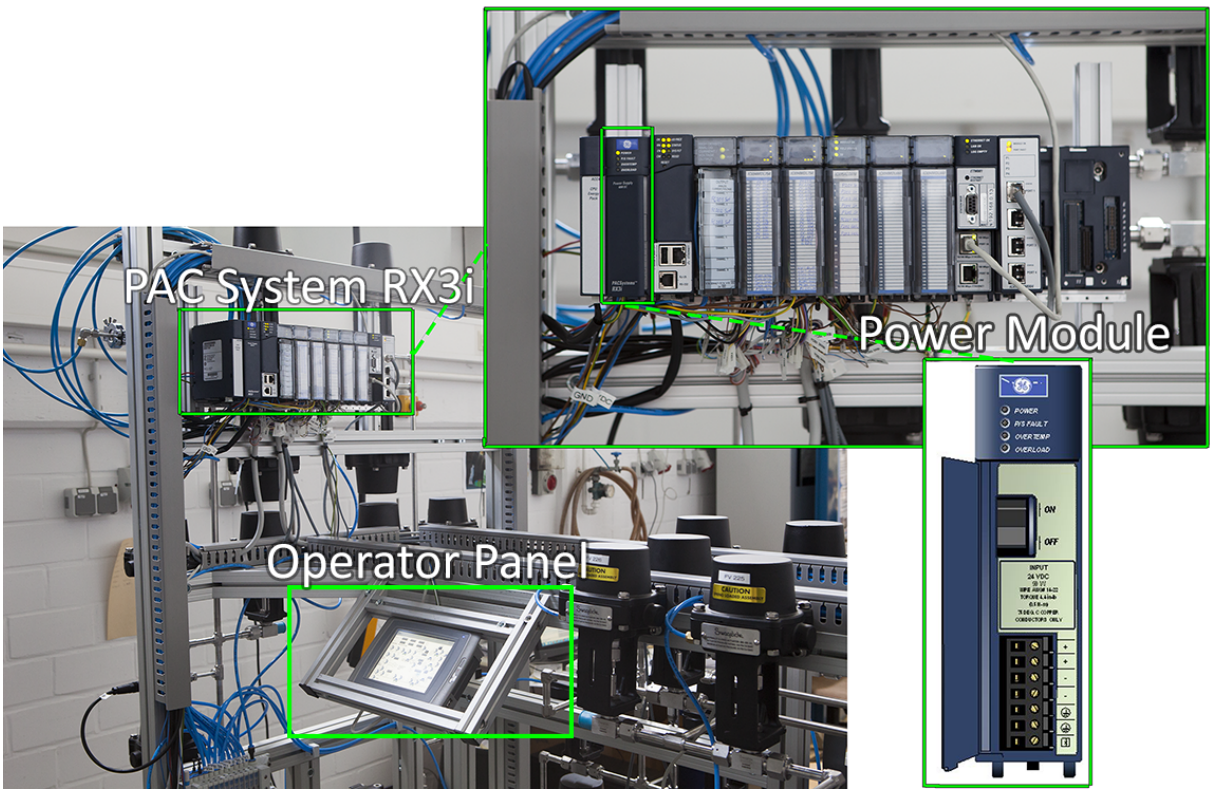

Figure 4.3: *Bottom left:* Picture of the PAC and the operator panel installed at the purification system. *Top right:* Front view of the PAC with its numerous modules for control and monitoring of different communication protocols. *Bottom right:* Detailed view of the power module of the PAC.

For on site control the purification system has a 10" *EXTER T100* operator panel attached directly to the system (see fig. 4.3). When switching on the power module of the PAC, both the operator panel as well as all instruments get powered on. This provides full controllability as a stand-alone system during first commissioning. The operator panel starts up with a main window (as seen in fig. 4.5) from which one can navigate to several sub-windows. The most important one is the "*Purification Gas System*"-window which shows the flow chart of the purification system and allows its operation. Furthermore, one can jump to a historical diagram of each sensor which shows the behaviour of the respective sensor within a variable time frame as well as a collective diagram of the flow controllers and the pressure gauges. Finally, the operator panel provides a historical view on occurred alarms in the alarm window.

In order to provide a high level of control and quick access, crucial for the distributing system of XENON1T, all 34 valves installed in the purification system are pneumatic valves (*Swagelok* SS-8BG-VCR-5C/5O), which shifters can operate both from the control room as well as locally using the operator panel. Each valve is connected to a compressed air supply through a valve terminal (*Festo*® MPA-L). Two MPA-L valve terminals, each providing 24 channels for compressed air, are implemented in the system and connected to the slow control through a 25-pin Sub-D plug. Each pin is connected to a digital output module (IC694MDL754) which provides 24 VDC for the solenoid coils of the MPA-L valve terminals. By simply pressing on the symbol representing the respective pneumatic valve on the touch screen or activating the respective boolean on the SCADA level, voltage is supplied to the solenoid coil of the valve terminal and thereby opening or closing the pneumatic valve.

While the majority of these valves are the preferred normally closed versions, due to availability issues five valves are in a normally opened state. They are installed in the least critical locations of the system, i.e. the bypass valves of the calibration ports, the getters and the HALO+. For additional security all pneumatic valves will be added with indicator switches. In the case

Figure 4.4: Picutre of the normally closed (*left*) and normally opened (*center*) pneumatic valves Swagelok SS-8BG-VCR-5C/5O [Swa08]. *Right:* Valve terminal Festo MPA-L [Fes10].

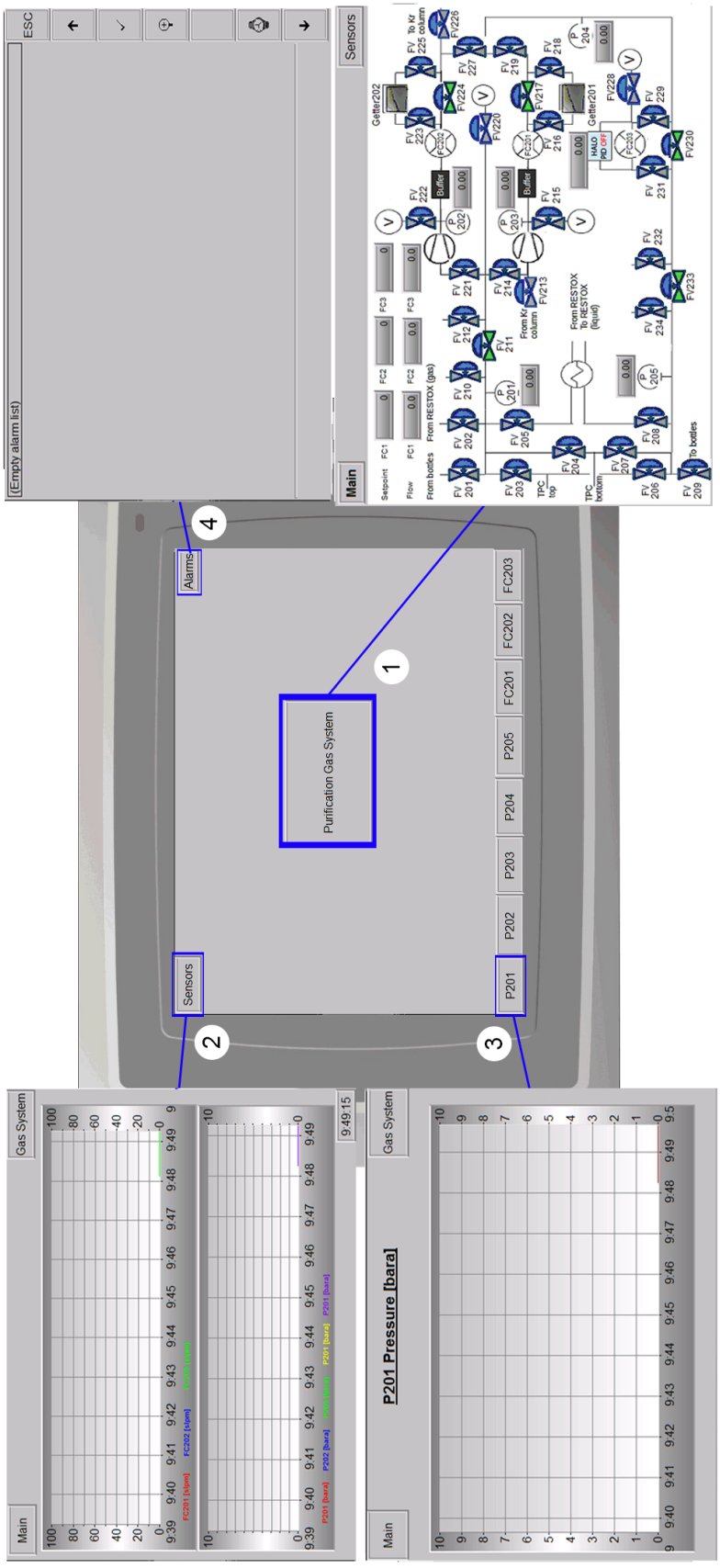

Figure 4.5: Main navigational window of the operator panel with its sub-windows. (1) opens the operation window, (2) combined sensor diagrams, (3) single sensor diagram, (4) alarm window.

of the bellow-sealed SS-8BG-VCR a piston to which a switch can be connected externally is moving while changing the state of the valve. These simple mechanical switches close or open an electrical circuit depending on the position of the valves. Therefore these switches are direct indicators for the status of the valves. In case of non matching set and read out value, an alarm will be send out, pointing out the failed valve.

At the time of shipment, the valves are divided into two security groups. The purification systems internal valves that are not connecting the system to any other systems nor to the vacuum port can be operated without any restrictions. The vacuum valves that are opening the system to the vacuum port are password protected as well as the system valves, which can open the system to other subsystems.

For pressure read out, five pressure transducers from *Swagelok* type PTU-S-AC9-31AD are implemented in the system, located appropriately so a pressure gradient at the two circulator pumps as well as at the HALO+ can be determined. They utilize a metal thin-film technology, where a changing system pressure changes the resistance of the strain gauge[Swa07]. This change is detected and leads to a DC voltage output between 0.1 - 10.1 V with an accuracy of 1% on full scale, which is directly translated to a pressure of 0.0 - 10.0 bar by an analog input module (IC695ALG616).

Furthermore, three mass flow controllers (*MKS* 1579A) are installed in the system which provide full control about the flow rates up to 100 slpm (standard liter per minute). One in each of the two purification lines in order to monitor the effective circulation speed achieved by the recirculation pumps and one bypassing the moisture analyser. The latter has the special feature as it allows, controlled by a PID circuit (proportional-, integral-, derivative, see chapter 4.2), to maintain a pressure difference between the inlet and the outlet of the HALO, which is necessary for a correct operation. The flow controllers can be set to a setpoint by clicking on the grey box next to the "*Setpoint*"-line on the operator panel. Underneath, the actual measured flow of the respective flow controller can be seen.

Regarding the GXe purification, the gas system can be separated into the purification unit, consisting of two purification lines with recirculation pumps and getters, and the monitoring unit which is the moisture analyser from *Tiger Optics*, installed with a bypass option. The zirconium getters (*SAES* PS4-MT50-R) are designed for very little user intervention and low maintenance requirement. For a start up the getter provides a local user interface. Its slow control interface is therefore limited to the supply of pneumatic pressure for its internal valve (controllable through the quadratic getter symbol) and an alarm read out. For the latter, the *SAES* getter provides a customer interface with a relay contact for the detection of alarms and warnings. Simultaneously, it creates a sound in case of alarms and warnings for users on site. The alarm relay is connected by default and disconnects in case of an alarm. 24 VDC is supplied by the digital output module and read out by the digital input module. An alarm is generated both at the SCADA level as well as on the operator panel, where the position of the alarm symbol directly indicates the failed unit. Acknowledging the alarm however, is only possible at the user interface of the respective getter.

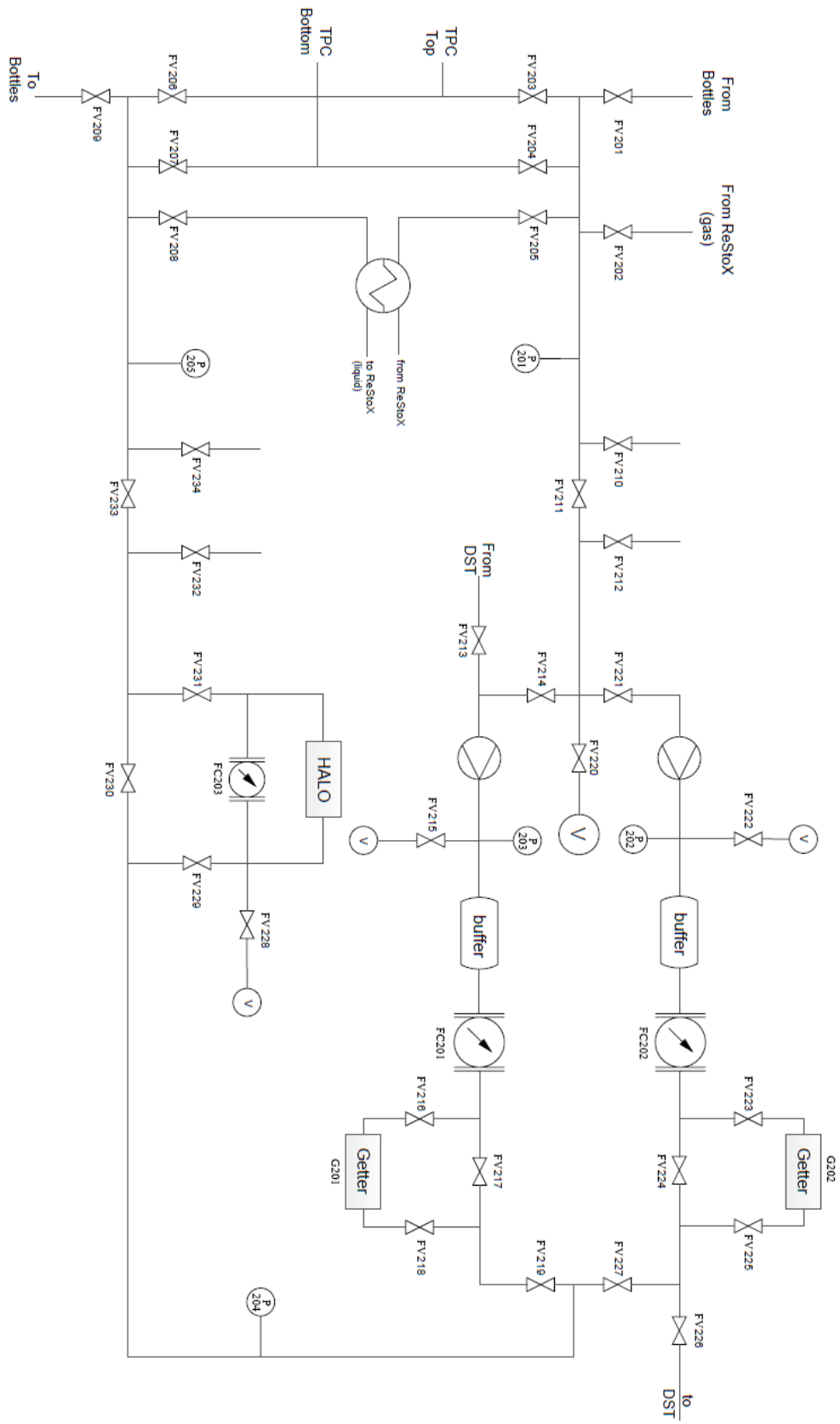

Figure 4.6: P&ID (Piping and Instrumentation Diagram) diagram of the purification system[Car13].

Furthermore the getters provide a remote contact shutdown in the customer interface. In order to open or close this contact a magnetic coil relay was installed exernally which is controlled by the digital output module. This allows to remotely shut down the getters in case of an emergency, e.g. an air leak which could damage the getter. Special care has to be taken, that no large amount of oxygen is introduced into the getter since this could result in a fire if happening at the high operation temperature of 400 °C.
For monitoring the level of electronegative impurities the moisture analyser HALO+ from *Tiger Optics* is utilized. It provides a graphical user interface through a touch screen in the front of the device with full control and read out capability. Furthermore it is embedded in the slow control over a serial RS232 interface connected to the serial port of the CPU module (IC695CPE305). From the SCADA system the user can switch between the three different operation modes (service-, tuning- and measurement mode) by activating the respective boolean. This will send out the on the PAC-level defined command strings to switch to the respective mode. While in measurement mode, the PAC constantly issues a request for the level of impurities measured and outputs the value on the SCADA screen in units of ppb. On the operator panel only the read out is implemented since the user is already on site and can if needed change the mode on the user interface of the HALO+. The impurity value is given on the operating window level of the operator panel and gives the number of the current mode (0 for service, 1 for tuning mode) when not in measurement mode. The symbol representing the HALO+ allows to activate the PID circuit in order to automatically preserve a differential pressure of 700 mbar, which is the condition required for optimal performance as stated by the manufacturer. While the PID control is activated, the manual control over FC203 is blocked.
Since due to the internal working system of the HALO+ a gas back flow into the sample cell cannot be actively prevented and since a higher cell pressure than 2.4 bar could permanently damage the sample cell it is crucial to prevent exposing the outlet of the HALO+ to such a high pressure. Therefore, when the pressure at P205 goes above 2.2 bar the diagnostic section is automatically bypassed and an alarm message appears on the operator panel.

4.2 A PID circuit for the purification system of XENON1T

A correct measurement of the moisture level with a sensitivity of $\approx 0.2\,\text{ppb}$ as quoted by Tiger Optics can only be achieved under correct conditions. In order to maintain the gas flow through the sample cell, the inlet pressure should be ideally higher than 2.6 bar. A lower pressure will still lead to a fairly good measurement result, however it is important that a pressure difference between inlet and outlet is provided to prevent a backflow into the sample cell.
For this, a Proportional-Integral-Derivative (PID) circuit was implemented that controls the flow controller FC203 so that the outlet pressure P205 is always kept 700 mbar lower than the inlet pressure P204, or 1.9 bar maximum if the inlet pressure is above 2.6 bar. The PID control can be turned on by activating the light blue "*HALO*"-box on the operator panel. It will switch from "*PID OFF*" to "*PID ON*" and starts adjusting the flow controller to obtain the differential pressure according to the parameter set in the PAC.
A PID controller is a very commonly used type of feedback control known for its wide range of applicability, its reliability, fast response and its simplicity. A control variable (CV) is thereby manipulated so that a process variable (PV) reaches a certain setpoint (SP). The PID controller does this by determining the deviation ϵ of PV from the desired SP and, depending on this error and the predefined constant P-, I- and D- parameters (K_P, K_I and K_D), sending out a PID output (OP) in the commonly known parallel algorithm

$$OP(t) = \underbrace{K_P \cdot \epsilon(t)}_{\text{P-component}} + \underbrace{K_I \int \epsilon(t) \cdot dt}_{\text{I-component}} + \underbrace{K_D \frac{d\epsilon(t)}{dt}}_{\text{D-component}} . \tag{4.2.1}$$

The three components are defined by their handling of the deviation ϵ. The proportional term simply changes its output proportionally to the current setpoint deviation multiplied with the proportional gain and is typically responsible for the majority of the signal change. The integral term changes the signal output accordingly to the accumulated deviation over time. Its main objection is to eliminate any steady state deviations, intrinsically included in a P-controller. While the integral term often tends to destabilize a control loop, the derivative term anticipates the change of deviations of the setpoint and allows for a stabilization. For the PID loop of the purification system however, the series algorithm was chosen

$$OP(t) = K_P \left(\epsilon(t) + K_I \int \epsilon(t) \cdot dt \right) \left[1 + K_D \frac{d\epsilon(t)}{dt} \right] . \tag{4.2.2}$$

This form of PID algorithm orignates from early analog PID circuits and represents a series circuit with a PI- and PD-controller. It is benefitial for the possible application of tuning methods, where e.g. the most commonly used Ziegler-Nichols PID tuning rules have been developed for and can therefore directly be applied without any conversion.
In the special case of the purification PID loop, SP is the pressure of P205 $SP = p_{P205,set} = p_{P204}(t) - 700\,\text{mbar}$ (for the case $p_{P204} < 2.6\,\text{mbar}$; $SP = p_{P205,set} = 1.9\,\text{bar}$ otherwise) and OP is the voltage provided by the analog output module in order to control the flow mass controller. *GEs Machine Edition* already provides a PID logic block, allowing an easy implementation.

After declaring CV $= F_{FC203}$, PV $= p_{P205}$ and SP $= p_{P205,set}$, only the three PID parameters K_P, K_I and K_D have to be defined.

The optimal value of the respective parameter is system-specific and dependent on the requirement of the control loop. The PID loop is supposed to provide the optimal working conditions for the HALO+ in the continuous working mode of the experiment. Since during the implementation the purification system was a stand-alone system without a connection to any of the other subsystems and the PID loop is system dependent, as soon as the final system state will be achieved, a retuning of the parameter values should be considered to provide an optimal control.

For testing the provided PID circuit a gas bottle filled with argon was connected to the gas system which was finally connected to the outside of the laboratory through a 10 m 1/4" flexible tube. By varying the pressure regulator of the bottle or the flow controller FC202 in one of the purification lines, different flows and pressure conditions could be simulated without actually having the circulation pumps installed. The long flexible tube simulated the large piping system to which the purification system will finally be connected to. The main goal was to provide a PID circuit which reacts stably to both slow and rapid pressure changes without any overshoot in CV, to prevent any overpressure in the HALO+ outlet. Preferably this is done within a short time and without any final offset. These conditions necessitate a relatively moderate PID control, with a proportional gain K_P small enough to prevent any considerable overshoot and a response time in the order of seconds. The time behaviour of the PID loop can be seen in figure 4.7 where different pressure conditions were simulated. The control circuit successfully kept a pressure difference of 700 mbar during different changes of conditions. The ladder diagram coding of the PID circuit in Machine Edition is attached in appendix A.

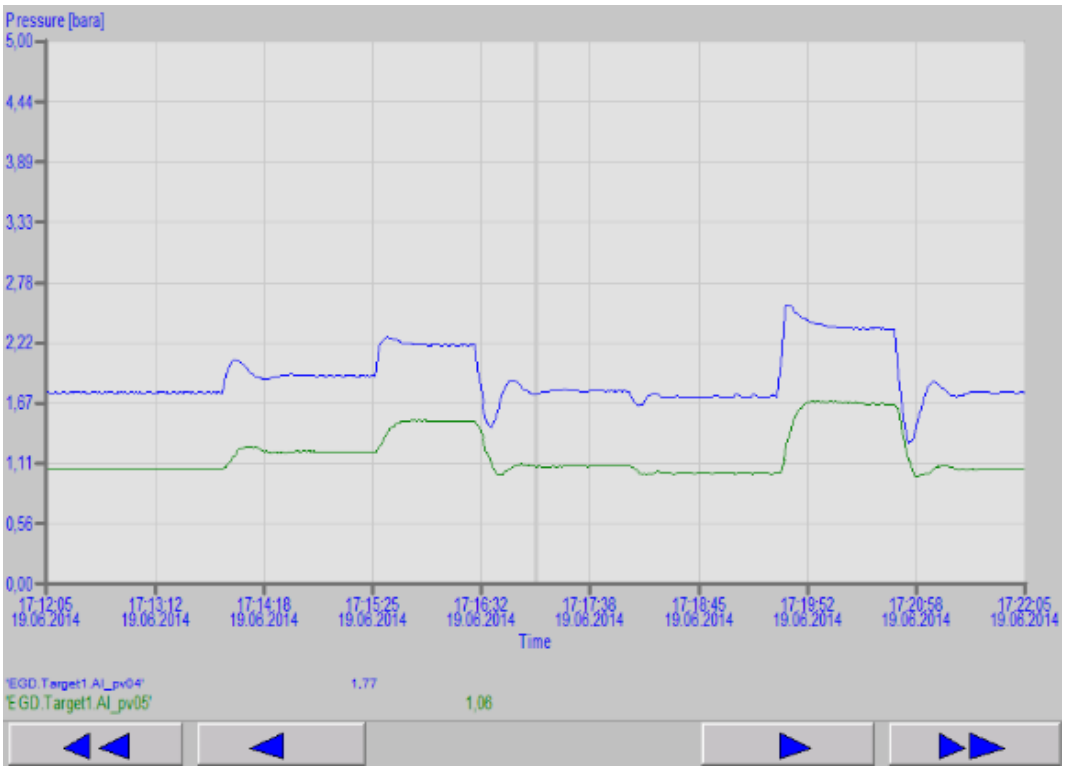

Figure 4.7: Time behaviour of inlet pressure (P204, blue) and outlet pressure (P205, green) while changing the inlet flow multiple times. The pressure difference of 700 mbar is accurately obtained within the order of seconds, even after rapid changes (compare t ≈ 17:19:30).

Chapter 5

A ^{83m}Kr detector for tracer diagnostics

The exceptionally well performing cryogenic distillation column regarding its removal of contaminating ^{85}Kr from xenon made an investigation of the separation efficiency intricate and time-consuming. In collaboration with the MPIK in Heidelberg a sensitive gas-chromatography technique was accessible, allowing to make statements about the krypton concentration on a ppq level [Lin14]. However these measurements require several days in order to produce significant results. On the other hand in particular during the commissioning phase of the distillation column the possibility of a live control of the separation efficiency was desirable. This especially motivated the development of an in-house diagnostic tool which, based on a ^{83m}Kr tracer method, allows a performance analysis during operation. In the following chapter its functional principle will be explained and its optimization will be described. In the course of this, the work on both the detector as well as the ^{83m}Kr emanator will be elaborated.

5.1 The ^{83m}Kr tracer method

Due to the relative long half-life of $t_{1/2}(^{85}\mathrm{Kr}) = 10.74\,\mathrm{a}$ and its extremely low concentration in xenon after cryogenic distillation (see chapter 3.4), a direct determination of the separation efficiency of the distillation column by detection of ^{85}Kr is not easily feasible. Doping it artificially with large amounts of ^{85}Kr is ruled out due to the long term contamination of the used xenon. However, this problem can be avoided by utilizing the metastable ^{83m}Kr as a tracer whose decay can be measured by using a photomultiplier tube, optimized for the scintillation light of xenon (as described in chapter 3.2). With a half-life of $t_{1/2}(^{83m}\mathrm{Kr}) = 1.83\,\mathrm{h}$, it is sufficiently stable for a distribution in a large system while at the same time decays quickly enough to the stable ^{83}Kr so that even without any removal, the used xenon will not be contaminated on a significant time scale. Moreover, since different isotopes of krypton behave chemically identical one can directly deduce the separation efficiency for the relevant ^{85}Kr by measuring the separation factor of ^{83m}Kr.

^{83m}Kr is obtained from the decay of ^{83}Rb (see fig. 5.1). ^{83}Rb disintegrates with a half-life of $t_{1/2}(^{83}\mathrm{Rb}) = 86.2\,\mathrm{d}$ through electron capture (EC), where an inner shell electron is captured by

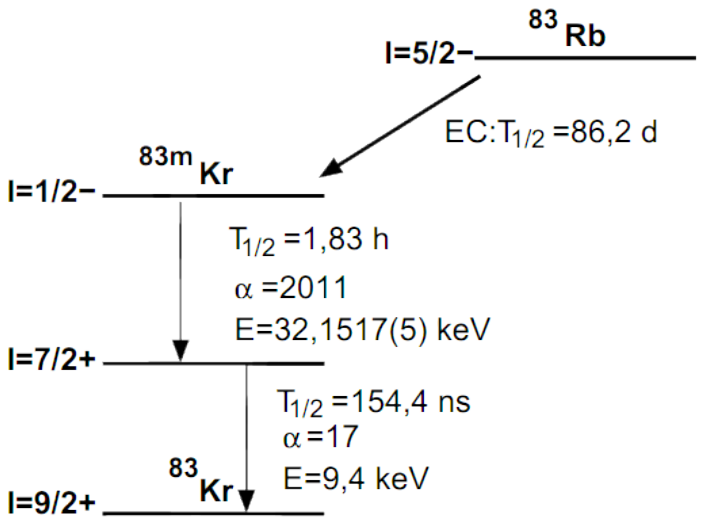

Figure 5.1: Decay branch of ^{83}Rb to the stable ^{83}Kr. With a probability of 77.6 % the decay goes over the radioactive ^{83m}Kr.[Ost08]

a proton. This leads to the conversion of the proton to a neutron while emitting an electron neutrino ν_e. With a branching ratio of 77.6 % the decay of ^{83}Rb leaves the resulting krypton atom in the short lived isomeric state ^{83m}Kr at 41.55 keV. ^{83m}Kr then successively disintegrates mainly via emission of conversion electrons with the energy of $E_1 = 32.15\,\text{keV}$ after a half-life of $t_{1/2}(32.15\text{keV}) = 1.83\,\text{h}$ and subsequently with an energy of $E_2 = 9.4\,\text{keV}$ after a half-life of $t_{1/2}(9.4\text{keV}) = 154.4\,\text{ns}$[Mcc15].

Conversion electrons are produced by the process of internal conversion (IC), where an inner shell electron gets ejected after the electromagnetic interaction with an excited nucleus through the exchange of a virtual photon. The deexcitation via IC competes with that of gamma decay. It is quantified with the internal conversion coefficient α which is defined as the ratio of the number of deexcitations via emission of electrons to the number of deexcitations via emission of gammas. Furthermore the IC can lead to the emission of Auger electrons, when the vacancy of the missing conversion electron is filled with a higher shell electron. ^{83m}Kr has an internal conversion coefficient for its first decay of $\alpha = 2011$, meaning with 99.95 % it deexcites almost exclusively by IC. Its second decay with $\alpha = 17$ is still dominated by IC with 94.4 % but occasionally the energy is carried by gamma rays.

In order to prevent the relatively long half-living ^{83}Rb from contaminating the system it was embedded in zeolite pellets with a pore size of 0.5 nm covered by a PTFE membrane with a pore size of 220 nm (as seen in figure 5.2). Zeolite is an aluminosilicate mineral with a crystal structure. It can trap ^{83}Rb as counter cation to the aluminosilicate anion. ^{83m}Kr on the other hand can be emanated from the zeolite through to its porous structure. Studies have shown that the source does not release ^{83}Rb at a detectable level[Han11] while ^{83m}Kr leaves the source nearly unattached[Ven05]. However, non negligible variations of the krypton emanating rate have been observed from different sources in further tests. They suggest an emanation rate of

Figure 5.2: *Left:* ^{83}Rb source embedded in zeolite pellets. *Right:* Top of the rubidium source with the protective PTFE membrane filter[Han11].

^{83m}Kr for the source used in Münster to be $\epsilon = (70 \pm 5)\%$.
In the process of doping, the ^{83}Rb source linked to the gas system through a VCR connection is opened and ^{83m}Kr is introduced by diffusion and the suction effect of the bypassing gas. Its subsequent decay can be detected locally with a custom made ^{83m}Kr -detector which can be integrated in the gas system and utilizes the scintillation properties of gaseous xenon (see chapter 3.2). Considering the CSDA (continuous slowing down approximation) range of electrons with energies in the order of 30 keV one can calculate that a detector volume of only a few cubic centimeter filled with GXe at atmospheric pressure p = 1.01325 bar is sufficient enough for an approximate complete energy deposition within the detector. This is also the case for a decay by emission of gammas with energies up to 10 keV, considering mainly the decay from the very short lived 9.4 keV level of ^{83m}Kr (due to the high internal conversion coefficient of the first decay $\alpha(41.55\,\text{keV}) = 11$). From the mass attenuation coefficient of these photons one can calculate a mean free path of ∼1 cm[Ros14]. Hence in the developed ^{83m}Kr T-detector, a R8520-06-Al Hamamatsu® photomultiplier tube monitors the doped GXe passing through a perpendicular stainless steel tube with an inner diameter of 40 mm (see figure 5.3). In front of the PMT a PTFE foil, which is highly reflective for the scintillation light of GXe, covers the interior of the T-piece in order to increase the light yield.
For determining the separation efficiency of the cryogenic distillation column several of these T-detectors were built and installed at different positions of the system. By placing a ^{83m}Kr -monitor at the input-, at the output- as well as at the off-gas line of the column, the tracer method allows to monitor the time behaviour of the krypton concentration during the actual distillation process.
Furthermore, the ^{83m}Kr detector was tested on a closed loop circulation in the gas purification system driven by a membrane circulation pump. With the addition of a special pipette connected to the ^{83}Rb source a bunched doping was possible. After introducing the ^{83m}Kr bunch into the closed loop system, the T-detector allowed to reconstruct the gas flow very precisely. This allows e.g. a calibration of mass flow controllers since from the oscillation the mass flow can be deduced with knowledge about the system volume[Ros14].

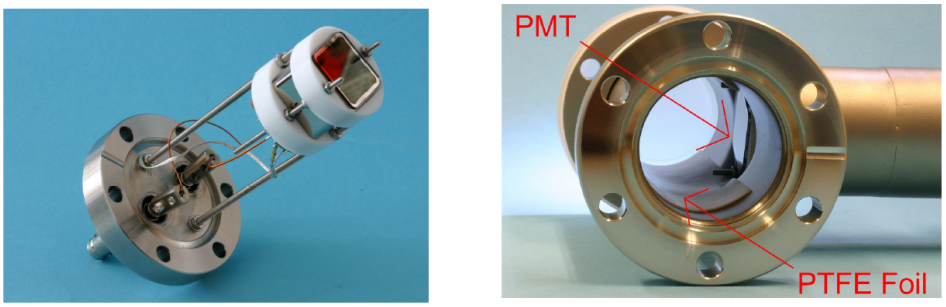

Figure 5.3: *Left:* Photomultiplier tube mounted with a PTFE holder to a CF-40 feed-through flange to provide high voltage and signal read-out. *Right:* Inner view of ^{83m}Kr detector with visible PMT and reflective PTFE foil[Ros14].

5.2 A ^{83m}Kr cross-detector for enhancement of sensitivity

Despite the success of the ^{83m}Kr T-detector in showing the functioning of the cryogenic distillation column as well as accurately describing the dynamics of the gas system, an enhancement of the sensitivity of the ^{83m}Kr detector was desirable. The relatively high background rate of several Hz made the detection of very low ^{83m}Kr concentrations not feasible since these measurement would be dominated by the background. By upgrading the detector to a X-detector, where two PMTs monitor the same volume, a significant decrease in background can be expected due to the possibility of measuring coincidence events. In the following the origins of background shall be described before different approaches of its reduction will be presented.

5.2.1 Functional principle and sources of background of photomultiplier tubes

The principle of a PMT is based on the photoelectric effect combined with the multiplication of charge by using a dynode structure. If the energy of a photon is greater than the work function of a material, the photon can break the bond between an electron and the nucleus and create a free electron. Since the photoelectric effect is quantum in nature, it follows a probabilistic distribution. The quantum efficiency (QE) of a PMT quantitatively describes the probability of an incident photon liberating a photoelectron and is defined as $QE(\nu) = N_{pe}/N_{ph}$. The R8520-06-Al PMT with an effective area of 20.5x20.5 mm^2 has a quantum efficiency for the scintillation light of xenon of $QE(171\,\text{nm}) \approx 30\,\%$[Apr12c].

Electrons emitted in the photocathode are accelerated onto the first dynode by a high electric field and a focusing electrode. As seen in figure 5.4 the electric field is separated by several dynodes with a cascading potential. In every dynode an electron can release several secondary electrons, depending on the applied electric field and the kinetic energy of the electron. By this avalanche effect even low energy photons can generate a measurable current at the anode, allowing to count single photons. The final current signal follows approximately a Gaussian distribution due to the statistical process of secondary electron emission.

The background rate of a PMT can be differentiated by its origin[Ham06][Fly02]. Categorized as

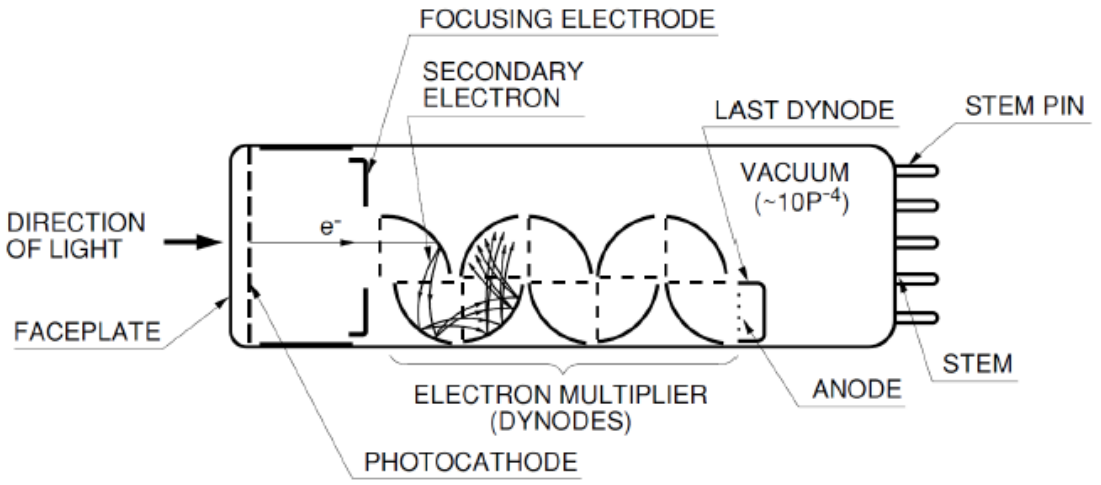

Figure 5.4: Sketch of a PMT showing the basic principle of multiplying charge with a dynode structure[Ham06].

dark current effects are effects leading to an electric current even though in absence of any form of light. Depending on the applied voltage different effects dominate this form of background. Leakage currents, a continuous component which is especially dominating the low voltage regime, is caused by the surface conductivity of the insulating material and follows roughly a linear behaviour defined by Ohm's law $I = U/R$.

At typical working conditions of PMTs the dominating component is the thermionic emission. Due to the very low work function of the photocathodes and dynodes surface material in PMTs, already at room temperature electrons can have enough kinetic energy in order to escape the material. Thermionic emission follows Richardson's law, which describes the current density J as

$$J = AT^2 e^{\frac{-W_{th}}{k_B T}}, \tag{5.2.1}$$

where k_B is the Boltzmann constant, A is the material dependent Richardson constant and W_{th} is the thermionic work function. The latter is a function of the potential depth U of the material and the Fermi level E_F

$$W_{th} = U - E_F \tag{5.2.2}$$

and is therefore also a function of the applied voltage.

At even higher voltage ($> 1\,\mathrm{kV}$) field emission causes a significant increase in dark current. Here, the electric field is strong enough to directly pull out electrons from the cathode material. Since applying voltages in this region shortens the life of the PMT, the manufacturer states a maximum supply voltage which is sufficiently low to prevent field emission ($\mathrm{V_{max}} = 900\,\mathrm{V}$ for R8520-06-Al). In figure 5.5 the typical dark current plotted against the supplied voltage is shown.

Additional but typically less significant dark current effects are scintillation from the PMTs

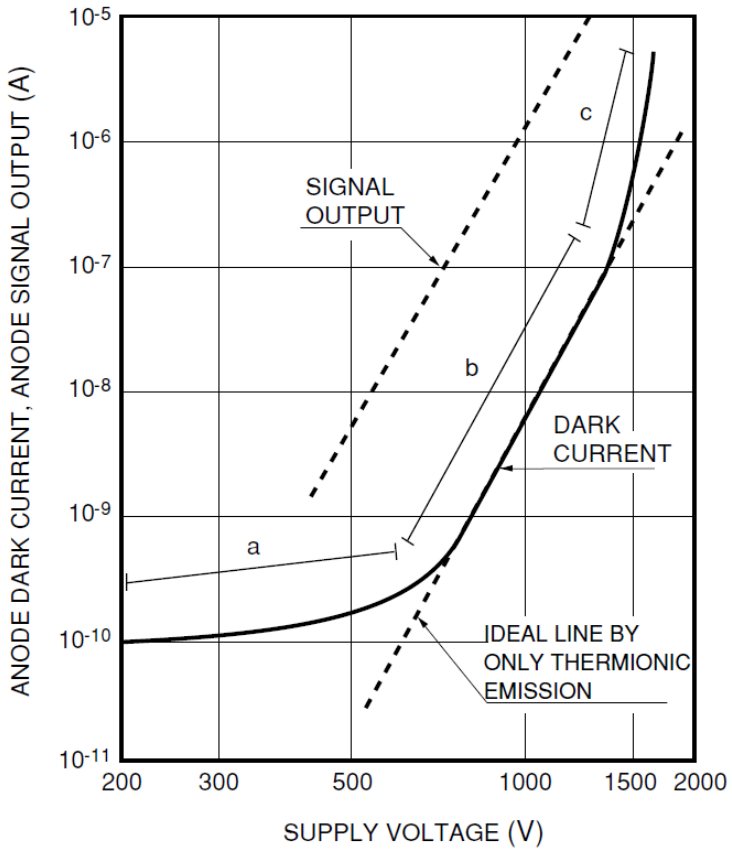

Figure 5.5: Typical dark current vs. supply voltage characteristic [Ham06]. Region (a) is dominated by leakage current, (b) is mostly dominated by thermionic emission whereas in (c) field emission increases the dark current abruptly.

housing material, excited through external radiation, as well as the so called "afterglowing". The latter describes the ionization of residual gas molecules inside the PMT which can lead to a delayed pulse in the range of ~ 100 ns to several μs. Although with a vacuum of $10^{-7} - 10^{-8}$ mbar inside the PMT the amount of residual gas is kept at a minimum, it can be a serious issue. Especially exposure to helium can cause a significant afterglowing because it can migrate through the glas shielding.

A typologically different effect, which contributes to the final background, is the excitation of the scintillation material in front of the PMT through ambient radiation. Here above all cosmic muons and decay products from the buildings material (e.g. concrete) can cause scintillation events inside the detection volume and thereby potentially mimicking an actual tracer decay event.

Finally electronic noise can potentially contribute to a background level. However if care is taken to properly ground and shield the electronics, the high gain of the PMT allows to easily deal with this issue by setting an internal threshold to the equivalent of a single photon event.

5.2.2 Design and construction of a X-detector

The previously described effects, leading to a non-negligible background are fundamental physical effects which cannot easily be eliminated. However, a major part of the background effects can be identified as such by the method of coincidence measurement. Through monitoring a scintillator simultaneously with two PMTs and interconnect them via a logical "AND" circuit, where only events are considered which both PMTs detect, an efficient discrimination of dark current induced events can be achieved as they only cause a signal in one PMT at a time.
Therefore, the T-detector described in chapter 5.1 was upgraded to a X-detector (see figure 5.6-5.7) in order to allow coincidence measurements. The stainless steel crosspiece was built with the same key parameters to facilitate a quick implementation of the already used components from the T-detectors to the new cross-detector. Two perpendicularly crossing stainless steel tubes with an inner diameter of 40 mm are each enclosed with two CF-40 endings. The PMT holding tube is deliberately longer to support the holding structure of the PMTs as they were used in the T-detector where two threaded rods, which are attached to a CF-40 flange, fixate the PMT through a PTFE casing (as seen left of figure 5.3). The flange contains two SHV connections for the high-voltage supply of the PMT and its signal output. Since with this configuration two PMTs are facing each other, the design of the inner reflective PTFE foil had to be reconsidered. The hydrophobic flourcarbon PTFE is well known for its excellent reflectivity of $\sim 99\,\%$ in the optical range[Lus10]. For VUV (vacuum ultraviolette) light, as emitted by xenon dimers during scintillation, PTFE still shows good reflectance but its reflective properties are not completely understood and are a subject of intensive investigation within the XENON collaboration. Its reflectivity is strongly depending on the exact manufacturing process as well as possible subsequent polishing processes. For VUV light it lies typically between ~ 50 - $75\,\%$[Sil10]. In general a reflection of a surface is a combination of contributions from specular and diffuse reflection.
Since PTFE is produced from a highly compressed powder, its micro-surface is typically uneven which leads to a predominantly diffuse reflection[Lev14]. The diffuse reflection is a good approximation for the PTFE samples prepared by the mechanical workshop in the University of Münster due to the polishing treatment using a milling head with a bore oil emulsion.
The process of diffuse reflection approximately follows Lamberts cosine law, which states that the light intensity I in a solid angle $d\Omega$ is proportional to the cosine of the angle of reflection θ_R to the normal of the surface

$$\frac{dI(\theta_R)}{d\Omega} \propto I_0 \cdot cos(\theta_R). \tag{5.2.3}$$

This is illustrated in figure 5.8, including the competing specular reflection process described by $\theta_I = \theta_R$. The majority of reflected photons are consequently found around the normal of the reflecting surface. Since in the X-detector the PMTs are facing each other, the most significant contribution in reflectivity would be lost by simply cutting out the segment of the PTFE foil which is covering the inner surface of the tube at the position of the opposite PMT.

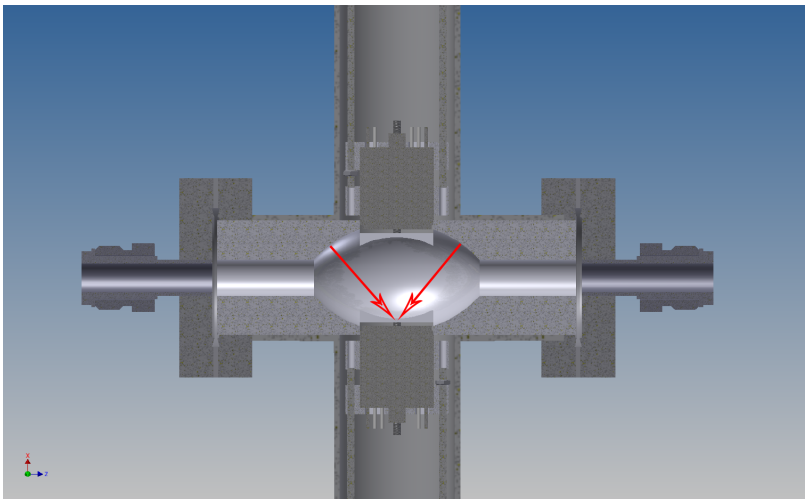

Figure 5.6: Technical drawing with inner view of the X-detector. The PMTs are positioned vertically, monitoring the horizontally passing GXe in a detection volume, defined by the hollowed corpus made of reflective PTFE. The corpus is specially processed, so the normal of the surface (indicated by red arrows) is pointing towards the opposite PMTs.

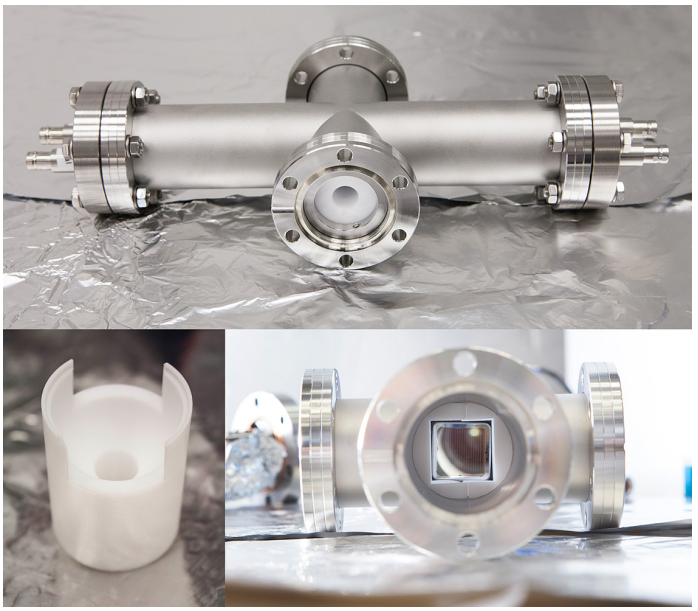

Figure 5.7: *Top:* Picture of the X-detector with the two PMTs and their holding structure installed left and right. The gas flow will be routed vertically in this orientation. At the entrance the PTFE reflector and its ringform mounting is visible. *Bottom left:* One of two segments of the reflective PTFE corpus. The element is hollowed along the axis by a 1/2" tube and spherical-like at the end so that a high fraction of the surface normal is pointing towards the opposite PMT. *Bottom right:* The rectangle stamps created by the two PTFE segments as positioning for the PMTs can be seen in the view through the horizontal tube.

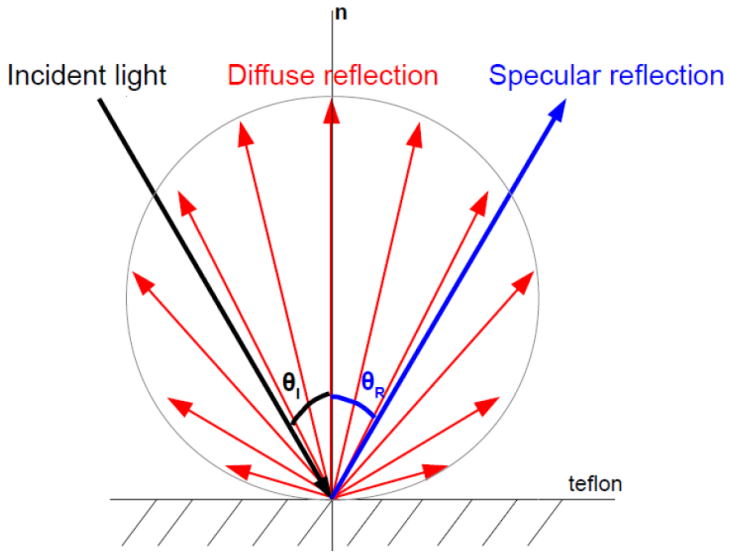

Figure 5.8: Schematic drawing of the specular (blue) and diffuse (red) reflection process[Lev14].

Instead a PTFE corpus made out of two hollowed cylinders was designed (see bottom left of figure 5.7). When put together they form an inner detection volume of 37.2 cm^3 where the surface normal is largely directed towards the PMTs. A technical drawing of the X-detector with the reflecting PTFE corpus can be seen in figure 5.6, where the normal of the surface was indicated with a red arrow. In consequence of the curvature of the corpus, the potential detection volume however decreased significantly. Contrary to the X-detector, especially when considering the reflection of the inner PTFE foil, the T-detector could in principle detect a photon from any point inside the cylindrical volume of the horizontal tube and thereby monitor a volume of 132(9) cm^3. However, measurements of the performance of this detector type (see [Sch12]) revealed a considerably smaller effective volume of $\sim 16\,cm^3$. A direct comparison of this value with the following measurements has to be taken with care, among others due to different purity of the used xenon in both cases. It does however indicate that the decreasing potential detection volume at the far end of the tube will not greatly impact the detection efficiency of the X-detector.

5.2.3 Measurement of the relative detection efficiencies of four T-detectors

Before reallocating two PMTs into the X-detector the four available T-detectors were examined regarding their relative detection efficiency. Therefore they were installed in series in the gas circulation system in the IKP Münster. This allowed for a comparison at identical conditions and for a simple reference measurement after implementing the X-detector in this ^{83m}Kr -monitor line. A schematic of the gas system including the implemented ^{83m}Kr -monitor line with its data acquisition (DAQ) system can be seen in figure 5.9. It shows the state of the system as it was operated when testing the detectors. During the initial reference measurement instead of the X-detector, two additional T-detectors were installed in the detector line.

A circulation pump (*QDrive*®) constantly circulated GXe at ∼2-3 bar through the setup of zirconium getter and detector line in order to provide clean GXe for an optimal light yield. For testing the detectors the ^{83}Rb-source was opened for typically ∼10 s, thereby introducing ^{83m}Kr as a tracer. High voltage of +800 V was supplied by the *iseg*® VDS8130p module in order to operate the PMTs in a high gain mode ($\mathcal{O}(\sim 10^6)$). After amplification with a voltage gain of x10 through a Fast-Amplifier (CAEN® Mod. N979), their analog voltage signal output was digitized by a flash analog-to-digital-converter (ADC) (CAEN® Mod. V1724). The 8 channel ADC is a 14-bit digitizer with a voltage range of 2.25 Vpp (voltage peak-to-peak). The conversion of its outputted ADC entities to voltage is therefore

$$1\,\mathrm{ADCE} \mathrel{\hat{=}} \frac{2.25\,\mathrm{Vpp}}{2^{14}} = 0.137\,\mathrm{mV}. \tag{5.2.4}$$

With a sampling frequency of 100 MHz and an acquisition window of 512 samples, an event window corresponded to 5.12 μs. Due to the strong activity of the ^{83}Rb-source (18.548 MBq on the 01.01.2015) the DAQ system would quickly oversaturate when opening the source for a longer period of time, thereby induce a dead-time caused loss of detection efficiency. In order to be able to detect an oversaturation a pulse generator was connected to the ADC, producing a constant rate of 100 Hz which would decrease in case of saturating rates. The digitized signal was finally processed with a DAQ software package developed at KVI Groningen, controlled by the Java-based program FPPDAQ written by Volker Hannen.

In the acquisition window of 5.12 μs a GXe scintillation event occupies only a small width, with typically $\lesssim$100 ns. Hence the majority of the signal is sole electronic noise around the baseline with no physical relevance. The FADC from CAEN® provides a zero length encoding (ZLE) algorithm which allows to reduce the data size of events significantly by only recording a small adjustable window around a signal peak above a software set threshold. The remaining signal is recorded as the length of "null signal" rather than as a data point for each sample (examplary waveforms can be seen in figure 5.14 chapter 5.2.5). This allows to make long-term measurements at fairly high event rates ($\sim \mathcal{O}(100\,\mathrm{Hz})$) without producing unmanageably large data files.

Since the initial reference measurement of the four T-detectors was simultaneously supposed to be a cross check for the long-term drifting behaviour of the PMTs for the PhD thesis of S. Rosendahl [Ros15], the measurement was done with settings used during the operation of the cryogenic distillation column. All four PMTs were read out with the same threshold of 30.5 mV ($\hat{=}$ 222 ADCE) during circulation of GXe at a pressure of 2.3 bar with a flow of 7.6 slpm. Initially a background measurement of 25 min was performed. The result can be seen in figure 5.10 where the measured background rates are presented in binned-form for each minute of measurement. The uncertainties of the respective bins come from their standard deviation $\sigma = s_{N-1}/\sqrt{N}$ where $N = 60$ is the number of measurements within one bin. The data was analysed with the C++ based analysis framework ROOT and fitted with a constant function to deduce the mean background.

This graphical analysis was deliberately used in order to be able to detect possible drifts of the PMTs. Although all four background rates are stable around a constant value, except for *PMT4*

.

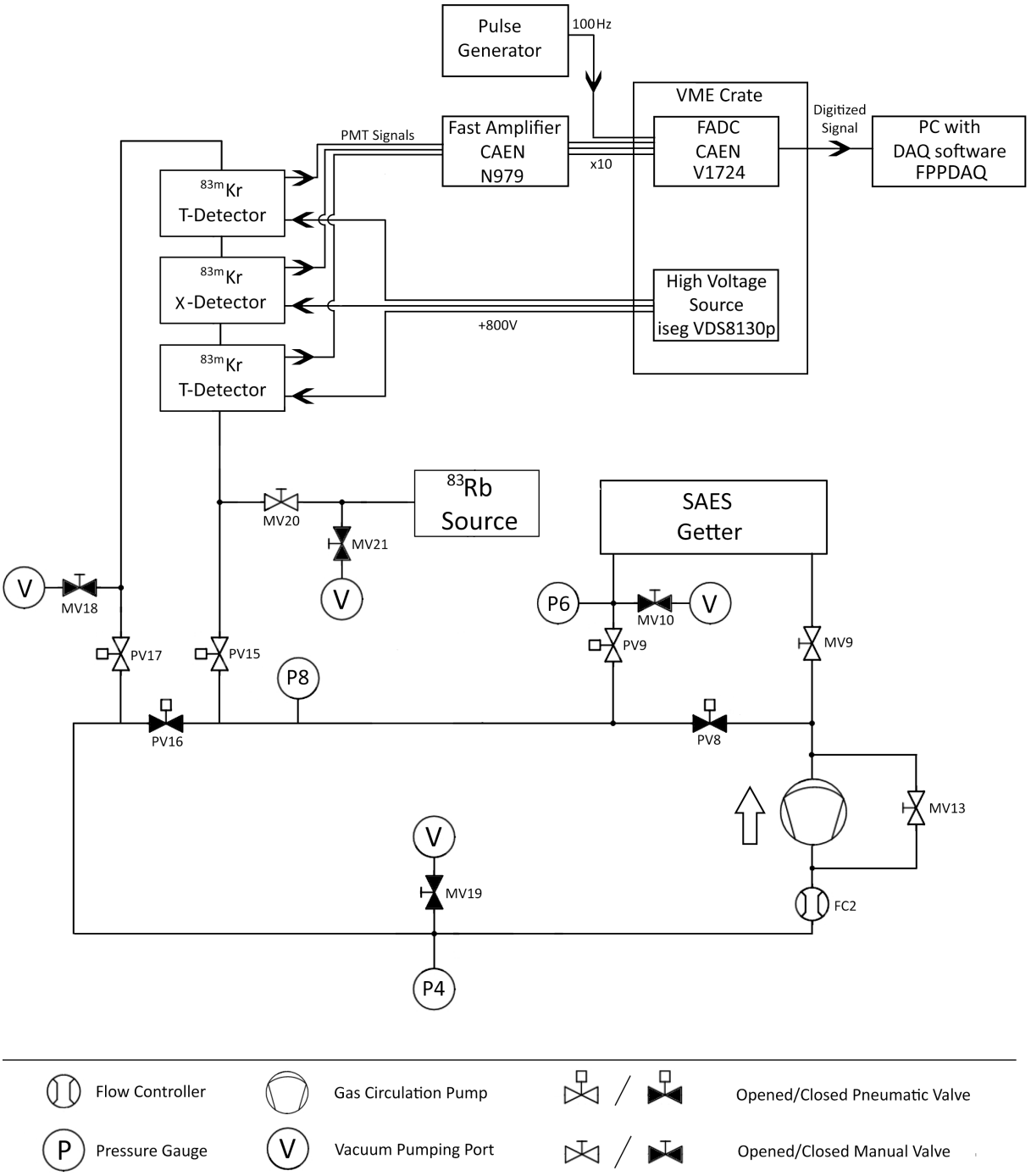

Figure 5.9: Flowchart and diagram of the DAQ system of the gas circulation system segment as utilized for the ^{83m}Kr -detector tests in the IKP Münster.

the fits show small deviations from their optimal value of the reduced chi-squared χ^2_{red}. They were obtained through ROOTs fitting routine MIGRAD using the method of least square minimization where χ^2_{red} allows a statement about the goodness of a fit. If the fluctuations of the background rates would be caused solely by statistical gaussian fluctuations one has to expect a value in the region depending on the number of degrees of freedom *ndf*

$$\chi^2_{red} = 1 \pm \sqrt{2/ndf}. \tag{5.2.5}$$

A significantly from 1 deviating χ^2_{red} can principally be caused by an under- or overestimation of uncertainties as well as by systematic uncertainties. In the following analysis however, indication for a systematic cause will be presented.

After the background measurement the ^{83}Rb-source was opened through the source valve *MV20* to introduce ^{83m}Kr into the gas system and closed at $t = 45$ min. The result can be seen in figure 5.11.

The relatively long doping time was caused by the overpressure in the gas system relative to the ^{83}Rb-source which was due to a previous measurement, done at $p = 1.77$ bar with an opened source valve *MV20*. This is in agreement with the long diffusion time of krypton in static gaseous xenon which was examined in [Fie14]. After an increasing rate during doping with ^{83m}Kr, the measured rate decays exponentially shortly after the source valve was closed. By fitting the signal data with an exponential decay function with a constant background B

$$f(t) = B + S_0 \cdot e^{-\lambda \cdot t} \tag{5.2.6}$$

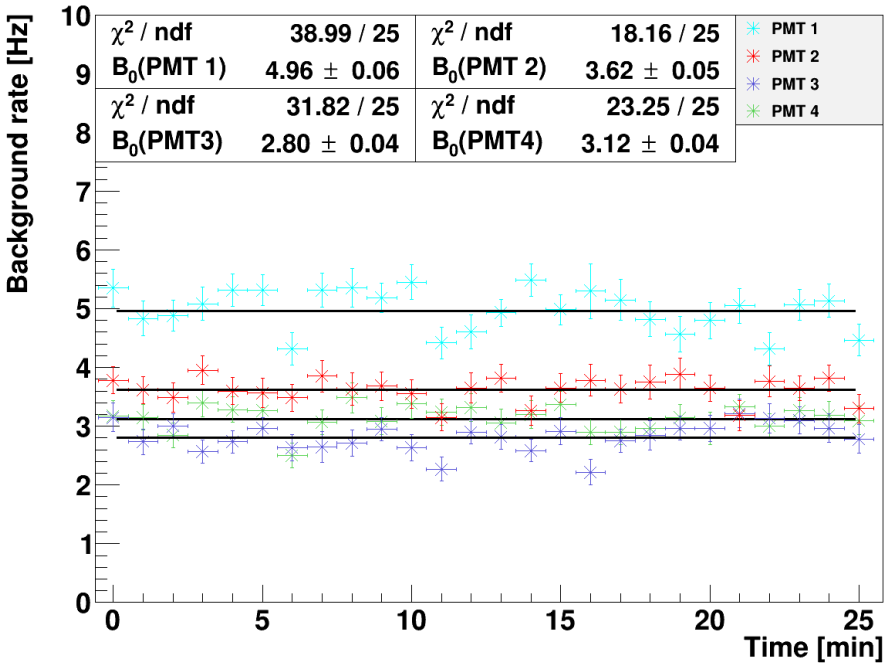

Figure 5.10: Background measurement of four T-detectors before opening ^{83}Rb-source.

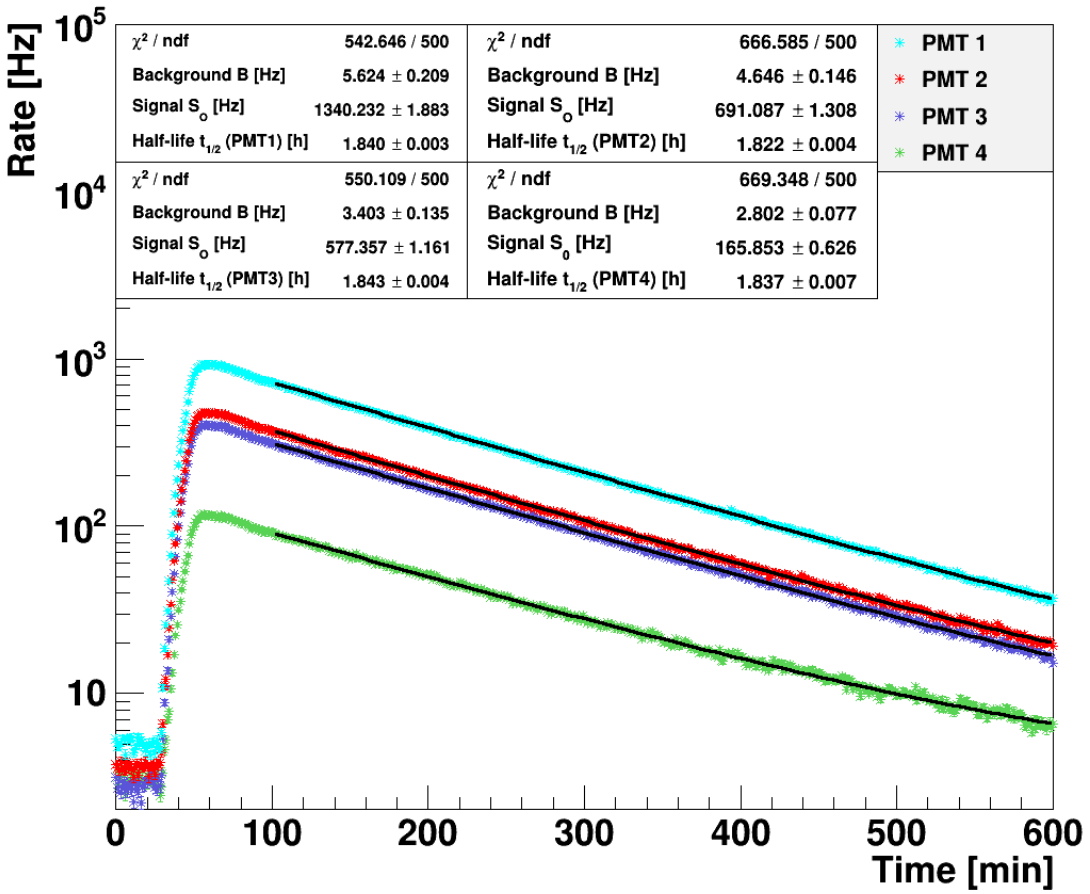

Figure 5.11: Logarithmically plotted event rate measured with four T-detectors installed in series while doping with ^{83m}Kr. At t = 25 min the ^{83}Rb-source is opened and closed at t = 45 min in order to prevent the DAQ from an oversaturation. After an equal distribution of the introduced tracer, the event rate decays exponentially with a half-life in agreement with the decay of ^{83m}Kr.

where $\lambda = \ln(2)/t_{1/2}$, the half-life of the introduced tracer could be determined and agrees in all four measured datasets with the literature value of ^{83m}Kr ($t_{1/2} = 1.83(2)$ h). Again, one has to note that the χ^2_{red} deviates slightly from the optimal $\chi^2_{red} \sim 1$.

Furthermore, significantly different detection efficiencies for ^{83m}Kr of the four T-detectors were observed. This can be explained with variations in the quantum efficiency as well as different gains under application of the same voltage and threshold within different PMTs. For the cross-detector, *PMT2* and *PMT3* were chosen due to their similar detection efficiency while *PMT1* and *PMT4* were used as reference. When normalizing their background reduced ^{83m}Kr signal rates to e.g. *PMT1*, the correction factor $C_{i,1} = r_i(^{83m}\text{Kr})/r_1(^{83m}\text{Kr})$ in respect to *PMT1* can be deduced. Due to identical thermodynamic and geometric conditions in all four detectors, this corresponds to the relative detection efficiency $\epsilon_{i,1} = C_{i,1}$ (see figure 5.12). Again the graphical analysis was performed in order to be able to observe a possible change in the relative detection

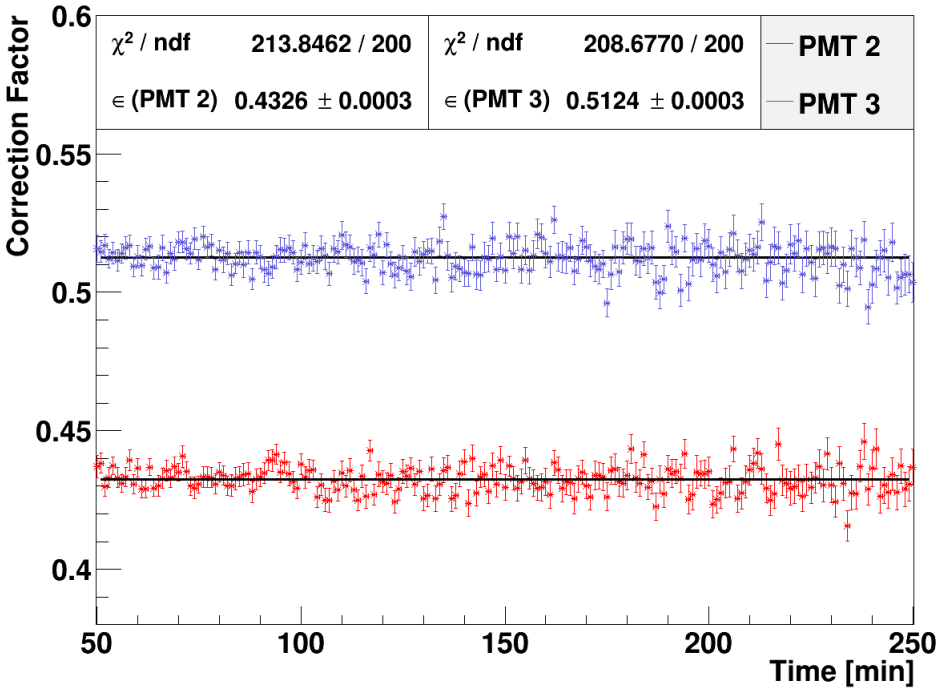

Figure 5.12: Backround reduced correction factors of *PMT2* and *PMT3* in respect to *PMT1*.

efficiency at different signal rates. The relative detection efficiency was determined in respect to both *PMT1* and *PMT4* to allow a stronger statement. These values will later on be compared to the values measured in the cross-detector to directly show the effect of the new inner geometry. The normalization regarding *PMT1* is shown in figure 5.12 where its uncertainty of the bins is determined by the propagation of uncertainty. It is listed in table 5.1 together with the measured background rates and the normalization regarding *PMT4*. The constant fit over the ratio of the background reduced ^{83m}Kr signal rates fits the correction factor well for a broad measurement window of over 3 h during a decreasing rate, suggesting that the relative detection efficiency is independent of the absolute rate. Furthermore, since the ratio of the rates give $\chi^2_{red} = 1 \pm \sqrt{2/ndf}$ the before made assumption of a systematic component in the uncertainty seems plausible.

Table 5.1: Results of the reference measurement with four T-detectors

	Background [Hz]	Relative Detection efficiency $\epsilon_{i,1}$ with respect to PMT1	Relative Detection efficiency $\epsilon_{i,4}$ with respect to PMT4
PMT2	3.62(5)	0.4326(3)	3.520(5)
PMT3	2.80(5)	0.5123(4)	4.169(6)

5.2.4 Effect of the PTFE corpus on the detection efficiency

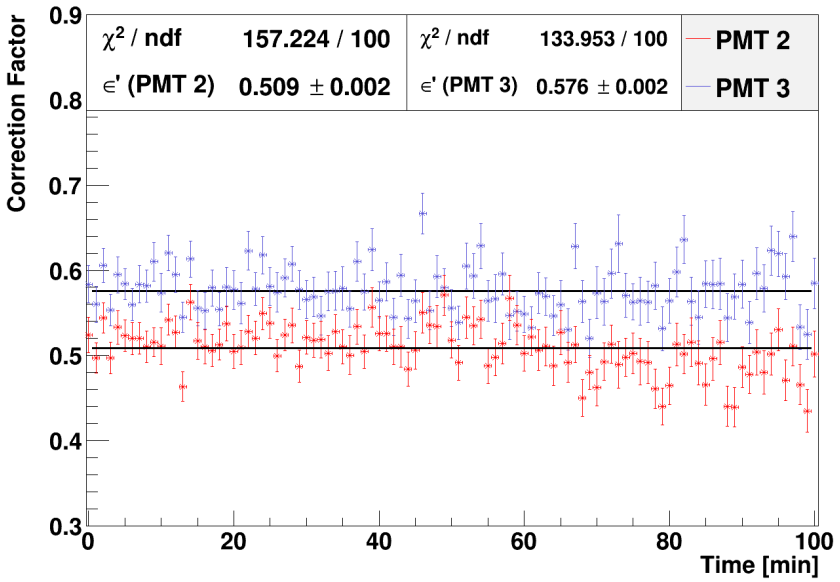

Figure 5.13: Background reduced correction factors of *PMT2* and *PMT3* in respect to *PMT1* during operation in the X-detector.

After assembling the X-detector with the new inner PTFE corpus and the two PMTs, the measurement was repeated first without a coincidence circuit (which will be discussed in following the chapter 5.2.5). By replicating the measurement in this "single"-mode with as much as possible identical settings the effect of the PTFE corpus on the detection efficiency can be directly observed. GXe at a pressure of $p = 2.04\,\text{bar}$ was circulated through the detector line and the purifying unit at a flow of $F = 7.4\,\text{slpm}$ for 24 h before starting a measurement in order to obtain a comparably high light yield and allow the PMTs to sufficiently stabilize. They were furthermore read out with the same threshold of 30.5 mV.

The results of the background reduced correction factors deduced from the same graphical analysis as described in chapter 5.2.3 can be seen in figure 5.13. Although providing a potentially smaller detection volume, the measurement with the hollowed PTFE corpus shows in fact a noticeable increase in detection efficiency Σ of 18.4 % and 13 % respectively as a result of the specially shapped surface. The determined detection efficiencies are listed in table 5.2 where the change in efficiency $\Delta\Sigma = \epsilon'/\epsilon$ is the average of both normalizations to *PMT1* and *PMT4*.

Table 5.2: Relative detection efficiency of the PMTs installed in the X-detector

	Relative detection efficiency $\epsilon'_{i,1}$ in respect to PMT1	Relative detection efficiency $\epsilon'_{i,4}$ in respect to PMT4	Change in detection efficiency $\Delta\Sigma$[%]
PMT2	0.509(2)	4.19(4)	+ 18.4(6)
PMT3	0.576(2)	4.73(5)	+ 13.0(7)

5.2.5 Background reduction by coincidence measurement

In order to significantly reduce the background rate in the X-detector, a coincidence analysis was performed as postprocessing of the initial "single"-mode measurement. This allowed a direct comparison of the background of the X-detector within a single measurement and hence a straightforward determination of the background reduction factor while at the same time examine the ^{83m}Kr signal acceptance factor for the same measurement. Hence, similarily to chapter 5.12 a measurement was performed where after a 30 min background measurement the ^{83}Rb was opened to the gas system (see figure 5.15). Two points of increase in the measured rate are visible (at $t = 30$ min and $t = 45$ min) because the ^{83}Rb-source was opened a second time due to the fact that the first doping did not introduce sufficiently enough ^{83m}Kr. Shortly after, the ^{83m}Kr signal rate was measured during its exponential decay where later on the waveform of every event was analysed for coincidences.

In order to fulfill the coincidence criterium a peak finding algorithm looked for a peak in the waveform of *PMT2* within a window of ± 100 ns of the detected peak position in the waveform of *PMT3*. Figure 5.14 shows two examplary events. On the left a coincidence event is shown which was recorded after doping with ^{83m}Kr. In each channel two delayed peaks appear that are likely caused by the subsequent decay of ^{83m}Kr. On the right an event is shown which is discriminated by the coincidence logic since only one PMT caused a signal.

Applying this coincidence analysis on a background measurement leads to a reduced background rate of $B_{\mathrm{X,coin}} = 1.07(2)$ Hz. By forming the ratio of the coincidence rate against the initial

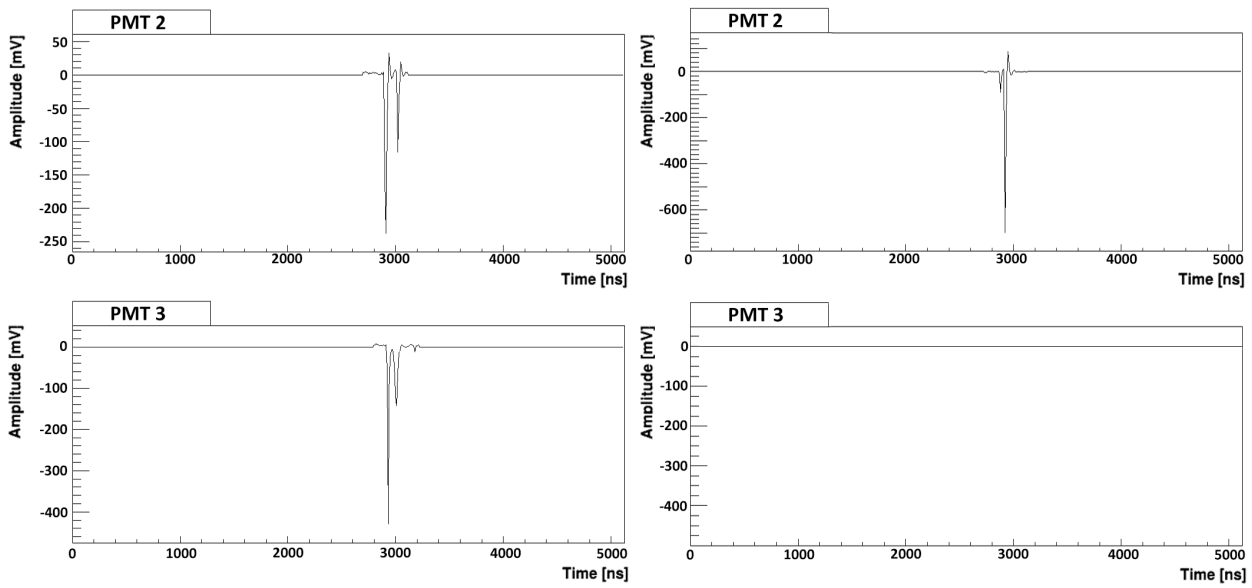

Figure 5.14: *Left:* Examplatory waveform of a coincidence event measured in both X-detector channels during doping with ^{83m}Kr. The two peaks are very likely caused by the subsequent decay of ^{83m}Kr. Due to the use of ZLE (zero-length-encoding) the baseline appears smooth without any electric noise. *Right:* Event discriminated by the coincidence analysis. While *PMT2* triggered, the opposite *PMT3* did not produce any signal above threshold.

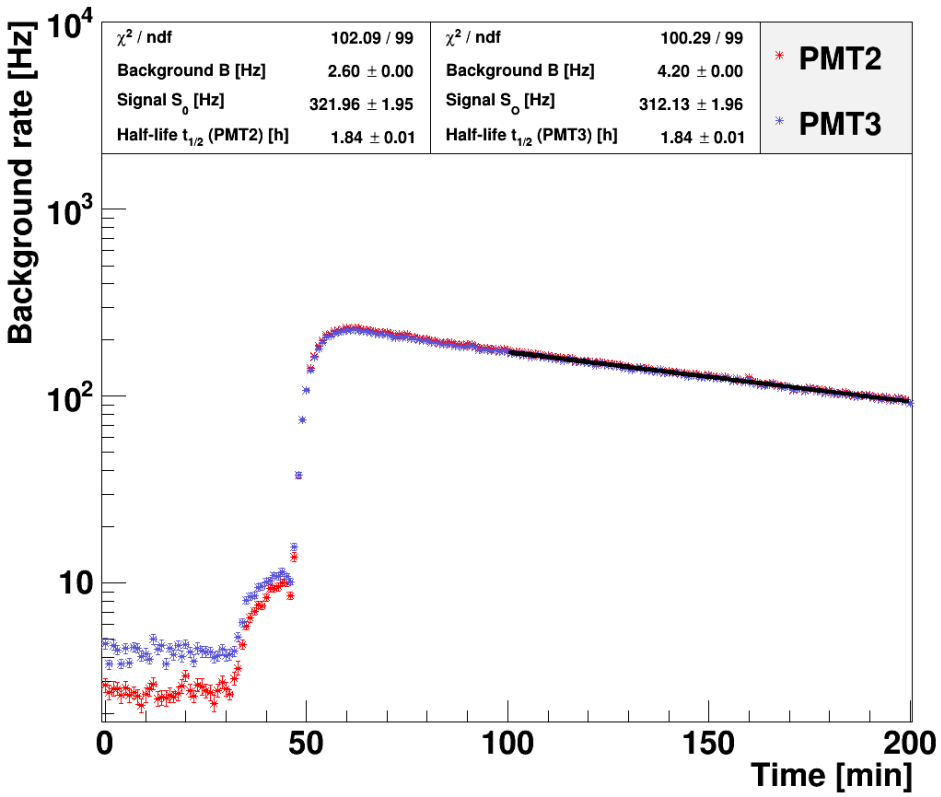

Figure 5.15: Measured rates with the X-detector in "single"-mode during doping with ^{83m}Kr. The ^{83}Rb was opened twice to introduce more ^{83m}Kr. The exponential fit was performed with a fixed background, determined from the initial background measurement.

"single"-mode rate of the background measurement one can obtain a background reduction factor

$$R_{B,i} = 1 - \frac{r_{B,\text{coinc}}}{r_{B,\text{single},i}} \tag{5.2.7}$$

for both PMTs (see figure 5.17). Care has to be taken regarding their uncertainties. Under assumption of a full solid angle $\Omega_i = 4\pi$ in the X-detector, with a real background rate $r_{B,\text{X}}$, the measured coincidence rate $r_{B,\text{coinc}}$ is

$$r_{B,\text{coinc}} = r_{B,\text{X}} \cdot \epsilon_2 \cdot \epsilon_3. \tag{5.2.8}$$

Hence the uncertainty of the background reduction factor $\Delta R_{B,i}$ is a correlated quantity. When fixating the background rate $R_{B,2}$, the coincidence rate can be written as $r_{\text{coinc}} = \epsilon_2 \cdot R_{B,2}$ which is a binomial distributed quantity with $r_{\text{coinc}}(k) = p^k q^{R_{B,2}-k}\binom{R_{B,2}}{k}$. From the variance of a binomial distribution $\sigma^2_{Bino} = n \cdot p \cdot q$ the uncertainty of the correlated background reduction factor is determined by

$$\Delta R_{B,i} = r_{B,i} \cdot \sqrt{\frac{R_{B,i}(1 - R_{B,i})}{r_{B,j\neq i}}}. \tag{5.2.9}$$

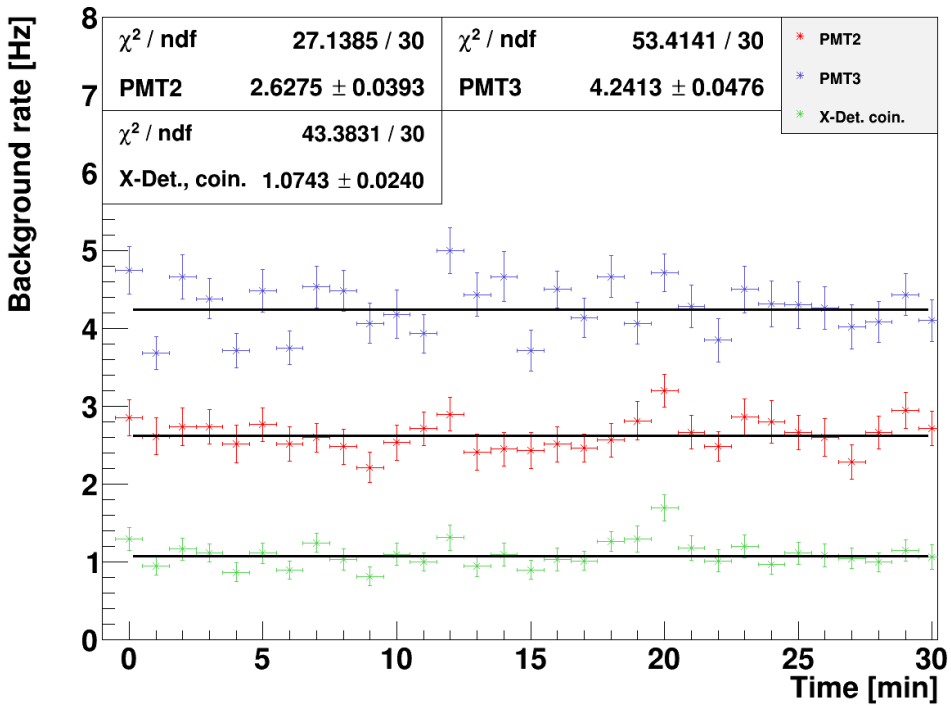

Figure 5.16: Background of the cross-detector in "single"-mode (*PMT2*/*PMT3*) as well as using the coincidence criterium.

After background reduction of the subsequently measured ^{83m}Kr signal rate one can likewise obtain a signal acceptance factor $A_{S,i} = r_{S,\text{coinc}}/r_{S,\text{single},i}$ (see figure 5.18). The results are listed in table 5.3. Although the coincidence mode reduced the background rate significantly, the X-detector still shows a detectable background rate of $B_{\text{X,coin}} = 1.07(2)\,\text{Hz}$. Since dark current effects can be excluded by the coincidence condition, the measured rate has to be caused by real scintillation events in the GXe. The reduction of this background will be the topic of the following sections.

Table 5.3: Background reduction and signal acceptance of the cross-detector in coincidence mode

	PMT2	PMT3
Coincidence background in X-detector [Hz]	1.07(2)	1.07(2)
Background reduction factor	0.578(4)	0.743(4)
Signal acceptance factor	0.885(1)	0.912(1)

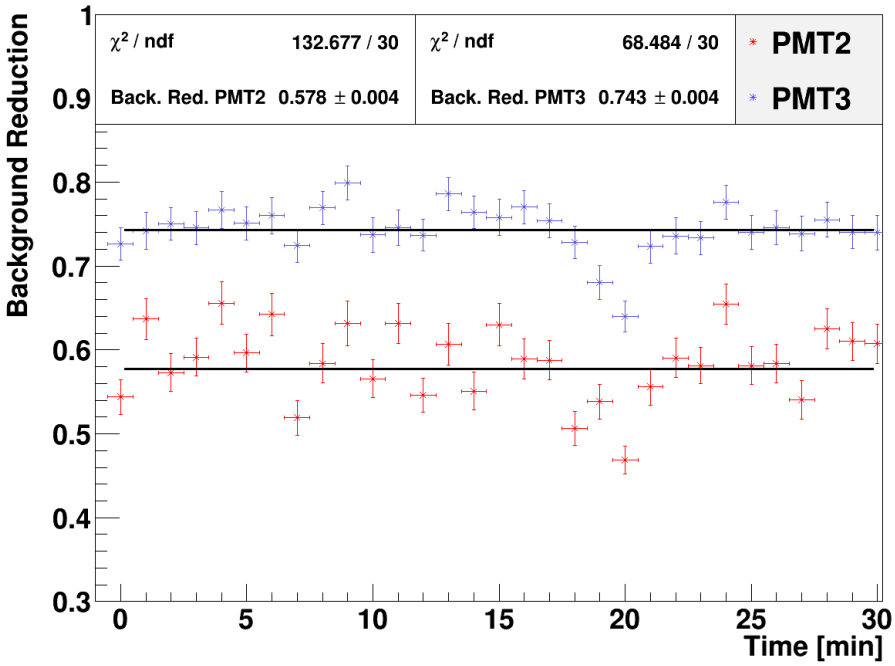

Figure 5.17: Background reduction factor through coincidence analysis.

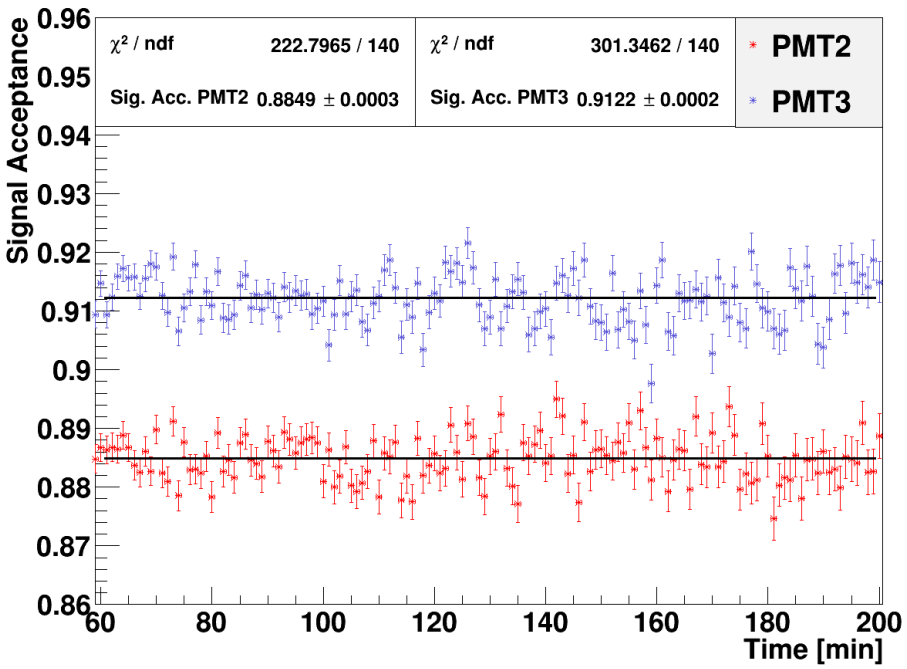

Figure 5.18: Signal acceptance of coincidence analysis measured after doping with ^{83m}Kr.

5.2.6 Background reduction by implementation of an active muon veto

One of the major backgrounds expected in the cross-detector even after applying a coincidence condition is the rate produced by cosmic ray induced secondary particles. High energetic cosmic particles (mainly protons and α particles[Oli14c]) produce particle showers when colliding with atoms in the earths atmosphere. The particle flux and its components on the sea level produced in these showers can be seen in table 5.4. Muons are of particular interest regarding the background in particle detectors because other than for neutrons or electrons, muons cannot easily be surpressed by conventional shielding.

Muons are not directly created during interaction of cosmic rays with atmospheric atoms but are the decay product of the primarily produced pions and kaons. Although free muons are with a mean lifetime of 2.197 µs[Oli14d] fairly short living particles they can reach the surface of the earth due to their relativistic velocities. At ground, muons show an overall angular intensity distribution which is approximately described by $\propto \cos^2\theta$[Oli14c]. This distribution deviates slightly for high energetic (where it becomes flatter) and low energetic (where it becomes steeper) muons. Not only do they constitute the largest component (63%) of the cosmic ray induced particle flux on sea level but are also difficult to shield from. While underground experiments like XENON1T use the shielding from hundreds of meter of rock, for an application as described in this thesis shielding is not feasible. Instead, by adding an external scintillator to the detector setup, the muon induced background can be reduced. This "veto" discriminates muon induced background by monitoring the coincidence between the X-detector and its external scintillator. As muon detector two EJ-200 plastic scintillators (from *Cosmic-Projekt* DESY in collaboration with *Hamamatsu*® and *iseg*®, see fig. 5.19) with a detection volume of $V_{\mu_{det}} = (20\text{x}20\text{x}1.25)\,\text{cm}^3$ were used.

Initially the detection efficiencies of the muon detectors were determined. This was done by stacking three detectors and measuring their coincidence rate in horizontal orientation. In this setup the outer two detectors constitute the reference while the middle detector is examined. I.e. by determining the ratio of the coincidence rate $r_{\mu_1-\mu_3}$ to $r_{\mu_1-\mu_2-\mu_3}$ the detection efficiency of detector μ_2 can be determined. This measurement was done three times with alternating detector positions in order to examine all three available muon detectors (see table 5.5). It was found that detector μ_2 showed a high detection efficiency of 98.7% while the efficiency of scintillator μ_1 and μ_3 were lower at 83.3% and 86.2% respectively (the measurement can be found in appendix B figure B.1-B.3). For the active muon veto the scintillators μ_2 and μ_3 were used.

Table 5.4: Percentage of radiative components from cosmic ray induced particle flux on sea-level[Bog06].

Total flux	Muons	Secondary neutrons	Electrons	Protons, pions
$3{\cdot}10^{-2}\text{cm}^{-2}\text{s}^{-1}$	63%	21%	15%	<1%

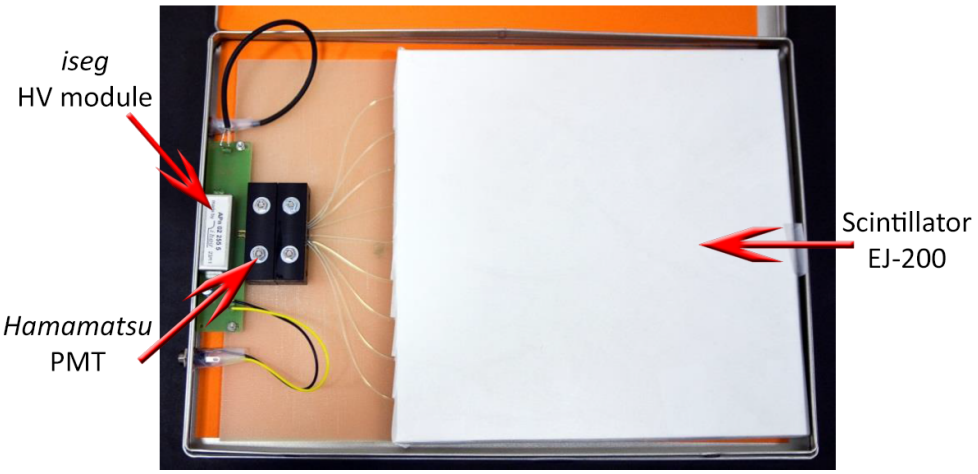

Figure 5.19: Inner view of the detector box from DESY. On the right the plastic scintillator is visible. Optical fibers connect it to the PMT from *Hamamatsu*® on the mid-left which is connected to the high-voltage module from *iseg*[Desy13].

The measurements additionally allowed to make a statement about the effective vertical radiative particle flux $\Phi_{\mu,IKP}$ as present in the laboratoy in the IKP Münster. With the dataset taken with the scintillators μ_2 and μ_3 in coincidence a flux of

$$\Phi_{\mu,IKP} = \frac{r_{\mu_2-\mu_3}}{A_{\mu-det} \cdot \epsilon_{\mu_2}, \cdot \epsilon_{\mu_3}} = 1.24(1) \cdot 10^{-2} \mathrm{cm}^{-2} \mathrm{s}^{-1} \tag{5.2.10}$$

The measured flux $\Phi_{\mu,IKP}$ is slightly lower than the literature value for the intensity of cosmic muons ($1.89\,\mathrm{cm}^{-2}\mathrm{s}^{-1}$ as taken from table 5.4) but agrees roughly considering that due to the non-negligable effective distance between the scintillators ($d = 2\,\mathrm{cm}$) particles with higher incidince angles will be less likely detected in coincidence.

Finally a 30 min background measurement was performed including the coincidence analysis of the X-detector as well as the active muon veto. The muon detectors were installed sideways to the detection volume of the X-detector (see figure 5.20). Due to the position of the X-detector within the gas system and guidance of the pipes the top/bottom positioning of the

Table 5.5: Efficiency measurement of the muon detectors.

	Detector stacking $\mu_2 - \mu_1 - \mu_3$	Detector stacking $\mu_1 - \mu_2 - \mu_3$	Detector stacking $\mu_2 - \mu_3 - \mu_1$
Coincidence rate r_{i-k} of two outer reference detectors [Hz]	4.20(7)	3.50(5)	4.19(9)
Coincidence rate r_{i-j-k} of three detectors [Hz]	3.48(8)	3.57(5)	3.62(8)
Detection efficiency ϵ_j of middle detector	0.833(6)	0.987(3)	0.862(6)

muon-veto, which is preferable due to the angular intensity distribution $\propto \cos^2\theta$, could not be realized without a rebuilding of the system. However, for testing the muon veto even in vertical position the detectors cover a sufficiently sphere due to their large size in relation to the X-detector. The coincidence algorithm was adjusted to a logical circuit where an event was discriminated as external background whenever a coincidence signal was measured in the X-detector simultaneously with at least one of the muon detectors. The result can be seen in figure 5.21 where the background rate of the single PMTs measured as well as the reduced background through coincidence analysis and active muon veto is plotted. Although the muon veto did reduce the background rate further on to $B_{X,\mu_{veto}} = 0.89(2)\,\mathrm{Hz}$, this reduction was relatively small with a muon veto rate of

$$r_{\mu_{veto}} = 0.187(3)\,\mathrm{Hz}.$$

In order to check if the remaining background was caused by an inefficient veto or was in fact caused by a different effect, a Monte Carlo simulation of the muon veto was performed which will be described in the following section.

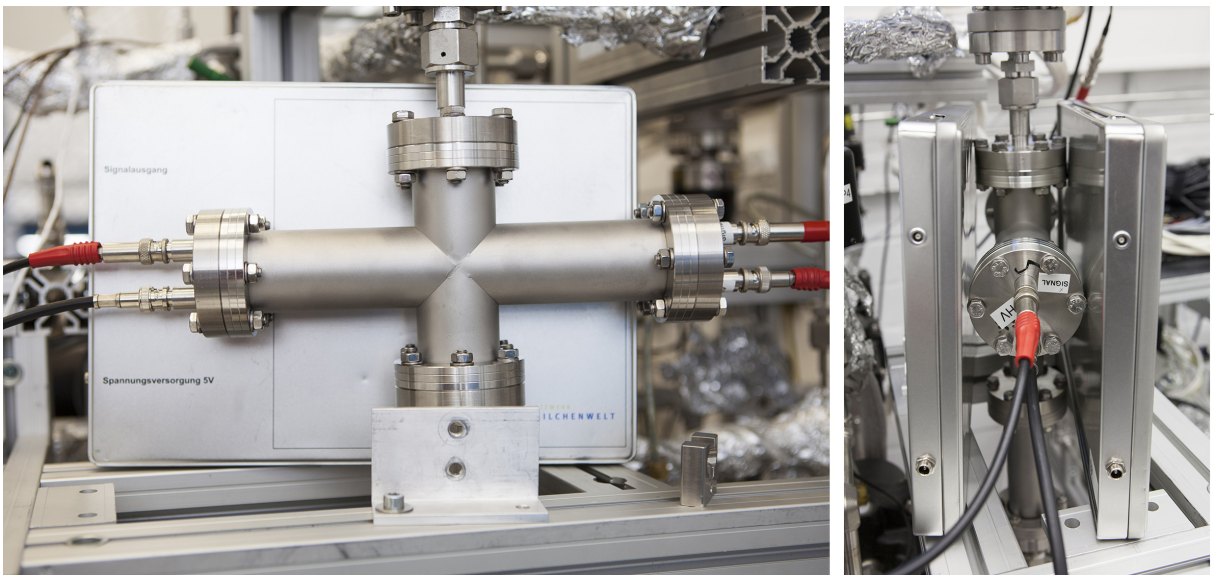

Figure 5.20: *Left:* Picture of the cross-detector in front of the muon-veto box placed around the central detection volume. *Right:* Side view of the finally installed two muon-veto boxes surrounding the cross-detector.

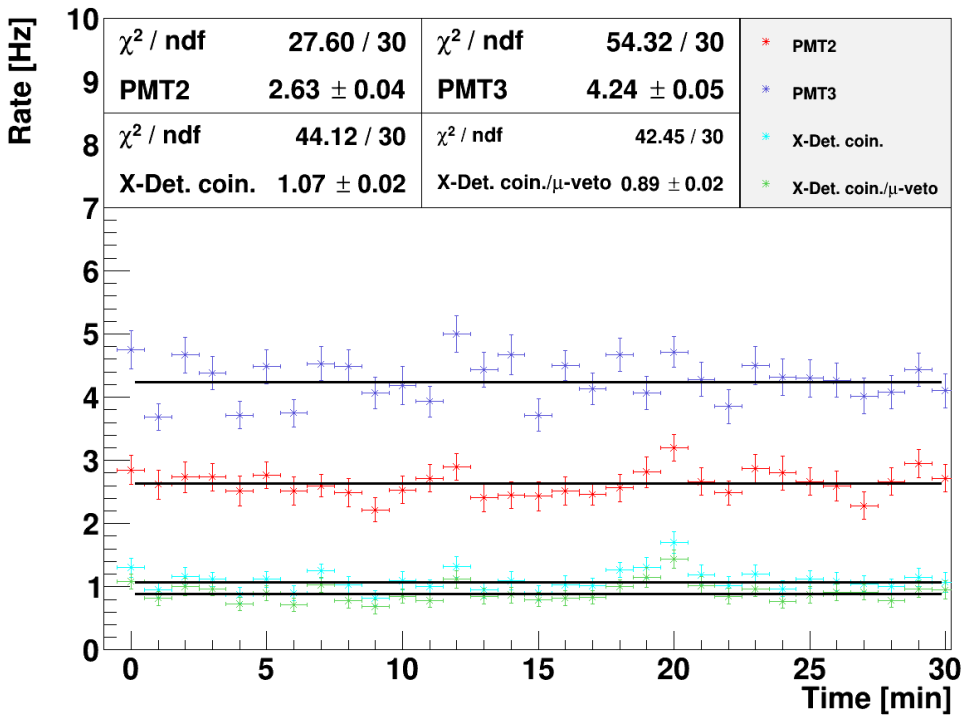

Figure 5.21: Background rate of X-detector in "single"-mode, coincidence mode and with active muon veto.

5.2.7 Monte Carlo simulation of the expected muon flux in the detector setup

In order to examine if the observed muon veto rate was the maximal reduction achievable, considering the detection efficiencies of the scintillators and the assembly of the setup, a C++ based Monte Carlo simulation in ROOT was developed (the code can be found in appendix C). It is based on generating random particle distributions according to their angular intensity distributions $\propto \cos(\theta)^2$ and tracking them along their direction of motion with a step size of 1 mm.

During each step, their position is compared to the defined geometry of the detector setup to see what proportion of the generated particles actually pass the detector as well as the muon veto. The X-detector geometry was approximated to be an ideal sphere with the given inner volume $V_X = 37.2\,\mathrm{cm}^3$ ($\hat{=} R_X = 20.71\,\mathrm{mm}$). The center of the coordinate system was then placed in the center of the sphere. This allowed for a tracking in spherical coordinates and a detection condition for the cross-detector which was simply described by "$if(\sqrt{x_\mu^2 + y_\mu^2 + z_\mu^2} < R_X)$". For the muon detectors the condition was done in Cartesian Coordinates due to their simple rectangle geometry.

The in ROOT implicated random function generator *TRandom3* was used to generate a random starting polar angle θ $[-\frac{\pi}{2}, \frac{\pi}{2}]$ according to $\cos(\theta)^2$ and a random uniform azimuth angle ϕ $[0, \frac{\pi}{2}]$. The starting point (x_0,y_0,z_0) was uniformly generated on a x-y plane with a surface

$A_{plane} = (2000\text{x}2000)\text{mm}^2$ at $z_0 = 100\,\text{mm}$, which is given by the top end of the muon detectors. The plane was chosen as large as possible without creating a too high demand of computing time. While in theory this plane should be much larger to cover all angles of the muons, due to their angular distribution the majority of particles penetrating the detector will be coming from a surface closely above the center of the detector. An even larger surface plane was tested but did not show any significant difference in the simulated rates.
Finally, from the number of generated particles N_{sample} starting on a plane with the surface A_{plane} and the number of simulated detections in both X-detector and muon detector $N_{X,\mu}$, the expected veto rate $r_{\mu_{veto}}$ caused by external muon radiation in units of $[\text{cm}^{-2}\text{s}^{-1}]$ could be calculated by

$$r_{\mu_{veto}} = \Phi_{cosmic} \cdot p_\mu \cdot A_{plane} \frac{N_{X,\mu}}{N_{sample}} \tag{5.2.11}$$

where Φ_{cosmic} is the flux of cosmic ray induced secondary particles and p_μ the percentage of muons (taken from table 5.4). For $N_{X,\mu}$ the determined detection efficiency of the muon detectors p_{μ_1}, p_{μ_2} was accounted for by

$$N_{X,\mu} = N_{X,\mu_1} \cdot p_{\mu_1} + N_{X,\mu_2} \cdot p_{\mu_2} - N_{X,\mu_{1,2}} \cdot p_{\mu_1} \cdot p_{\mu_2} \tag{5.2.12}$$

where double counts are eliminated by the last term. In order to give an upper limit, the unknown detection efficiency of the X-detector was assumed to be 100% regarding external background. The simulation was performed for a total of $5 \cdot 10^7$ particles and gives the simulated rate of

$$r_{\mu_{veto},\text{sim}} = 0.13(1)\text{Hz}$$

as well as the upper limit of the expected muon induced background in the X-detector

$$r_{\text{X}_\text{B},\text{sim}} = 0.33(1)\text{Hz},$$

where the uncertainty is the standard deviation from 50 single runs. The simulated muon veto rate $r_{\mu_{veto},sim}$ is 30 % smaller than the measured veto rate $r_{\mu_{veto}} = 0.187(3)\,\text{Hz}$. Since the muon background measurement in chapter 5.2.6 was consistent with the literature value, a higher muon flux cannot be expected. Furthermore, since the simulation was designed to give an upper limit on the expected rate, its modification can only lead to an even smaller expected rate. Possible reasons for this divergance will be discussed in in the following section.
Based on the simulated results, one can state the sideways positioning of the muon detectors only effectively shields $\sim 47\%$ of the muon induced background, where their limited detection efficiency has taken into account. Secondly it reveals that the background of the cross-detector after coincidence analysis can not be caused solely by cosmic ray induced radiation. Given the value determined in chapter 5.2.5 ($B_{X,coin} = 1.07(2)\,\text{Hz}$) even with a perfect veto, a background rate $B_{X,\mu_{veto}} \lesssim 0.74\,\text{Hz}$ can not expected to be achieved. In order to be nonetheless able to reduce the background even more, a more detailed analysis of the induced signal was performed, described in the following section.

5.2.8 Signal analysis of coincidence events

Another possibility of discriminating coincidence background events is by analysing their energy deposition inside the detector. Since ^{83m}Kr decays with a defined energy of in total 41.55 keV, it should be distinguishable from background events, in particular those which have been caused by high energetic particles. E.g. the rate of energy loss of cosmic muons, which is described by the Bethe-Bloch formula, is nearly constant with $-\frac{dE}{dx} \sim (1.5-2)\,\frac{\mathrm{MeV\cdot cm^2}}{\mathrm{g}}$ for GXe due to their characteristic as MIPs (minimum ionizing particles) at their mean energy of 4 GeV at sea level [Oli14c]. In a spherical detector with $d \approx 4\,\mathrm{cm}$ at $p = 2\,\mathrm{bar}$ muons can deposit around

$$\Delta E = -dE/dx \cdot \rho d \approx 80\,\mathrm{keV}, \tag{5.2.13}$$

for GXe with the specific surface density $\rho d = 0.045\,\mathrm{g/cm^2}$. In order to use this effect for background discrimination, every event that triggered in coincidence was analysed in a window of $\pm\,40$ ns around the peak. The integrated signal height of $2.4{\cdot}10^5$ decay events of ^{83m}Kr plotted with the integrated signal height of equal amount of muon-vetoed background coincidence events can be seen in figure 5.22. The energy spectrum of the background measurement S_B shows a significantly broader tail of the Landau-like distribution towards regions of higher energies. Hence, by applying a high energy cut, where only events with less signal height are considered, the background can be further on decreased while only loosing small amounts of signal rate. In order to see the effect of background reduction R_B and ^{83m}Kr signal acceptance A_S at different energy cuts E_{cut}, the ratio of the energy cut-depending integral of the background and signal

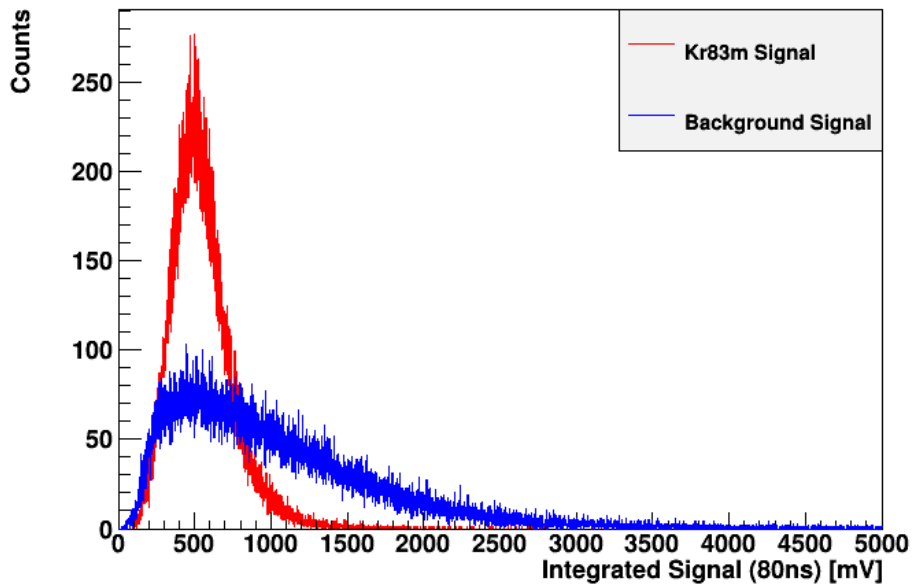

Figure 5.22: Signal height of coincidence events measured in the cross-detector during high doping with ^{83m}Kr (red) plotted next to the signal height of coincidence events measured during background measurements (blue).

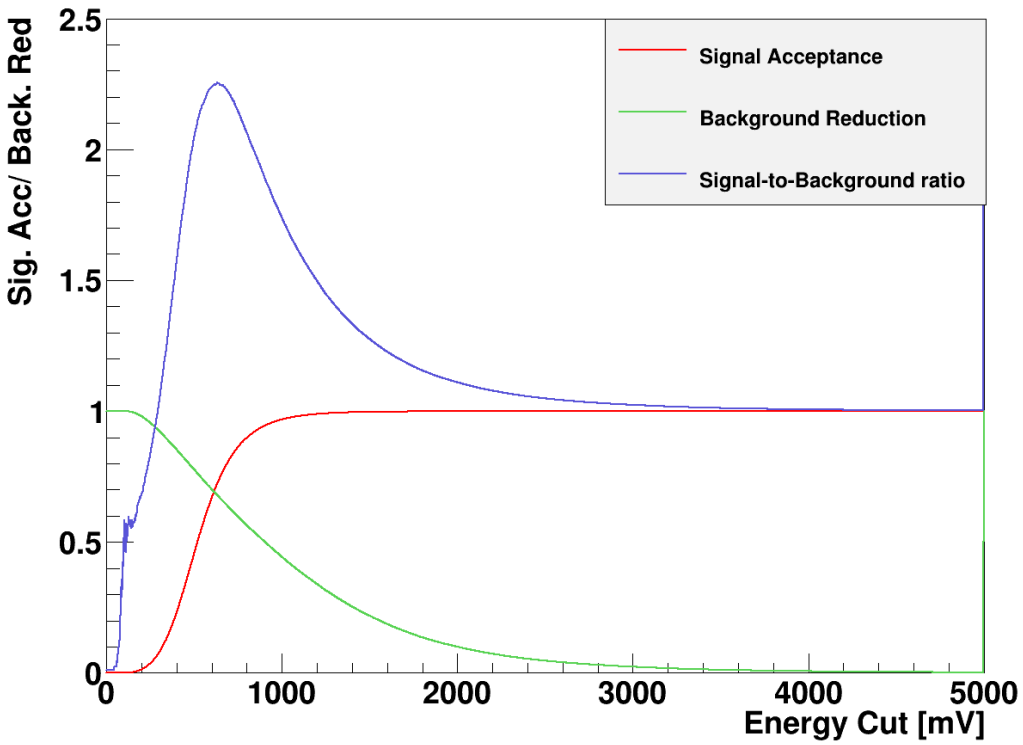

Figure 5.23: Signal acceptance (red) and background reduction (green) factor for the X-detector depending on the applied energy cut. The resulting signal-to-background ratio S/B as a function of energy cut (blue) is plotted and shows a peak at $E_{cut} = 640\,\text{mV}$.

spectrum against the total event count N_{evt}

$$R_{B,S}(E) = \frac{\int_0^{E_{cut}} S_{B,S}(E)}{N_{evt}} \tag{5.2.14}$$

was plotted in figure 5.23. Obviously signal acceptance A_S and background reduction R_B are by definition oppositely affected by the application of an energy cut. To find an optimal value for an energy cut, the signal-to-background ratio S/B was plotted on top of the two spectra. A clear peak can be seen at $E_{cut} = 640\,\text{mV}$ with $S/B \sim 2.25$. Applying the energy cut on the analysed background signals which triggered in coincidence, reduces the background rate of the X-detector furthermore to

$$B_{X,E_{cut}} = 0.30(1)\,\text{Hz}$$

(see figure 5.25) with an acceptance factor of 72.3(1) % regarding the ^{83m}Kr induced coincidence rate.

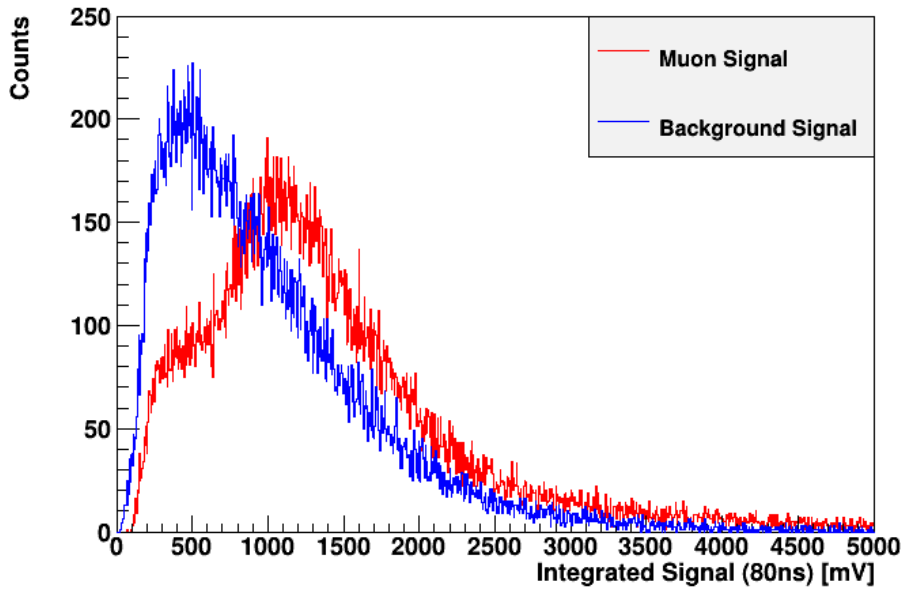

Figure 5.24: Signal height of coincidence events measured in the cross-detector during background measurements (blue) plotted next to the signal height of coincidence events discriminated by the muon veto (red).

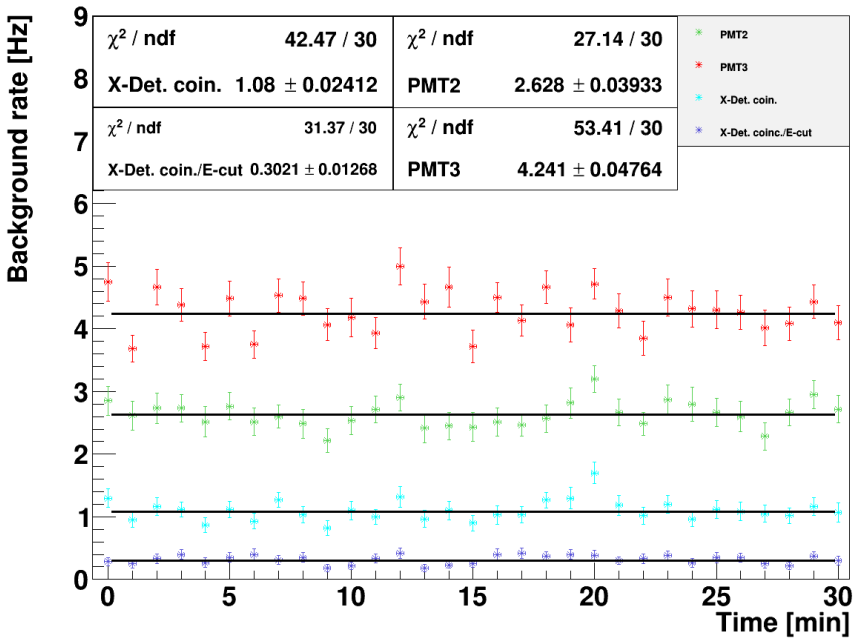

Figure 5.25: Background rate of X-detector in "single"-mode, coincidence mode and with energy cut.

5.2.9 Summary and discussion of final improvement

When combining the muon veto with the high energy cut of background events which triggered in coincidence, the background rate of the X-detector is furtheron reduced to the final background of

$$B_{X,fin} = 0.27(1)\text{Hz}.$$

By comparing this lowest achieved background of the X-detector to the initially measured backgrounds in chapter 5.2.3 of the T-detectors and including the effect of the PTFE corpus as well as the acceptance factors from the coincidence criterium and the high energy cut, one can directly state the improvement regarding the signal-to-background S/B by

$$\Delta S/B = \frac{B_{0,i}}{B_{X,fin}} \cdot \Delta\Sigma_i \cdot S_{A,coin} \cdot S_{A,E_{cut}}. \tag{5.2.15}$$

In respect to both T-detectors with *PMT2* and *PMT3* the increase is calculated to be

$$\Delta S/B_2 = 10.2(4) \qquad \Delta S/B_3 = 7.7(3).$$

Lastly, in order to examine the characteristic of the coincidence background $B_{X,coin}$, the signal analysis was additionally performed on the muon-vetoed external background events. The energy spectrum deduced from $5 \cdot 10^4$ events is plotted in figure 5.24, where it shows an even more distinctive tendency to higher energies than the coincidence background. Again, this suggests that the remaining background after application of an active muon veto $B_{X,\mu veto}$ is not solely caused by cosmic ray induced external background events. This agrees with the results from the Monte Carlo simulation in chapter 5.2.7. Especially when considering that the presented spectrum of the background also contains a muon component of $\sim 43\,\%$ (due to the limited detection efficiency of the veto), and thereby slightly increasing the spectrum in higher energies, the effective spectrum that would appear with complete discrimination of cosmic muons, is relatively low energetic in relation to the muon induced background, indicating a different source than cosmic ray induced background.
What is additionally noticeable is a low energetic component in the muon energy spectrum, with a peak in equal measure to the coincidence background spectrum $B_{X,coin}$ at $E \sim 400\,\text{mV}$. This strongly suggests that the remaining background in the cross-detector, measured in coincidence mode after application of the muon veto as well as the high energy cut, is caused by a particle like radiation which causes scintillation in the GXe of the X-detector but is insufficiently detected by the muon veto. The efficiency with which the muon veto detects this low energetic background component can be estimated in two ways. Considering the results of the simulation in chapter 5.2.7, the veto rate induced by the low energetic component divided by the background in the X-detector which is not expected to be induced by muons gives

$$\epsilon_{\text{lowE}} = \frac{r_{\mu_{veto}} - r_{\mu_{veto},\text{sim}}}{B_{X,coinc} - r_{X_B,\text{sim}}} = 7.7 \pm 3.5\,\%.$$

Furthermore, when assuming that after the high energy cut the high energetic muon component is eliminated from the background, the efficiency can be additionally estimated by

$$\epsilon_{\text{lowE}} \approx \frac{B_{X,E_{cut}} - B_{X,fin}}{B_{X,E_{cut}}} = 10 \pm 4.7\,\%.$$

The values for the detection efficiency of the muon veto regarding the unknown low energetic component agree within the uncertainties with $\mathcal{O}(10\,\%)$.
A possible and reasonable explanation of this undiscriminated background could be the exposure through gammas from the ^{83}Rb-source. Although the source is properly shielded with several layers of lead in order to reduce the external radiation under the exemption limit, the fairly small background rate could still arise from it. ^{83}Rb (as presented in figure 5.1) decays to ^{83}Kr solely by electron capture while emitting γ or X-rays of various energies. However with a majority of 89.98 % ^{83}Rb decays by emitting a γ with an energy of 520.40 keV/529.59 keV/552.55 keV[NDC15]. Gammas at $\sim$540 keV have an attenuation coefficient of $\mu/\rho \sim 0.14\,\text{cm}^2/\text{g}$ for lead[Hub95]. With the density of lead $\rho = 11.34\,\text{g/cm}^3$ the mass attenuation length μ can be determined which determines the loss of intensity depending on the thickness of an absorber

$$I(x) = I_0 \cdot e^{-\mu \cdot x}. \tag{5.2.16}$$

With a shielding thickness assumed to be $x \sim 5\,\text{cm}$ the transmission factor of lead for 540 keV gammas is 0.0272 %. With the distance between the ^{83}Rb and the X-detector $d = 1.1\,\text{m}$ and the areal cross section of the X-detector $A_X = \pi \cdot r_X = 13\,\text{cm}^2$ the amount of gamma exposion in the X-detector can be determined

$$r_\gamma = A_0(^{83}\text{Rb}) \cdot \frac{A_X}{4\pi d^2} \cdot e^{-\mu x} = 0.244\,\text{Hz}.$$

This value can only be taken as rough estimate, since the material gammas traverse through between source and detector was not included and the exact thickness of the lead shielding was not known. When for example assuming a shielding thickness of $x = 4\,\text{cm}$ the induced rate increases to 1.19 Hz. Hence this approximation agrees with the simulated muon vetoed background

$$B_\gamma = B_{X,coin} - B_{\mu_{veto},\text{sim}} = 0.74\,\text{Hz}$$

in the order of magnitude. Furthermore, these gammas are expected to cause low energy signals, due to the energy loss in the shielding. Since this source of background was initially not considered, the muon veto detectors were not positioned in the beam path in order to allow discrimination of these gammas which therefore could explain the undiscriminated background.

5.3 Building and testing of a ^{83m}Kr emanator for a low energy calibration of XENON100

The monoenergetic conversion electrons emitted by the decaying ^{83m}Kr make it especially interesting for low energy calibration applications. Since with an increasing size the XENON detectors self-shielding further on improves, a calibration of the detector response to low energy recoil with external calibration sources gets more challenging. While external low energy sources fail to penetrate the detector sufficiently for a calibration of the inner volume, internal calibration sources obviously do not suffer from this problematic.

With a simple ^{83}Rb source port connection to the gas system, where ^{83m}Kr was introduced by diffusion, the reproducibility and predictability of the amount of introduced ^{83m}Kr particles was challenging and the potential of the source for tracer emanation was not completely taken advantage of. While the latter was a rather minor issue for the use in the Münster laboratory due to the strong ^{83}Rb source with an activity of several MBq, for a potential usage in the underground laboratory at LNGS this states a severe problem. For safety reasons the import regulations for radioactive sources at LNGS are very strict, making an effective use of the allowed activity (typically $\sim 10\,$kBq) necessary.

In order to increase the doping efficiency of the ^{83}Rb source the underlying idea was to incorporate the source into the gas circulation loop in a bypassable way rather than just in a bypassed port. By guiding the gas flow through the source its full doping potential can be principally utilized. Besides the above considered and still valid requirement of ^{83}Rb purity outside the source, this additionally necessitates the support of a certain gas flow through the emanator without creating a significant pressure gradient, which depends in detail on the application. Since during the development of the ^{83m}Kr emanator a calibration of the XENON100 detector with ^{83m}Kr was decided, it needed to fulfill the operating requirements of XENON100. The emanator needed to support a flow of 8 slpm at 2 bar inlet pressure where no differential pressure higher than 200 mbar was allowed. This was limited by the at the experiment installed membrane pump from KNF. Finally the designated position for the ^{83m}Kr calibration source constrained the dimensions of the emanator to be smaller than 450x400 mm^2.

In order to support the flow of 8 slpm the originally used PTFE filters had to be replaced. The manufacturer quoted a supported gas flow of 5 slpm/cm^2 regarding the filters with a pore size of 220 nm[Mil01]. Due to the fact that the filter size and a holding structure for the stainless steel tubes limited the cross section to $\lesssim 1\,$cm^2, the required flow was not expected to be supported. Dedicated measurements confirmed this and showed that at 8 slpm a differential pressure of $\sim$1 bar built up (shown in appandix D.1).

Thus for shielding the ^{83}Rb source in the ^{83m}Kr emanator, Swagelok® SS-4FW-VCR-2 filters were selected. These pleated stainless steel filters with a 2 μm pore size are internally welded to the housing to prevent any bypass flow (see figure 5.26) while only creating a slight differential pressure at even high flow rates (340 mbar at 150 slpm[Swa13]). At the moderate flow of 8 slpm no significant built up of differential pressure could be observed.

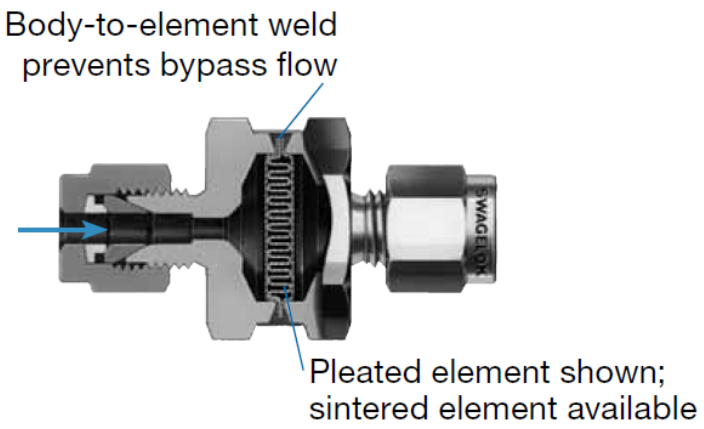

Figure 5.26: Technical drawing of the SS-4FW-VCR-2 from Swagelok®[Swa13].

The ^{83}Rb source itself was implemented in a custom made container with which issues of transport and safety were considered. A stainless steel 1/2" VCR gland was partially threaded. Additionally a metal grid was welded on two compatible holed threaded rods by laser beam welding, in order to avoid any radon contamination from common welding with thoriated tungsten electrodes (see figure 5.27). Mounted together this creates a penetrable container variable in size. The latter allows to fixate the ^{83}Rb pellets inside the container and thereby reduce the risk of a breaking of the zeolite pellets into smaller subparticles during transport. Furthermore this enables a non-destructive refilling of the source for later applications in case the source has decayed to a too low activity.

Finally for flexibility of the emanator as calibration source, a vacuum port was included in order to evacuate the segments exposed to air during transport. The final design and a picture of the emanator as it was installed in the gas system in the IKP Münster can be seen in figure 5.28. The ^{83}Rb container is covered by 2 layers of lead shielding to prevent radioactive exposure outside the emanator.

In order to verify the effective confinement of ^{83}Rb inside the emanator, an extensive screening

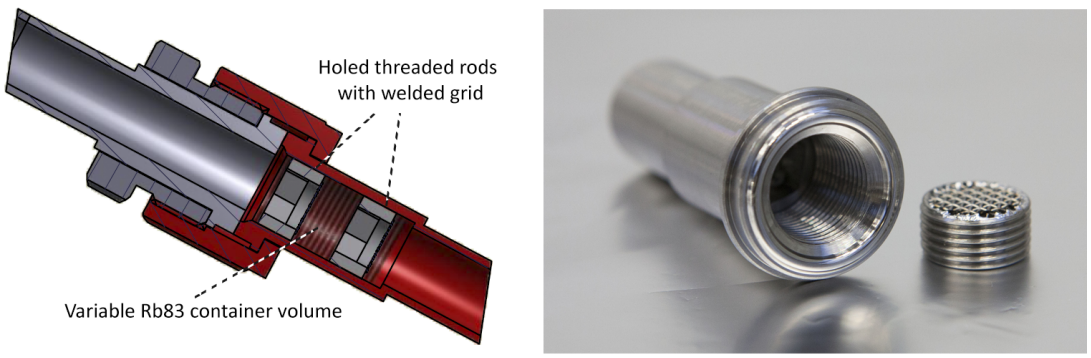

Figure 5.27: *Left:* Technical drawing of the ^{83}Rb container. *Right:* Inside view of the ^{83}Rb emanator. On the right one of the holed threaded rods can be seen.

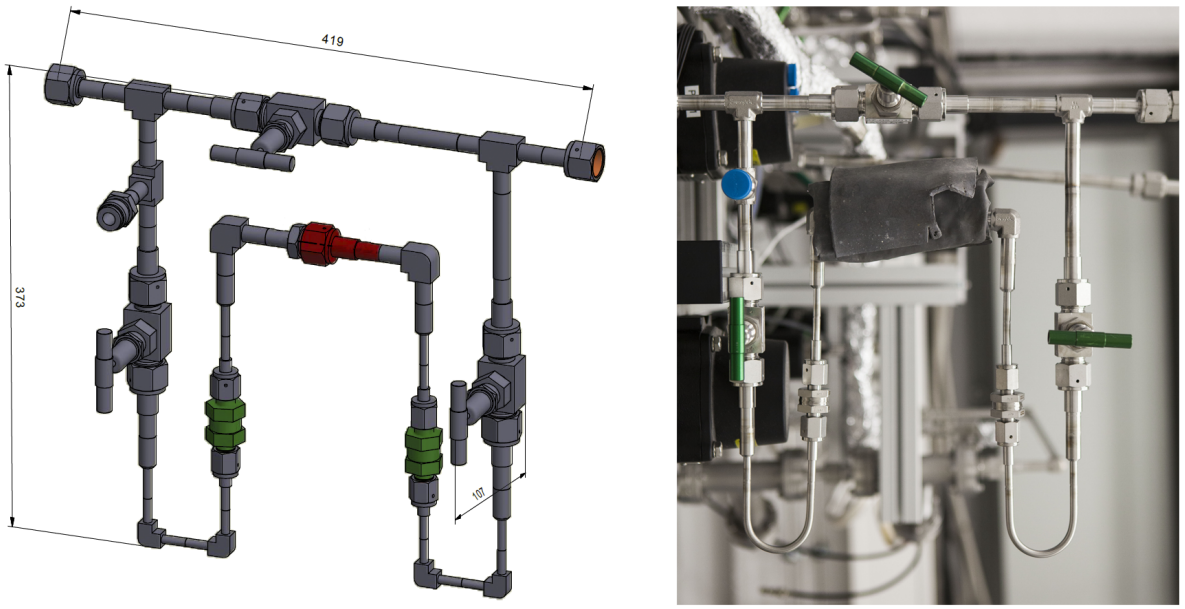

Figure 5.28: *Left:* Technical drawing of the ^{83m}Kr emanator. The filters are colored green while the housing for the ^{83}Rb pellets is marked in red. *Right:* Picture of the ^{83m}Kr emanator installed in the gas system of the Münster laboratory. The ^{83}Rb container is covered by lead shielding.

was performed. Therefore, the above mentioned PTFE filter with 200 nm pore size was installed at the output of the emanator. Then driven by the circulation pump from *QDrive*® implemented in the gas routing system, GXe was continuously circulated through the emanator at 4.4 slpm for 88 h. In case the direct flow would wear away microparticles from the zeolite pellets which would not be filtered by the 2 μm pore sized Swagelok filter, they would eventually accumulate at the PTFE filter, which was already approved for its confinement of the ^{83}Rb pellets. . Screening the PTFE filter for the characteristic energies of the gammas emitted by the decay of ^{83}Rb (see 5.2.8) would reveal a possible release of ^{83}Rb into the gas system.

Therefore, after the circulation phase the exposed PTFE filter was screened with a cryo-cooled germanium detector from Canberra® (model GX3019) at the IKP Münster. The semiconductor detector was integrated in a setup where an ADC from CAEN® digitized the voltage from the detector which could be further on processed with the software *Maestro-32* on a dedicated laboratory PC. The energy scale was first calibrated with a ^{22}Na source which disintegrates to ^{22}Ne by β-decay[Gal09]. By utilizing the known predominant γ lines at 511 keV (from annihilation of the emitted β^+) and 1247.437 keV (deexcitation of the excited ^{22}Ne*) a conversion from channel numbers given by the ADC board into an energy scale was possible.

The potentially ^{83}Rb exposed PTFE filter was analysed for 81397 s live time (shown in appandix D.3), where *Maestro-32* already considered the dead-time of the detector system. Finally a reference measurement with 90414 s live time was performed with an unexposed PTFE filter. The count rate was normalized regarding its live time and substracted from the spectrum of the exposed filter. The result can be seen in figure 5.29 where the region of interest between

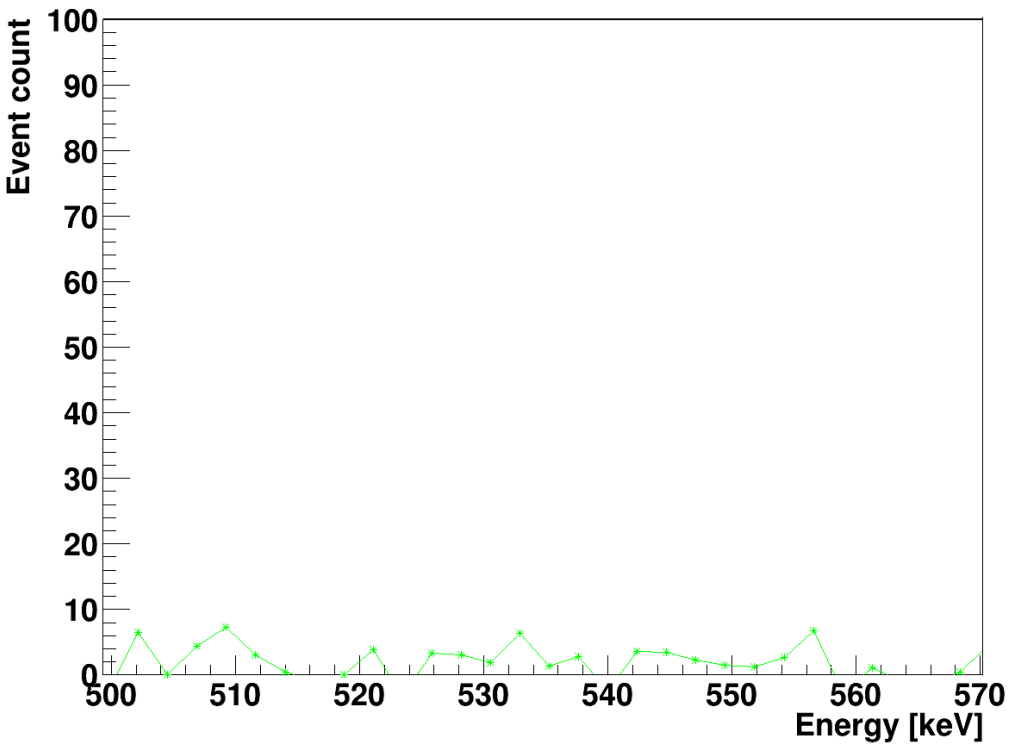

Figure 5.29: 81397 s live time γ spectroscopy measurement of exposed PTFE filter after background substraction. The background was measured with a non exposed PTFE filter for an accurate reference.

500 keV - 570 keV was selected. No traces of ^{83}Rb could be found on the PTFE filter, indicating an effective confinement of the ^{83}Rb pellets within the emanator.
The emanator was consequently approved for its application at XENON100 as ^{83m}Kr calibration source. The measurements of the introduced rate with the XENON100 detector after opening the emanator can be seen in figure 5.30. It shows an increase in measured rate up to a constant level after the emanator is opened in "diffusion mode". In this mode GXe was circulated through the bypass valve with only one source valve opened. It was not used in a flow-through mode because initial measurements showed that the emanator, although having only a small activity, introduced in fact more ^{83m}Kr into the system than the DAQ could process without getting oversaturated. This confirms the good performance of the emanator, both in its confinement of ^{83}Rb as well as its emanation rate regarding ^{83m}Kr and allows for a long time use as calibration source, since by the use of the flow-through mode the emanation rate can be additionally increased.

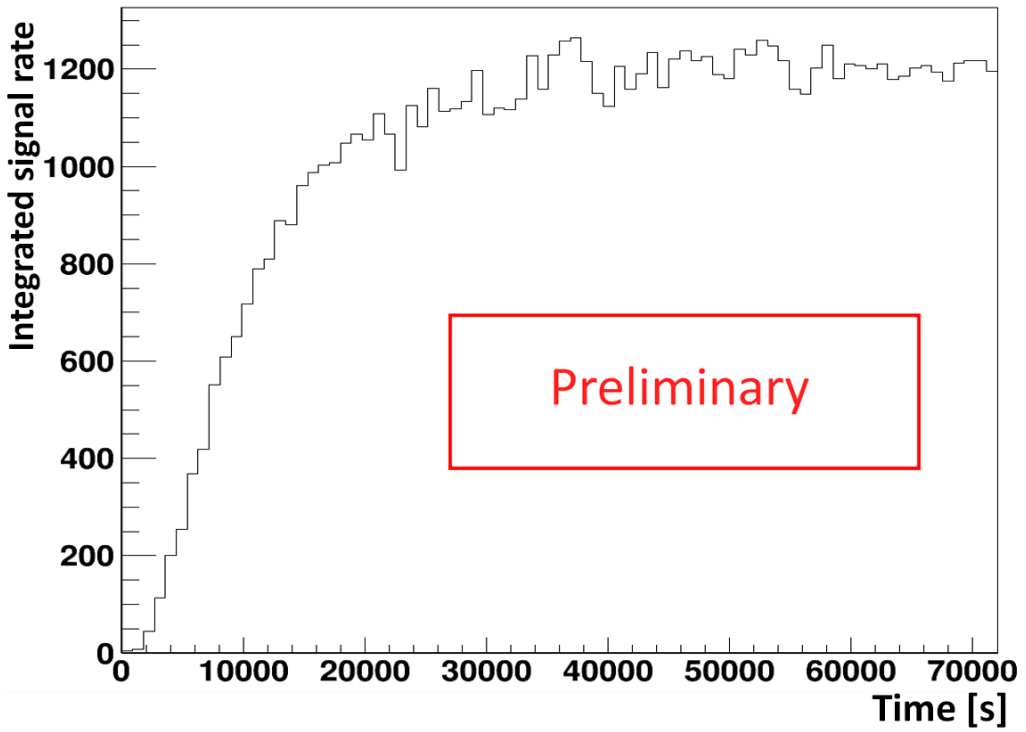

Figure 5.30: Prelimanary result of the ^{83m}Kr calibration run with the custom built ^{83m}Kr emanator at XENON100 in a bypass mode. The signal rate are given in an integrated form over each bin, which corresponds to 15 min. The plot was created by A. Fieguth in courtesy of the XENON collaboration.

Chapter 6

Summary

The experimental detection of dark matter in form of Weakly Interacting Massive Particles (WIMPs) could give answer to a fundamental question of cosmology. Several observations giving compelling evidence for the existence of an unknown non-bayronic form of matter were presented and theoretically motivated candidates which could explain the vast amount of missing mass were introduced and described in chapter 2.

As discussed in chapter 3, in the growing scientific field of dark matter detection the XENON Dark Matter Project is one of the leading experiments. By utilizing a dual-phase time projection chamber where liquid and gaseous xenon acts as detection medium, the international collaboration was already able to set a limit on the spin-independent cross section of $2 \times 10^{-45}\,\mathrm{cm}^2$ for a WIMP mass of $55\,\mathrm{Gev/c}^2$ with the XENON100 detector in 2012 and thereby setting the at that time worlds most stringent limit. Currently with XENON1T the next phase of the experiment is under comissioning and will start taking data in the near future to reach an even higher sensitivity for an eventual limit of $2 \times 10^{-47}\,\mathrm{cm}^2$ for a spin-independent cross section at a $50\,\mathrm{GeV/c}^2$ WIMP mass at 90% confidence level after 2 years of measurement. The IKP Münster as one of the many institutes participating in the international XENON collaboration is especially involved in the purification of the xenon from radioactive ^{85}Kr and from electronegative impurities. Therefore two for the experiment crucial subsystems were developed and built in Münster, namely the cryogenic distillation column and the gas purification system.

For the latter a slow control system was developed within the scope of this thesis, demonstrated in chapter 4. It allowed for a monitoring and control of all instruments installed before delivery to LNGS, both with from an operator panel installed at the system as well as from a dedicated computer in expert mode. Security automatisms were included to protect damage from the sensitive instruments, in particular the moisture analyzer HALO+. A PID-controller was furthermore implemented for an automatic control of the pressure conditions around the moisture analyser. A pressure difference of 700 mbar between inlet and outlet of the HALO+ was stated as necessary working condition by the manufacturer. Tests with argon flushed through the gas system showed the successful functionality of the control loop as well as its stability and fast response (setpoint is reached in $\mathcal{O}$(s)). An evaluation of the PID circuit is recommended as soon

as final working conditions are provided.

For the characterisation of the two in Münster developed systems, a tracer method based on custom made scintillation T-detectors has been developed. In chapter 5 their functional principle and their optimization in sensitivity was evaluated. For low rate measurements these detectors were shown to be background dominated with rates of $\sim$3-4 Hz. Within the scope of this thesis a X-detector was constructed with which, through the ability of coincidence measurements, dark current induced background effects could significantly be reduced (down to $B = 1.07\,\mathrm{Hz}$) while at the same time the signal detection efficiency was increased through the implementation of a specially shaped PTFE corpus (18.4 % and 13 %). Through the additional installation of an active muon veto and the application of a high energy cut, the background could furthermore be decreased to 0.27(1) Hz showing a reduction of more than an order of magnitude in respect to the background in the initially used T-detectors. Including the acceptace factors of the respective analysis, a final increase of signal-to-background ratio of 10.2(4) and 7.7(3) could be determined.

A Monte Carlo simulation was performed in order to review the measured rates in the active muon veto. The simulation, designed to give a highest limit on the expected background rates led to the result, that the highest expected rate ($r_{\mu,sim} = 0.13\,\mathrm{Hz}$) is in fact lower than the actual measured veto rate ($r_{\mu_{veto}} = 0.187\,\mathrm{Hz}$). This led to the assumption of the existence of another external background component. A designated signal analysis agreed with this by revealing a low energetic background component in the vetoed background events. While this component could principally be caused by several sources of background, an estimation showed that the radiation from the shielded ^{83}Rb-source is a likely candidate.

Finally, a $^{83\mathrm{m}}$Kr emanator was designed and constructed in order to allow a flow-through mode for high efficiency doping. The confinement capability of the emanator regarding ^{83}Rb was evaluated with a screening using a cryocooled gamma-spectrometer where no traces of ^{83}Rb could be detected. The emanator was designed as calibration source for XENON100 where it was installed and used after approvement from LNGS. Having only a small activity of $< 10\,\mathrm{kBq}$ the emanator still introduced sufficiently enough $^{83\mathrm{m}}$Kr into the detector for a high rate calibration run. In fact in flow-through mode, the detectors DAQ was even oversaturated by the emanator, wherefore it was operated in a bypass diffusion mode. This allows for a long term usage of the emanator as calibration source since even after a significant decrease of the small ^{83}Rb activity, the emanating rate can be increased by switching the operating mode. $\underset{=}{t->\infty}$

Appendices

Appendix A

Ladder Diagram of PID circuit for pressure control for the HALO+

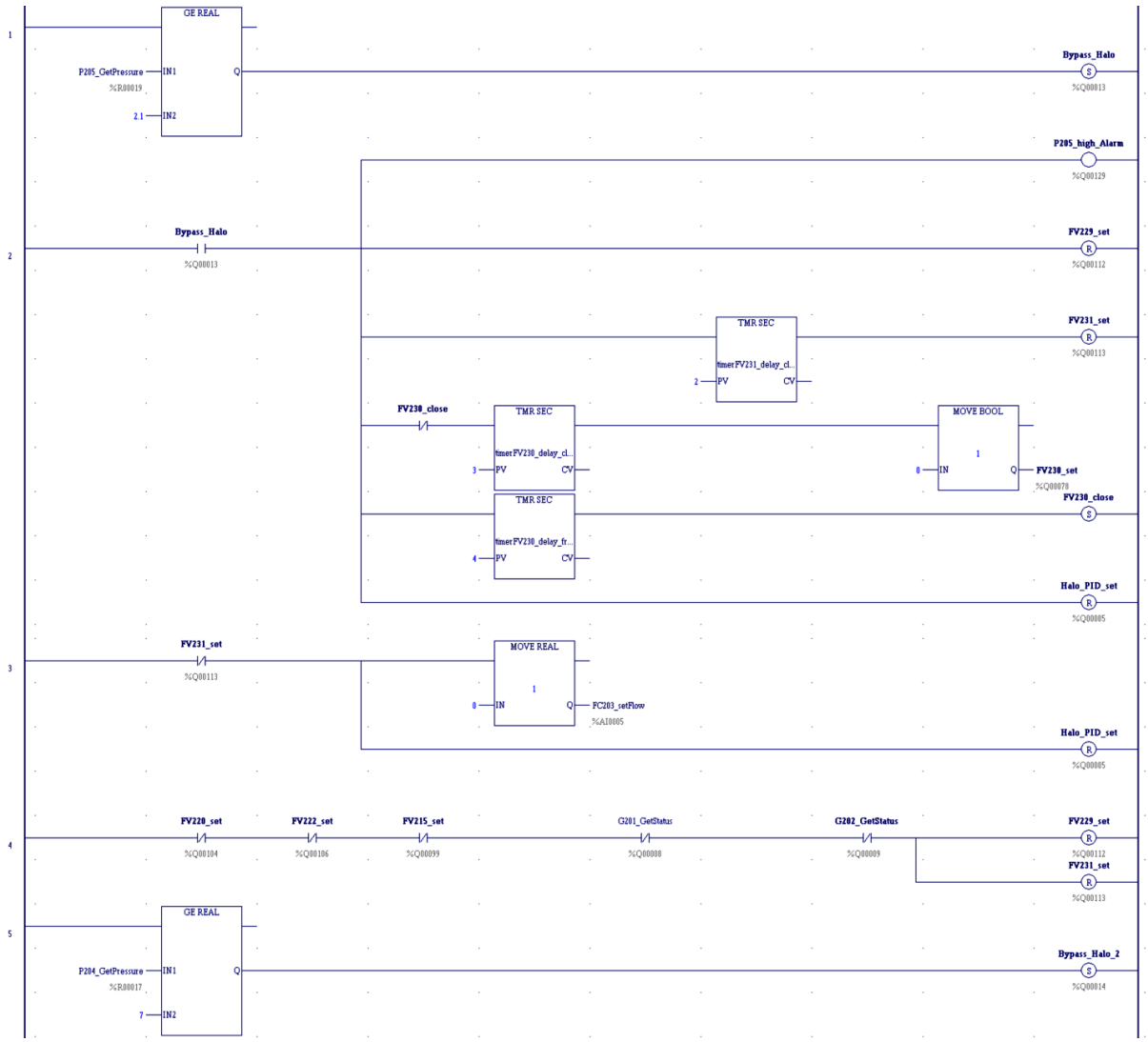

Figure A.1: PID ladder diagram of the circuit for pressure control of P205.

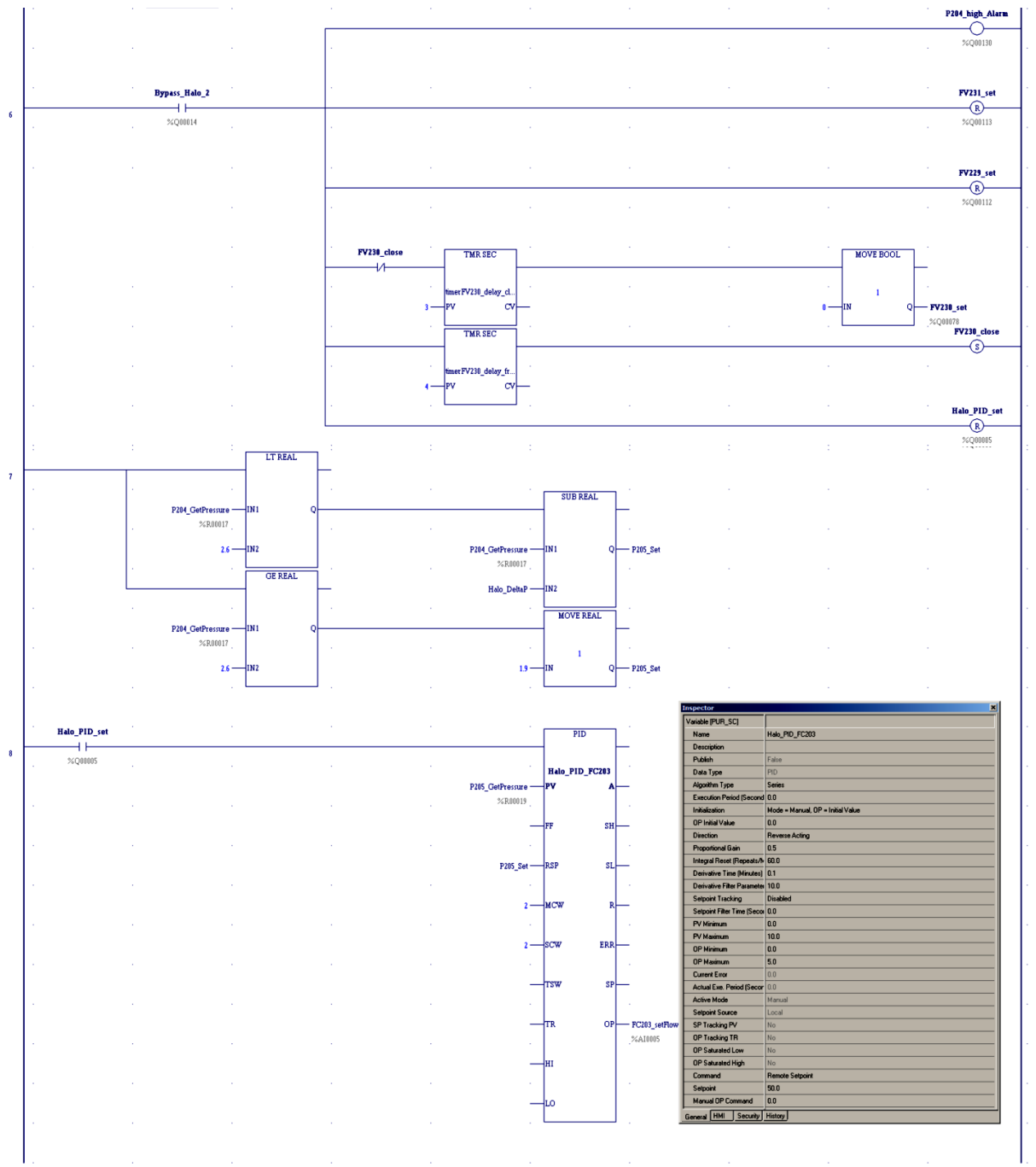

Figure A.2: Continouation of PID ladder diagram coding with opened Inspector window, showing the configuration of the PID parameters.

Appendix B

Detection efficiency of muon detectors

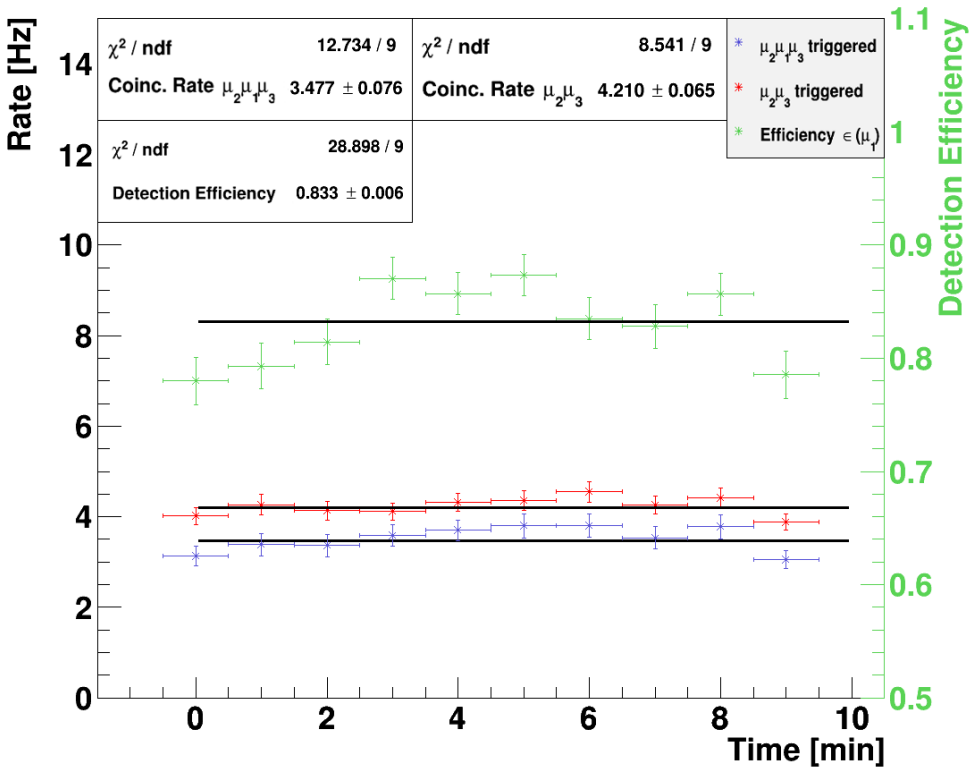

Figure B.1: Measurement of coincidence rate in stacked muon detectors for efficiency determination of muon detector μ_1. Both the coincidence rates (*black*, *left*) as well as the detection efficiency (*green*, *right*) are plotted on two different scales on the same canvas.

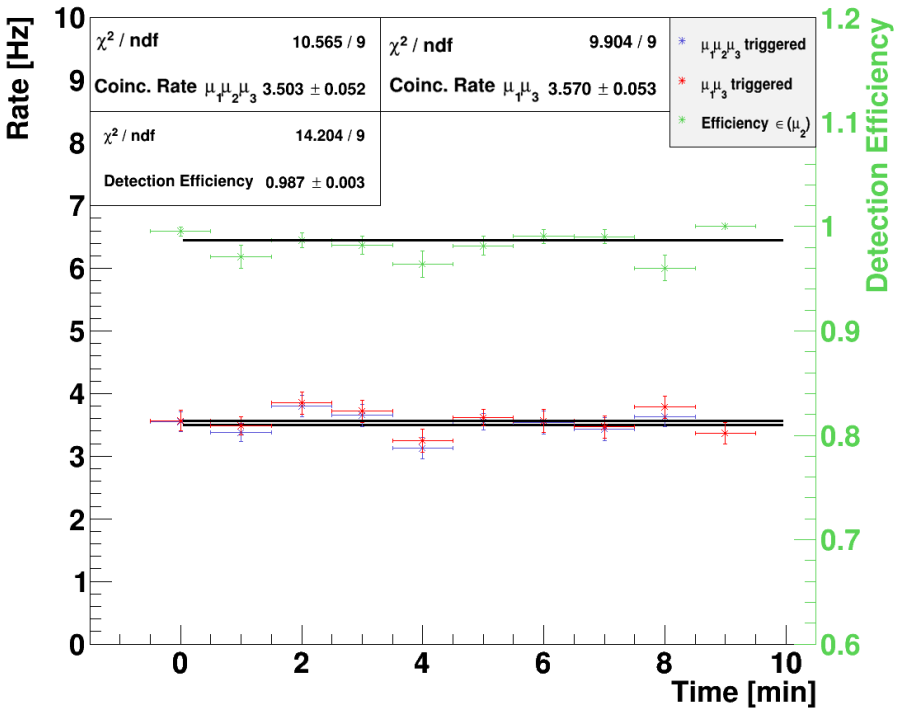

Figure B.2: Measurement of coincidence rate in stacked muon detectors for efficiency determination of muon detector μ_2. Both the coincidence rates (*black*, *left*) as well as the detection efficiency (*green*, *right*) are plotted on two different scales on the same canvas.

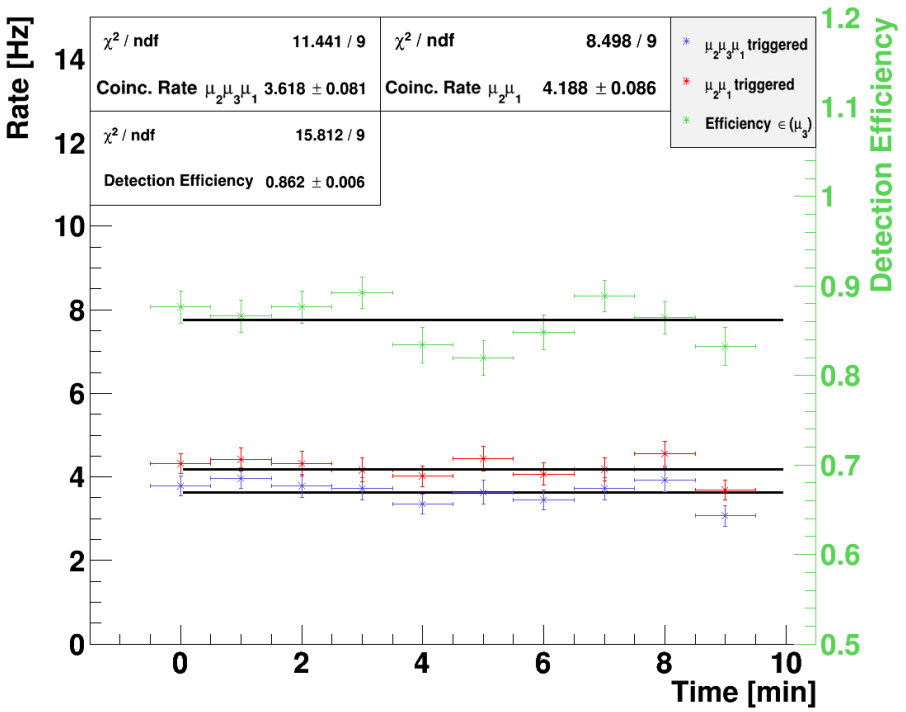

Figure B.3: Measurement of coincidence rate in stacked muon detectors for efficiency determination of muon detector μ_3. Both the coincidence rates (*black*, *left*) as well as the detection efficiency (*green*, *right*) are plotted on two different scales on the same canvas.

Appendix C

Monte Carlo simulation of muon background

```
{
#include "TFile.h"
#include "TTree.h"
#include "TRandom3.h"
#include "TF1.h"
#include "TMath.h"
#include "TApplication.h"
#include "TCanvas.h"
#include "TAxis.h"
#include "TH1.h"
#include "TVector3.h"
#include "TROOT.h"
#include <fstream>
gROOT->SetStyle("Plain");

TRandom3 *rand = new TRandom3(0);
const int Nsam=1000000;
float Colleff, Myonflux, Colleff2, Myonflux2, Ndoppel;
float x0;
float y0;
float z0;
float r;
int Ntref, steps, Paddle1, Paddle2, Ndoppel1, Ndoppel2, Ndoppel3;
ofstream ofd;
ofd.open("detsimfin32_eloss_test2mblub.dat", std::ios::app);
```

```
Ntref=0;
Ndoppel1=0;
Ndoppel2=0;
Ndoppel3=0;
 for (int i=0; i<Nsam; i++){

    TF1 *f1 = new TF1("f1","cos(x)**2",-1*TMath::Pi()/2,TMath::Pi()/2);
    double theta = f1->GetRandom();
    double phi = rand->Uniform(0,TMath::Pi()/2);
    const int xrange=1000;
    const int yrange=1000;
    x0 = rand->Uniform(-1*xrange,1*xrange);
    y0 = rand->Uniform(-1*yrange,1*yrange);
    z0 = 100;

steps=0;
Paddle1=0;
Paddle2=0;

 for(int j=0; j<2500; j++)    {

  x0+=1*sin(theta)*cos(phi);
  y0+=1*sin(theta)*sin(phi);
  z0-=1*cos(theta);
  r=sqrt(x0**2+y0**2+z0**2);

  if(r<20.71){
   steps+=1; }

if((z0>=-100) &&
    (z0<=100) &&
    (x0>=-100) &&
    (x0<=100) &&
    (y0>=45.5) &&
    (y0<=58)){
    Paddle1+=1;}

if((z0>=-100) &&
    (z0<=100) &&
    (x0>=-100) &&
```

```
    (x0<=100) &&
    (y0<=-45.5) &&
    (y0>=-58)){
    Paddle2+=1;}

                                }
 delete f1;

 if(steps!=0){
        Ntref+=1;}

 if(steps!=0 && Paddle1!=0){
        Ndoppel1+=1;}

 if(steps!=0 && Paddle2!=0){
        Ndoppel2+=1;}

 if(steps!=0 && Paddle1!=0 && Paddle2!=0){
        Ndoppel3+=1;}

 }

 delete rand;
 Ndoppel=(float)Ndoppel1*0.861+(float)Ndoppel2*0.985-(float)Ndoppel3*0.985*0.861;

 Colleff = (float)Ntref/(float)Nsam;
 Colleff2 = Ndoppel/(float)Nsam;

 Myonflux = 0.03*Colleff*(4*xrange*yrange)/100.;
 Myonflux2 = 0.03*Colleff2*(4*xrange*yrange)/100.;
 cout << "Total events in X-detector = " << Ntref << endl;
 cout << "Exected Myon flux in X-detector = "<< Myonflux << endl;
 cout << "Rate in both X-detector and Paddle = "<< Myonflux2 << endl;

 ofd << Ntref << " " << Ndoppel << " " << Myonflux <<" " << Myonflux2
<<  endl;
 ofd.close();

 return 0;
}
```

Appendix D

Filter test

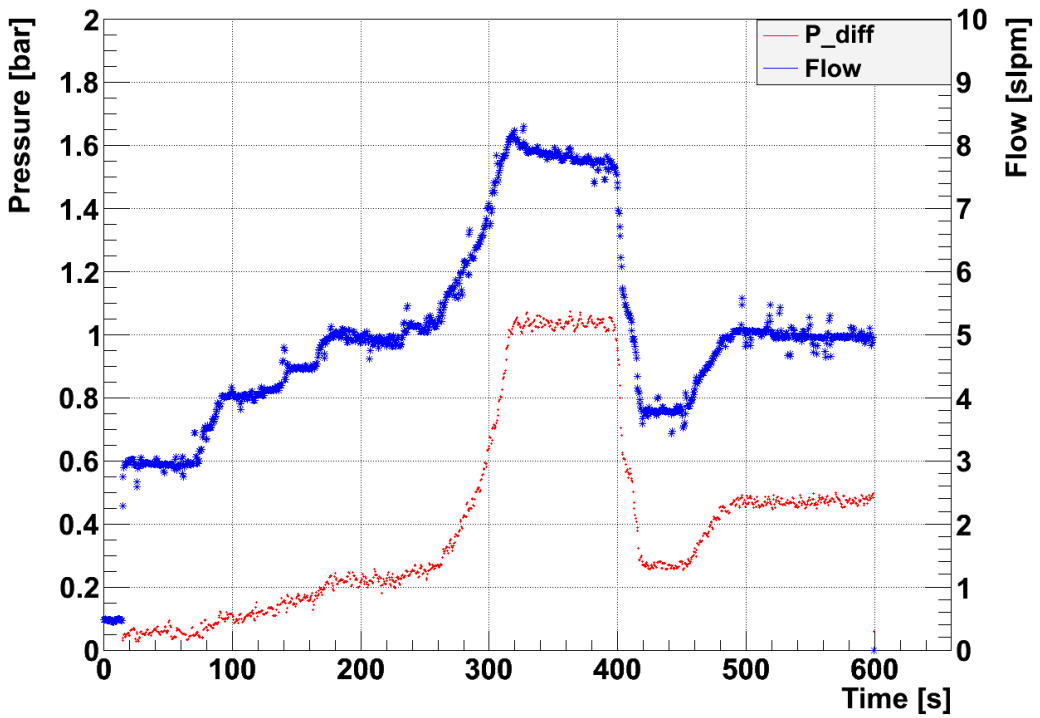

Figure D.1: Performance tests of the PTFE filter with the pump testing station in Münster. The blue line shows the achieved gas flow through the filter, the red line the appropriate differential pressure built up before and after the filter.

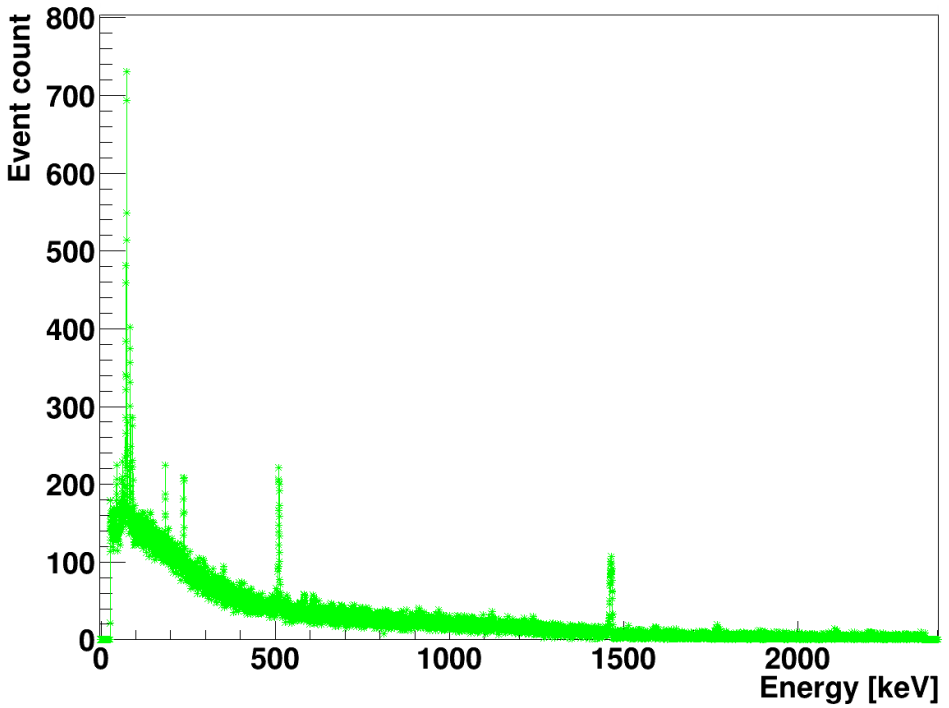

Figure D.2: 81397 s live time γ spectroscopy measurement of exposed PTFE filter.

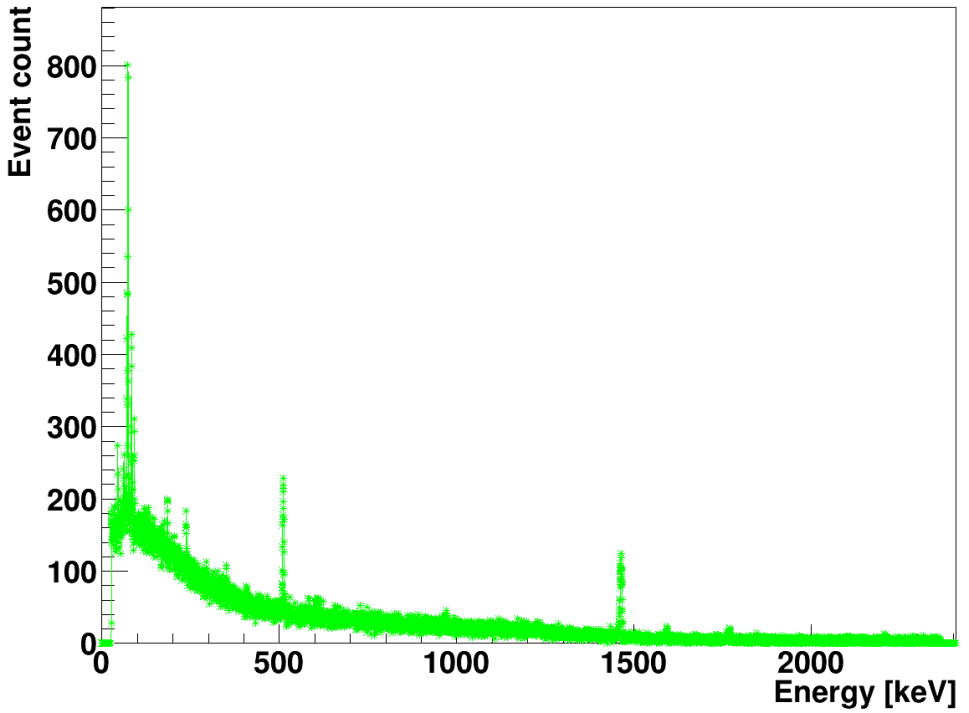

Figure D.3: 90414 s live time γ spectroscopy measurement of clean PTFE filter as reference measurement.

Bibliography

[Abe09] K. Abe et al.: *Distillation of Liquid Xenon to Remove Krypton.* Astroparticle Physics, V. 31, Issue 4, p. 290-296, 2009

[Ake14] D. S. Akerib et al.: *First results from the LUX dark matter experiment at the Sanford Underground Research Facility.* Phys. Rev. Lett. 112, 091303, 2014

[Alb14] J. B. Albert et al.: *Improved measurement of the $2\nu\beta\beta$ half-life of ^{136}Xe with the EXO-200 detector.* Phys. Rev. C 89 015502, 2014

[Agu13] M. Aguilar et al.: *First Result from the Alpha Magnetic Spectrometer on the International Space Station: Precision Measurement of the Positron Fraction in Primary Cosmic Rays of 0.5-350 GeV.* Phys. Rev. Lett. Vol. 110, 141102, 2013

[Ang08] J. Angle et al.: *First Results from the XENON10 Dark Matter Experiment at the Gran Sasso National Laboratory. Phys. Rev. Lett. 100:021303, 2008*

[Apr06] E. Aprile et al.*:* Noble Gas Detectors. *Wiley-VCH Verlag GmbH & Co. KGaA, 2006*

[Apr10] E. Aprile, T. Doke*:* Liquid Xenon Detectors for Particle Physics and Astrophysics. *Rev. Mod. Phys. 82, 2053, 2010*

[Apr11] E. Aprile et al.*:* Design and performance of the XENON10 dark matter experiment. *Astroparticle Physics 34, p. 679-698, 2011*

[Apr12a] E. Aprile et al.*:* The XENON100 dark matter experiment. *Astroparticle Physics 35, p. 573-590, 2012*

[Apr12b] E. Aprile et al.*:* Dark Matter Results from 225 Live Days of XENON100 Data. *Phys. Rev. Lett. 109:181301, 2012*

[Apr12c] E. Aprile et al.*:* Measurement of the Quantum Efficiency of Hamamatsu R8520 Photomultipliers at Liquid Xenon Temperature. *JINST 7 P10005, 2012*

[Apr13a] E. Aprile et al.*:* The XENON1T Dark Matter Search Experiment. *Springer Proc. Phys. 148, 93-96, 2013*

[Apr13b] E. Aprile et al.*:* Limits on spin-dependent WIMP-nucleon cross sections from 225 live days of XENON100 data. *Phys. Rev. Lett. 111, 021301, 2013*

[Apr14a] E. Aprile et al.*:* First Analysis of the XENON100 Dark Matter Search Data. *Astropart. Phys. V. 54, p. 11-24, 2014*

[Apr14b] E. Aprile et al.*:* First Axion Results from the XENON100 Experiment. *Phys. Rev. D 90, 062009, 2014*

[Beg91] K. G. Begemann et al.*:* Extended rotation curves of spiral galaxies - Dark haloes and modified dynamics. *MNRAS Vol. 249, p. 523-537, 1991.*

[Bel12] G. Bellini et al.*:* Cosmic-muon flux and annual modulation in Borexino at 3800 m water-equivalent depth. *JCAP, 1205:015, 2012.*

[Ber05] G. Bertone, D. Hooper, J. Silk*:* Particle Dark Matter: Evidence, Candidates and Constraints. *Phys. Rep. Vol. 405, p. 279-390, 2005*

[Ber10] G. Bertone*:* The moment of truth for WIMP Dark Matter. *Nature Vol. 468, p. 389-393, 2010*

[Bog06] L. N. Bogdanova et al.*:* Cosmic muon flux at shallow depths underground. *Phys. Atom. Nucl. V. 69, p. 1293-1298, 2006 doi:10.1134/S1063778806080047*

[Bov12] J. Bovy, S. Tremaine*:* On the local dark matter density. *Astrophysical Journal V. 756, p. 89 doi:10.1088/0004-637X/756/1/89*

[Car12] J. Cardoso, L. Levinson*:* Slow Control of Xe1T, Design and Safety Considerations *XENON Collaboration, 2012*

[Car13] J. Cardoso et al.*:* XENON1T Slow Control, Technical Design Report *XENON Collaboration, 2013*

[Cer10] D. G. Cerdeno, A. M. Green*:* Direct detection of WIMPs *arXiv:1002.1912 [astro-ph.CO]*

[Che99] C. Y. Chen et al.*:* Ultrasensitive Isotope Trace Analyses with a Magneto-Optical Trap. *Science 286(5442):1139-41, 1999*

[Clo06] D. Clowe et al.*:* A direct empirical proof of the existence of dark matter. *Astrophysical Journal 648:L109-L113, 2006*

[Desy13] Cosmic-Projekt DESY.*:* Das CosMo-Experiment, technische Bedienungsanleitung *2012*

[Dob10] A. Dobi et al.*:* Study of a zirconium getter for purification of xenon gas. *Nucl. Instr. Meth. A 620, p. 594-598, 2010*

[Dok02] T. Doke et al.*:* Absolute Scintillation Yields in Liquid Argon and Xenon for Various Particles. *J. Appl. Phys. Vol. 41, p 1538-1545, 2002*

[Eds97] J. Edsjö*:* Aspects of Neutrino Detection of Neutralino Dark Matter. *PhD Thesis, Department of Theoretical Physics, Uppsala University, 1997*

[Fen10] J. L. Feng Dark Matter Candidates from Particle Physics and Methods of Detection. *Annu. Rev. Astron. Astrophysics, 2010*

[Fes10] Festo Companys Ventilinsel MPA-L, Festo Beschreibung Pneumatik MPA-L. *Festo AG & Co. KG, Esslingen, 2010*

[Fie14] A. Fieguth*:* Investigations of impurities in xenon gas with a cold-trap-enhanced quadrupole mass spectrometer. *MSc thesis, WWU Münster, 2014*

[Fly02] S. O. Flyckt, C. Marmonier Photomultiplier tubes: principles and applications. *Philips Photonics, Brive, 2002*

[Fox11] P. J. Fox, G. D. Kribs, T. M. P. Tait*:* Interpreting dark matter direct detection independently of the local velocity and density distribution. *Phy. Rev. D 83, 034007, 2011.*

[Gal09] M. Galan*:* LNE - LNHB/CEA Table de Radionucléides. *Laboratoire National Henri Becquerel, 2009.*

[Ham06] Photomultiplier Tubes, Basics and Applications, Hamamatsu Photonics K.K. *Third Edition, 2006*

[Han11] V. Hannen et al.*:* Limits on the release of Rb isotopes from a zeolite based ^{83m}Kr calibration source for the XENON project. *arXiv:1109.4270v2, 2011.*

[Har15] Harvey et al.*:* The non-gravitational interactions of dark matter in colliding galaxy clusters. *Science Vol. 347 no. 6229 pp. 1462-1465*

[Hin95] L. D. Hinkle, J. Provost*:* Differential current thermal mass flow transducer. *US Patent 5461913, 1995.*

[Hit83] A. Hitachi et al.*:* Effect of ionization density on the time dependence of luminescence from liquid argon and xenon. *Phys. Rev. B 27, p. 5279-5285, 1983.*

[Hub95] J. H. Hubble, S. M. Seltzer*:* Tables of x-ray mass attenuation coefficients and mass energy-absorption coefficients 1 keV to 20 MeV for elements Z = 1 to 92 and 48 additional substances of dosimetric interest . *NISTIR Report 5632 (Gaithersburg, MD: NIST), 1995.*

[Jun96] G. Jungman, M. Kamionkowski, K. Griest*:* Supersymmetric dark matter. *Phys. Rep. Vol. 267, p. 195-373, 1996*

[Kuh10] Michael Kuhlen et al.*:* Dark Matter Direct Detection with Non-Maxwellian Velocity Structure. *JCAP, 1002:030, 2010.*

[Kus09] Alexander Kusenko*:* Sterile neutrinos: the dark side of the light fermions. *arXiv:0906.2968v3, 2009.*

[Lae03] J. R. De Laeter et al.*:* Atomic weights of the elements: Review 2000 (IUPAC technical report). *Pure and Applied Chemistry V. 75, No. 6, p. 683-800, 2003*

[Lev14] C. Levy-Brown*:* Light propagation and Reflection off Teflon in Liquid Xenon Detectors for the XENON100 and XENON1T Dark Matter Experiments *PhD thesis, WWU Münster, 2014*

[Lip93] B. G. Liptak*:* Flow Measurement *Taylor & Francis, 1993*

[Lin14] S. Lindemann, H. Simgen*:* Krypton assay in xenon at the ppq level using a gas chromatographic system and mass spectrometer *Eur. Phys. J. C 74:2746, 2014*

[Lus10] C. Lussenhop*:* Measuring Reflective Properties of PTFE for Applications in Liquid Xenon Detectors. *Report, Columbia University, 2010*

[Mar13] M. Martinez*:* Search for Dark Matter at the LHC. *Journal of Physics 460, 2013*

[Mcc15] E. A. Mccutchan*:* Nuclear Data Sheets 125, 201. *Brookhaven National Laboratory, 2015*

[Mil87] M. Milgrom, J. Bekenstein*:* The modified Newtonian dynamics as an alternative to hidden matter. *IAU Symposium, V. 117, p. 319-330, 1987*

[Mil01] Millipore Corporation*:* PTFE Membrane Filters - For filtering acids, bases, or solvents, as well as gases. *Bedford, MA., 2001*

[MKS06] MKS Instruments*:* Digital Mass Flow Controller Type 1579A and Digital Mass Flow Meter 579A - Instruction Manual. *2006*

[NASA10] NASA*:* http://apod.nasa.gov/apod/ap150410.html *Tony Hallas, 15.04.2010*

[NDC15] Nuclear Data Center*:* http://wwwndc.jaea.go.jp/cgi-bin/nuclinfo2010?37,83 *Japan Atomic Energy Agency, 2011*

[Oli14a] K. A. Olive et al. (Particle Data Group Collaboration)*:* Neutrino mass, mixing, and oscillations. *Chin. Phys. C* **38** *(2014) 090001*

[Oli14b] K. A. Olive et al. (Particle Data Group Collaboration)*:* Axions and other similar particles. *Chin. Phys. C* **38** *(2014) 090001*

[Oli14c] K. A. Olive et al. (Particle Data Group Collaboration)*:* Cosmic Rays. *Chin. Phys. C* **38** *(2014) 090001*

[Oli14d] K. A. Olive et al. (Particle Data Group Collaboration)*:* Leptons. *Chin. Phys. C* **38** *(2014) 090001*

[Ost08] Beatrix Ostrick*:* Eine kondensierte ^{83m}Kr-Kalibrationsquelle für das KATRIN-Experiment. *PHD-thesis, WWU Münster, 2008*

[Pla13] *Planck Collaboration:* Planck 2013 results. I. Overview of products and scientific results.

[Pla12] Guillaume Plante*:* The XENON100 Dark Matter Experiment: Design, Construction, Calibration and 2010 Search Results with Improved Measurement of the Scintillation Response of Liquid Xenon to Low-Energy Nuclear Recoils. *Columbia University, 2012*

[Rea14] J. I. Read*:* The Local Darm Matter Density. *J. Phys. G: Nucl. Part. Phys. 41 063101*

[Ros14] S. Rosendahl et al.*:* A novel ^{83m}Kr tracer method for characterizing xenon gas and cryogenic distillation systems. *JINST 9 P10010, 2014*

[Ros15] S. Rosendahl*:* Gas purification of the XENON dark matter experiment. *PHD-thesis, WWU Münster, 2015*

[Rub70] V. C. Rubin, W.K. Ford*:* Rotation of the Andromeda Nebula from a Spectroscopic Survey of Emission Regions. *Astrophysical Journal, Vol. 159, p.379, 1970*

[Sae01] SAES Pure Gas Inc.*:* PS4-MT50-R, Rare Gas Purifier, Product Manual. *Rev. A, 2012*

[Sch12] S. Schneider*:* Measurement of Kr-83m Doping in Xenon Gas for Calibration and Tracer Applications. *Bachelor thesis, WWU Münster, 2012*

[Sil10] C. Silva et a.*:* Reflectance of polytetrafluoroethylene for xenon scintillation light. *J. Appl. Phys., V. 107, 064902, 2010*

[Sin14] B. Singh, J. Chen*:* Nuclear Data Sheets for A=85. *Nuclear Data Sheets, V. 116, N. 0 p. 1-162, 2014*

[Sol04] V. N. Solovov et al.*:* Measurement of the refractive index and attenuation length of liquid xenon for its scintillation light. *Nucl. Instrum. Meth. Phys. Res. A 516, p.462-474, 2004*

[Swa07] Swagelok*:* Pressure Transducers, Ultrahigh-Purity. *Swagelok Company, 2007*

[Swa08] Swagelok*:* Bellows-Sealed Valves, B Series. *Swagelok Company, 2008*

[Swa13] Swagelok*:* Filters, FW, F, and TF Series. *Swagelok Company, 2013*

[Tig06] HALO+*:* Trace Gas Analyzer, Instruction Manual, M7103 Series. *Rev. G, 2006.*

[Toj06] R. Tojeiro*:* Understanding the Cosmic Microwave Background Temperature Power Spectrum. *2006.*

[Unb87] Heinz Unbehauen*:* Regelungstechnik I. *Wiesbaden, 1987.*

[Ven05] D. Vénos et al.*:* ^{83m}Kr radioactive source based on ^{83}Rb trapped in cation-exchange paper or in zeolite. *Applied Radiation and Isotopes Vol 62, p. 323-237, 2005.*

[Zwi33] Fritz Zwicky*:* Die Rotverschiebung von extragalaktischen Nebeln. *Helvetica Physica Acta Vol. 6, p. 110-127, 1933.*

Danksagung

An dieser Stelle möchte ich meinen ausdrücklichen Dank aussprechen an so viele, die mich im Rahmen dieser Arbeit unterstützt haben.
Allen voran möchte ich Prof. Dr. Christian Weinheimer danken, dafür dass er mir über Jahre hinweg in unterschiedlichen Positionen die Arbeit in seiner Arbeitsgruppe ermöglicht hat und dabei stets prägende Anreize für den Fortschritt der jeweiligen Projekte gegeben hat. Wie man es schafft bei einem 28 h Tag noch die Zeit zu finden mit einem Studenten über alle möglichen Probleme zu reden oder sogar sich über seine Hobbys auszutauschen, werde ich wohl nie verstehen aber weiß jede Minute mehr als zu schätzen. Prof. Dr. Alfons Khoukaz muss ich ebenso danken, für seine die Bereitschaft sich als Korreferent zur Verfügung zu stellen.
Special thanks go to Assist. Prof. Ethan Brown. for letting me work on and grant me the responsibility for a crucial project. Even more I have to thank you for giving me your trust and offering me a position in your group.
Der gesamten Arbeitsgruppe gilt mein Dank für das gute Arbeitsklima und den stets offenen Türen und Ohren. Stephan Rosendahl als Vater unseres Labors muss ich explizit danken. Obwohl während der Zeit dieser Arbeit quasi verabschiedet, standest du doch stets mit guten Tipps zu Verfügung. Auch Christian Huhmann danke ich für die umfangreiche Unterstützung im Labor sowie für die Zeit die er investierte vage Vorstellungen in klare technische Zeichnungen zu verwandeln. Ebenfalls danke ich dem gesamten Team der mechanischen und elektronischen Werkstätte, für die Arbeit Konzepte auf Papier real werden zu lassen.
Der Kaffeerunde alias Fussballdebattierclub alias Physiker 3.0-Sergej danke ich auch für unterhaltsame Gespräche, die stets Farbe in den Büroalltag gebracht haben.
Alex und Michael danke ich speziell für die gemeinsame Zeit in der Arbeitsgruppe genauso für das intensive Korrekturlesen, die durch euch erst Struktur und Qualität erhalten hat. Dank euch gab es beim Arbeiten stets was zu lachen. Und Alex, wenn deine Wingman-Qualitäten nur ansatzweise denen deiner Physiker-Qualitäten entsprechen würden, wer weiß, vielleicht wären wir dann gemeinsam den WIMPs auf die Schliche gekommen.
Vor allen Dingen muss ich mich aber bei meinen Eltern, meiner Schwester und meiner gesamten Familie bedanken. Ob mental oder finanziell habe ich von euch Unterstützung erhalten, die alles andere als selbstverständlich ist. Der Halt, den ihr mir gebt, lässt mich auch in der aussichtslosesten Situation nicht ganz die Nerven verlieren. Ohne euch wäre ich nicht wo und nicht wer ich heute bin.